Title
Experimental Investigations of Partially Premixed Hydrogen Combustion in Gas Turbine Environments

Author
North, Andrew

Publication Date
2013

Peer reviewed|Thesis/dissertation

Experimental Investigations of Partially Premixed Hydrogen Combustion in Gas Turbine Environments

By

Andrew Jon North

A dissertation submitted in partial satisfaction of the

requirements for the degree of

Doctor of Philosophy

in

Applied Science and Technology

in the

Graduate Division

of the

University of California, Berkeley

Committee in charge:

Professor Robert Dibble, Chair

Professor Jyh-Yuan Chen

Professor Michael Frenklach

Fall 2013

Abstract

Experimental Investigations of Partially Premixed

Hydrogen Combustion in Gas Turbine Environments

By

Andrew Jon North

Doctor of Philosophy in Applied Science and Technology

University of California, Berkeley

Professor Robert Dibble, Chair

The carbon dioxide emission prevention advantage of generating power with high hydrogen content fuels using gas turbines motivates an improved understanding of the ignition behavior of hydrogen in premixed and partially premixed environments. Hydrogen rich fueled flame stability is sensitive to operating conditions, including environment pressure, temperature, and jet velocity. Furthermore, when premixed or partially premixed operation is desired for nitric oxide emissions reduction, a diluent, such as nitrogen, is often added in allowing fuel/air mixing prior to combustion. Thus, the concentration of the diluent added is an additional independent variable on which flame stability dependence understanding is needed. The focus of this research is on characterizing the dependence of hydrogen jet flame stability on environment temperature, jet velocity, diluent concentration, and pressure by determining the dependence of the liftoff height of lifted flames on these 4 independent parameters. Nitrogen is used as the diluent due to its availability and effectiveness in promoting liftoff.

Experiments are first conducted at atmospheric pressure in scoping subsequent research where the additional parameter of pressure is added. The stability and liftoff characteristics of a nitrogen diluted hydrogen jet flame at atmospheric pressure in a vitiated co-flow are investigated experimentally and numerically with particular attention focused on regimes where multiple stabilization mechanisms are active. Information gleaned from this research is instrumental for informing modeling approaches in flame transition situations when both autoignition and flame propagation influence combustion characteristics. Stability regime diagrams which outline the conditions under which the flame is attached, lifted, blown-out, and unsteady are experimentally developed and explored. The stability of the flame is investigated with a 1D Reynolds Averaged Navier Stokes parabolic numerical model which shows that under certain conditions, local turbulent flame speeds exceed the local velocity for the production of stable lifted hydrogen

flames. These modeling results suggest that the dominant flame stabilization mechanism is flame propagation, and likely tribrachial flame propagation, consistent with the conclusions of prior studies for jet flames issuing into ambient environments such as the research of Muñiz and Mungal (1997). The lifted regime is further characterized at atmospheric pressure in determining liftoff height dependence on co-flow temperature, jet velocity, and nitrogen dilution. A strong sensitivity of liftoff height to co-flow temperature, jet velocity, and nitrogen dilution is observed. The numerical model results trend well with the experimentally developed stability regime diagrams. Liftoff heights predicted by Kalghatgi's correlation are unable to capture the effects of nitrogen dilution on liftoff height for the heated co-flow cases. A uniquely formulated Damköhler number was therefore developed which acceptably captures the effects of jet velocity, nitrogen dilution and environment temperature on liftoff height. Satisfactory agreement between the correlation results which relies on propagation parameters in its formulation further indicates that stabilization is indeed dominated by propagation.

The unsteady regime is also investigated experimentally at atmospheric pressure. The unsteady regime is characterized by rapid ignition events of an initially unburned jet of fuel, and these events are always followed by subsequent blowout events. The frequency by which these ignition events occur are measured and insights are drawn regarding the impact of nitrogen dilution, jet velocity, and co-flow equivalence ratio on ignition frequency. Nitrogen addition to the fuel increases autoignition delay times which reduces ignition frequency, though it also reduces the speed of flame propagation which increases the frequency of blowoff. Consequently, when the level of nitrogen dilution added to the fuel is moderate, increases in dilution increase ignition frequency, and when high levels of nitrogen are added, further increases reduce ignition frequency because each ignition event is preceded by a blowoff event. Jet velocity increases lead to broader ranges of nitrogen dilution where unsteady behavior is observed. Finally, increases in co-flow equivalence ratio result in unsteady behavior for greater levels of nitrogen dilution

Experiments are also conducted at elevated pressure with co-flow temperature, jet velocity, and nitrogen dilution still parameterized. Strong sensitivity of liftoff height on co-flow temperature and pressure is observed both when jet velocity and jet Reynolds number are held constant as pressure is varied. With confinement, which is required in achieving elevated pressure, liftoff height sensitivity on jet velocity is diminished. The Damköhler number is again utilized in assessing its utility in incorporating the pressure effect, and satisfactory correlation results are demonstrated. Elevated pressure results and atmospheric pressure results (without confinement) indicate that the Damköhler number can be used in scoping experimental lifted flame research at elevated pressures and temperatures and in informing numerical modeling approaches for research as well as in industry.

To my wonderful mother and father, whose strength and support guided me every step of the way.

Table of Contents

Table of Figures

Acknowledgements

This publication has been produced with support from the BIGCCS Centre, performed under the Norwegian research program Centres for Energy Efficient Research. The authors acknowledge the following partners for their contributions: Aker Solutions, ConocoPhilips Skandinavia AS, Det Norske Veritas AS, Gassco AS, Hydro Aluminium AS, Shell Technology AS, Statkraft Development AS, StatoilHydro Petroleum AS, TOTAL E&P Norge AS, and the Research Council of Norway (178004/I30 and 176059/I30).

1. Introduction

i. *Motivation*

Carbon Capture and Sequestration (CCS) provides a means of generating power from fossil fuels without emitting Carbon Dioxide (CO_2) into the atmosphere. When the power is generated in gas turbine combustion systems, the CO_2 can be removed from the exhaust (post-combustion CCS), or prior to combustion of the fuel (pre-combustion CCS), in addition to other means. In pre-combustion CCS, the original fuel can be natural gas (reformed) or coal (gasified and reformed) which is converted to a synthetic fuel mixture containing mainly hydrogen (H_2) and carbon monoxide (CO) [1]. This process is outlined at a high level in Figure 1. The converted fuel yields H_2 as the primary product, while the CO is reacted with water forming more H_2 and CO_2. The CO_2 can be separated and sequestered, completing the CCS value chain, and the H_2 can then be used as fuel for large-scale, clean, efficient power generation. In comparison with the natural gas widely utilized in current state-of-the-art gas turbines, H_2 is characterized by a much greater energy density by mass. Additionally, the significantly reduced autoignition delay times of preheated H_2 mixtures, wide flammability limits, and high flame speeds, imply that current gas turbine combustors are not optimized for H_2 operation. In other words, the knowledge base which led to the state of the art in gas turbine combustors is restricted to a single fuel (natural gas) which is not an applicable knowledge base for applications where H_2 is used instead. Of the many challenges in developing lean premixed, partially premixed, and non-premixed H_2-fired gas turbines [2], one of the most serious fundamental issues is the stabilization of lifted H_2 jet flames. Lifted flames are a key research tool for developing knowledge which is critical for optimizing stationary gas turbine combustors fueled with H_2. Additional data sets characterizing lifted H_2 jet flames in gas turbine environments are beneficial for numerical model development and in developing an improved understanding of the factors that influence partially premixed flame ignition and stability. The liftoff height (L) for lifted flames is a readily measurable quantity which serves as a challenging benchmarking parameter for numerical models.

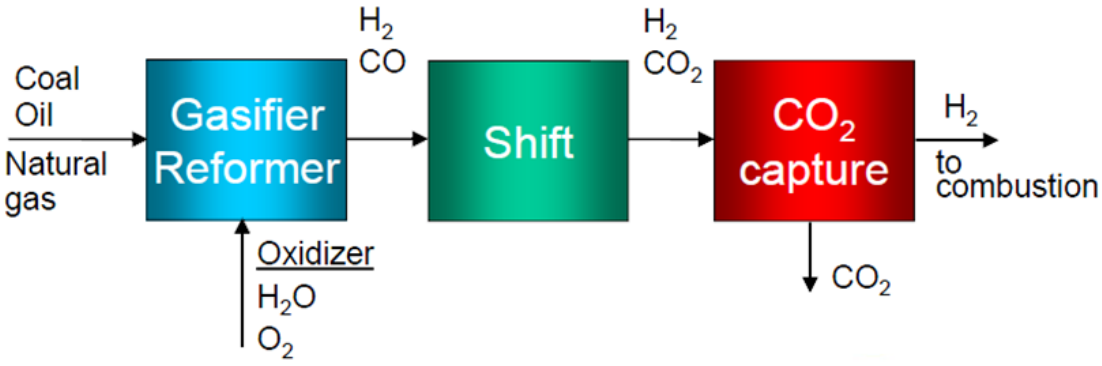

Figure 1: Drawing illustrating conceptually the process of converting fossil fuels to hydrogen.

While virtually all pollution is eliminated when H_2 is used as a fuel, Nitric Oxide (NOx) can still be an issue. For this reason, H_2 should be premixed before combustion in order to meet NOx emissions standards. A nonpremixed flame is localized where stoichiometric conditions exist, where the maximum temperature exists. NOx production rates are maximized as a result. By

premixing the fuel with the air, the maximum flame temperature is significantly reduced, reducing rates of NOx production. Oxygen concentration also impacts NOx production rates, though this effect is not as influential as temperature. These points are illustrated pictorially in Figure 2.

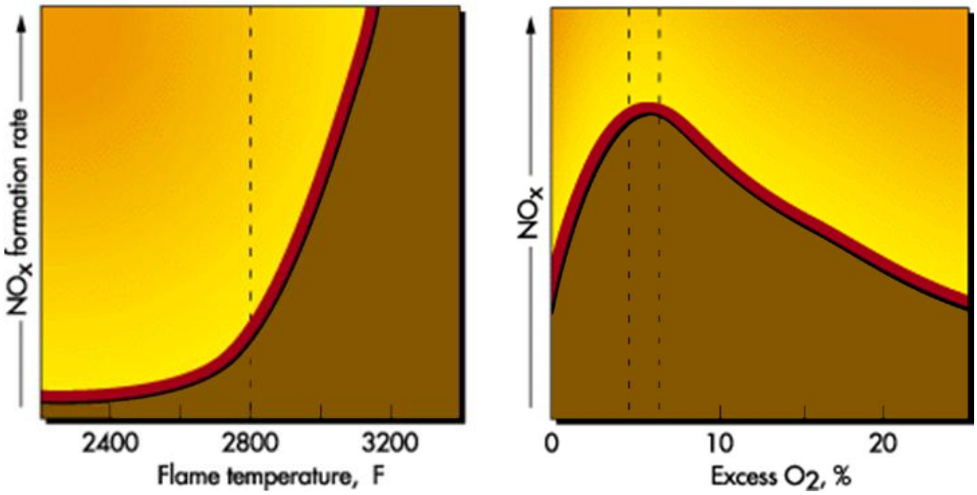

Figure 2: NOx formation rate dependence on flame temperature and oxygen concentration.

In achieving premixed operation, a mixing section is typically employed where the air and the fuel are mixed. The mixing section is designed such that the propensity for a flame igniting or propagating into the mixing section, which is called flashback. Flashback is avoided at all costs, because flashback in the mixing section necessitates shutting down the turbine causing significant loss of revenue and/or damage to the turbine.

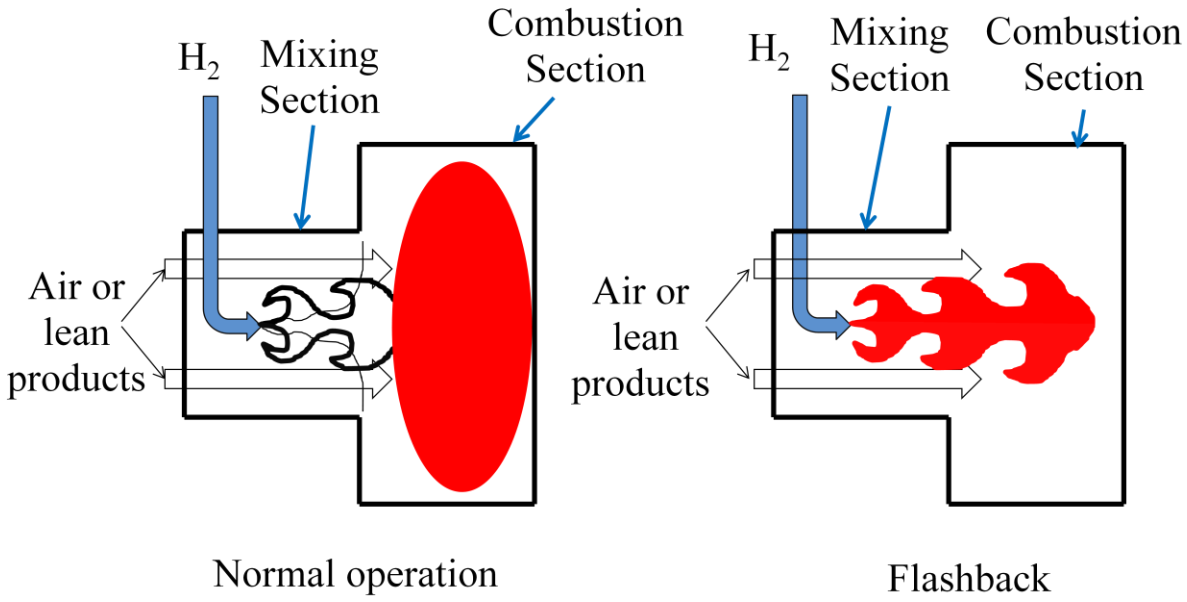

Figure 3: Illustration showing the nature of flashback.

This research is therefore primarily motivated in gaining the knowledge and tools necessary for informing gas turbine power plant developers on how to design and operate H_2 fueled gas turbine combustors for flashback avoidance.

ii. *Background*

Several theories exist which propose explanations of the mechanism responsible for stabilizing turbulent lifted jet flames [3] [4], including premixed flame propagation [5], the extinction of diffusional flamelets [6] [7], large scale structures [8], tribrachial flame behavior [9] [10], and autoignition [11] [12] [13] [14] when a heated co-flowing oxidizer is included. Markides et al (2005) [15] also experimentally investigated the effects of turbulence interactions between the jet and surroundings on liftoff for autoignition dominated flames and concluded that these processes are coupled and that turbulent mixing between the jet and co-flow delays autoignition.

Despite the myriad of flame stabilization theories in existence, a simple correlation proposed by Kalghatgi [16] which relies solely on the premixed flame propagation theory as the flame stabilization mechanism, is capable of reproducing virtually all turbulent lifted jet flame data including those with Nitrogen (N_2) dilution, yet importantly, excluding cases where a vitiated co-flow has been applied. Peters (2000) [17] explains that for the "conventional" lifted turbulent jet flames the Damköhler number is small enough for premixed flame propagation terms to dominate over terms related to the extinction of laminar diffusional flamelets. Peters further argues that the flame structure observed with these flames (without heated co-flows) is commonly tribrachial, though the liftoff height (L) is often governed by multiple stabilization mechanisms while consistently enhanced by tribrachial flame geometry [17]. It should also be noted that while laminar diffusion quenching events do not determine the liftoff height, there is little doubt that diffusion flame quenching is responsible for the liftoff of an initially attached flame [17]. When local fluctuating strain rates near the nozzle exceed a threshold value, the flame is forced downstream where scalar dissipation rates are relaxed and mixing lengths are increased. The influence of scalar dissipation on flame stabilization is further explained by Peters [7]. The stabilization region, however, is on average downstream of the region where local scalar dissipation rates descend below the threshold quenching value because of insufficient tribrachial flame speeds. Instead, the flame stabilizes at a radius and axial location where the speed of an ensemble of tribrachial flamelets balances the local flow velocity. Kalghatgi's correlation is capable of accounting for tribrachial flame speed enhancement through calibration of the constant of proportionality, which is also fuel dependent.

Predicting the liftoff height of lifted turbulent jet flames is arguably the most severe model validation test [17], hence liftoff height characterization data have been used in the development and validation of many sophisticated models. Some example models include application to turbulent lifted H_2-in-N_2 jet flames in vitiated co-flows and in describing the flame stabilization mechanism at work. Cao et. al. (2005) [18] used the joint velocity-turbulence frequency-composition PDF method and captured the strong sensitivity of liftoff height to co-flow temperature which is observed in experimental results. They also found that model results suggest that flame stabilization is primarily controlled by chemical kinetics for the flames studied. Additionally, Kumar et. al. (2007) [19] used a flame extinction model based on the k-ε turbulence time scale concept for the prediction of liftoff heights for a wide variety of conditions

and fuels including cases with hot co-flows. Kumar et. al. observed that the flame stabilizes where the local flame propagation speed equals the local fluid velocity. The same method was also used to predict combustion dynamics for mild combustion burners [19].

Since experimental data sets of turbulent lifted jet flames are critical for numerical model development and validation, extensive work is being conducted to broaden these data sets. Gordon et. al. [20] [21] [22] [23] recently made significant experimental contributions involving turbulent H_2-in-N_2 jet flames in a vitiated co-flow. A primary motivation for their work was the determination of a means of differentiating between regimes dominated by partially premixed flame propagation from those dominated by autoignition. Co-flow temperatures between 1000 K and 1475 K were considered, and the dependence of liftoff height on co-flow temperature ($T_{co\text{-}flow}$), co-flow velocity, and jet velocity (V_{jet}) was characterized. They concluded that the liftoff height for hydrogen jet flames is more sensitive to co-flow temperature than that of methane lifted jet flames owing to the aforementioned greater H_2 autoignition sensitivity versus that of methane.

iii. *Vitiated Co-flow Burner Introduction*

The present work is similar to the work by Gordon et. al. [20] [21] [22] [23], though the motivations are distinct and the approach here is unique and beneficial. The nature of flame stabilization is investigated experimentally using an upgraded Berkeley Vitiated Co-flow Burner (VCB) [24] as sketched in Figure 4. The reason for choosing Berkeley's VCB configuration is twofold. Firstly, the VCB represents a convenient setup for a parallel experimental and numerical investigation. Secondly, the VCB allows relatively simple and well defined specifications of the boundary conditions together with straightforward measurements of the main parameter (L). Thirdly, the VCB presents an opportunity for investigating the chemical kinetic complications inherent when recirculation is involved as well as the complications involved with high Reynolds number turbulence. Recirculation occurs with the VCB as a result of the high shear forces between the jet reactants and the co-flow products. Finally, the VCB configuration is also relevant to applications; it in fact represents a compact and geometrically simplified version of the Alstom GT24/26 second stage burner (Sequential EV), which is shown in Figure 5.

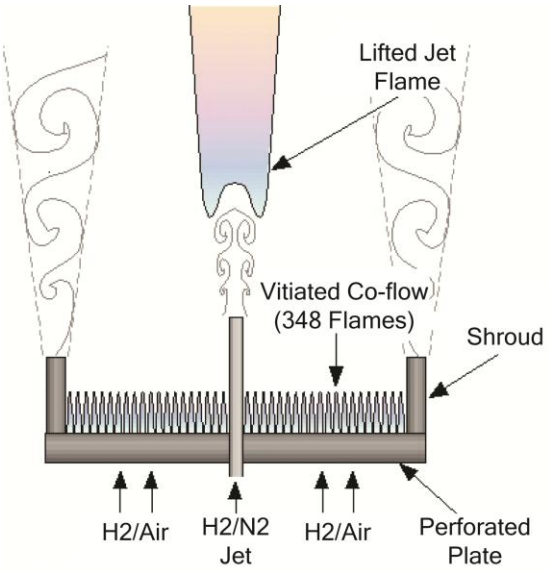

Figure 4**:** Berkeley's VCB used in developing experimental data.

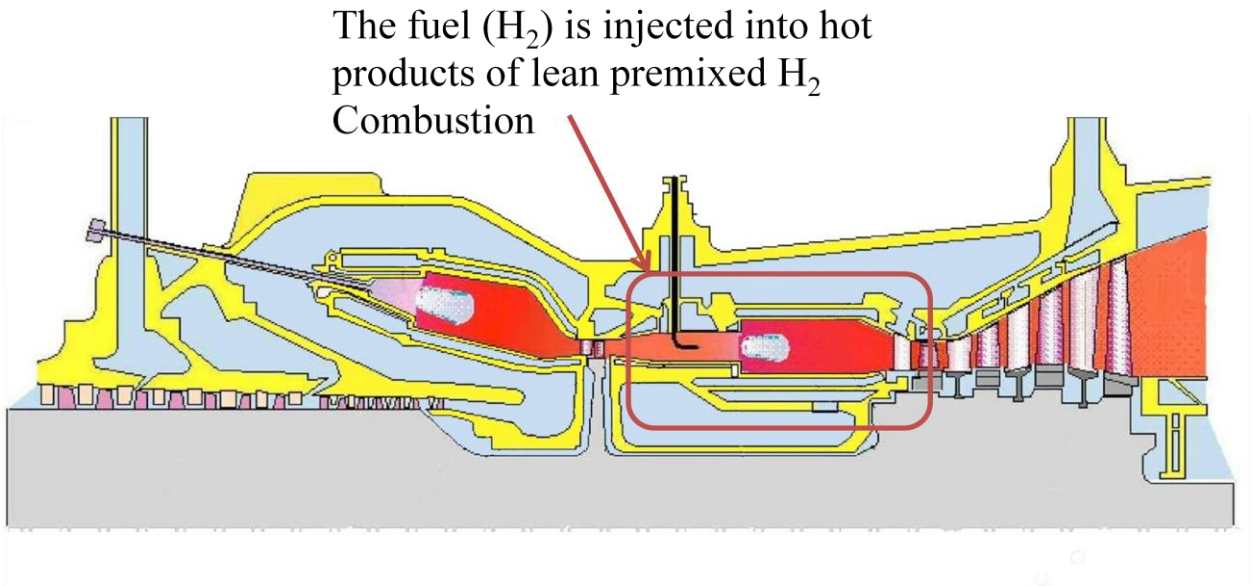

Figure 5: Conceptual drawing of the Alstom GT 24/26 Gas Turbine.

The VCB consists of an ambient temperature high velocity fuel jet issuing into a co-flowing stream containing nearly adiabatic products of lean premixed H_2-air combustion. The geometry of the upgraded VCB (in comparison to the original design by Ricardo Cabra [11]) is designed to increase the operational flexibility of the burner allowing investigations of broader V_{jet} and nitrogen dilution mole fractions (y_{N2}) ranges, and for better co-flow fluidic control without prohibitively complicated flow control techniques. The jet inner diameter has been scaled down by a ratio close to the co-flow dimension downscaling factor in preserving the 'potential core' height [25], which is the height at which outside air entrainment begins. Cabra et al [25] measured the potential core height on the original burner reporting z/d = 42, which is greater than the liftoff heights encountered with the current burner. Similarity is invoked with the upgraded burner in making use of the potential core height measurements performed by Cabra et

al. Additionally, the reduced co-flow temperatures investigated in the present research increases the potential core height [25]. The temperature of the co-flow stream is controlled by varying the co-flow stoichiometry ($\varphi_{co\text{-}flow}$). N_2 is added to the fuel jet which encourages the flame to lift from the nozzle by increasing scalar dissipation rates near the nozzle which quenches the combustion reaction locally [7]. Chemical kinetic effects also likely play an important role on the effect of N_2 dilution on flame detachment, though research by Karbassi et. al. [26] shows that the molecular mass of the diluent added to the fuel plays a most critical role on attached flame stability. Hence, the impact of N_2 addition is likely dominated by the effect of momentum effects independent of V_{jet} adjustments.

iv. *Elevated Pressure Vitiated Co-flow Burner Introduction*

Once the atmospheric pressure scoping work was completed, the VCB was redesigned and built in the interior of a pressure chamber in adding functionality for investigating the pressure effect on lifted N_2-in-H_2 flames. As with the atmospheric pressure experiments, premixed H_2 and N_2 issue through a circular nozzle without taper and an inner diameter of d_{jet} = 2.4 mm. The nozzle is again placed around a co-flow composed of combustion products of premixed H_2 and air. The premixed H_2 and air flames are stabilized on a perforated plate with 348 1.6 mm diameter perforations arranged hexagonally with 4.8 mm separation between perforations. The total blockage ratio of the co-flow remains 0.89.

The redesigned burner includes minor modifications in the design of the co-flow which are necessary for interfacing the hardware with a pressure chamber. Additionally, a spark-plug igniter is added to the co-flow as well as an additional igniter downstream for ignition of the jet reactants. The pressurized VCB is shown in Figure 6.

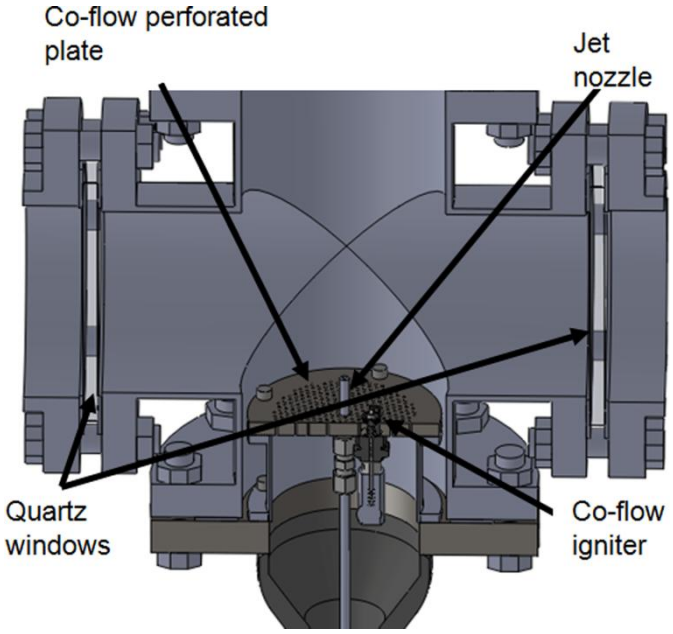

Figure 6: Pressurized VCB showing the igniter and windows for viewing access.

The jet nozzle height above the co-flow plate is adjustable between 0 cm and 4 cm. 15 cm diameter windows allow viewing access used for schlieren imaging and direct imaging.

v. *Steady State Elevated Pressure Vitiated Co-flow Burner Introduction*

An elevated pressure vitiated co-flow burner capable of operating at steady state was also designed for experimental investigations desired over a longer time span where more sophisticated diagnostics may be employed. This apparatus was never constructed, though its design is introduced nonetheless for completeness. The concept is functionally equivalent to the transient design, though cooling systems needed to be incorporated to allow steady state operation. The redesign effort involved resizing the burner to fit within the a pressure vessel which had already been constructed, and the incorporation of a heat shield with adequate cooling to maintain the pressure vessel walls at or below the maximum temperature of 200^{o} C. The heat shield incorporates a double walled cooling scheme, with carbon dioxide flowing between the heat shield windows. The rest of the heat shield is water cooled, with a copper cooling jacket that spirals around the outside perimeter of the heat shield. The final design is shown in Figure 7 and Figure 8:

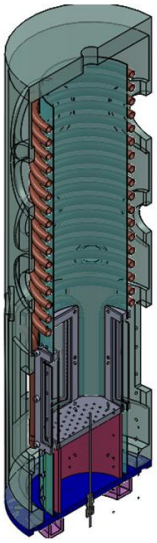

Figure 7: Section view of the steady state elevated pressure version of the Vitiated Co-flow Burner (VCB).

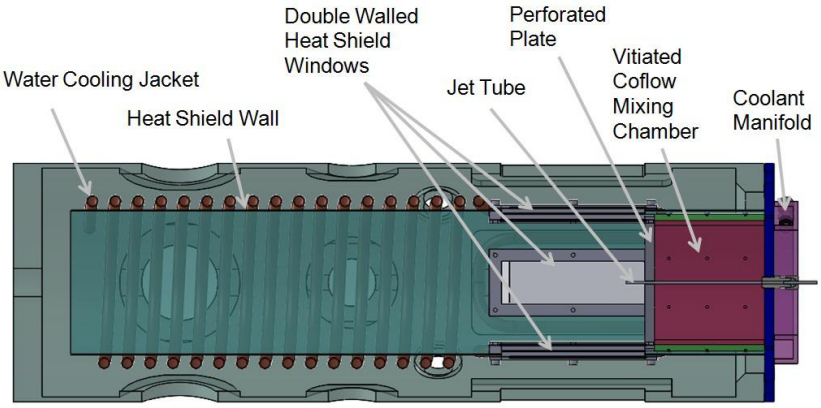

Figure 8: Side view of the steady state elevated pressure VCB.

The water cooling jacket maintains the heat shield below the temperature where radiation from the heat shield would heat the pressure vessel walls beyond their temperature threshold. The double walled windows ensure that the pressure vessel windows do not receive excessive radiation from the heat shield windows. The perforated plate creates the co-flow around the jet, while minimizing the chances for flashback. The diameter of the co-flow is 150 mm and is perforated with a blockage ratio of 0.89 as before.

2. Methods

i. *Experimental Methods*

a) Atmospheric Pressure Research

Stability Regimes Development Methodology

For the research conducted at atmospheric pressure, flame stability is characterized experimentally by first creating stability regime diagrams which outline the conditions under which the flame is attached, lifted, blown-out or unsteady. Stability regime diagrams are created for V_{jet} = 300, 400, and 500 m/s. $\varphi_{co\text{-}flow}$ is held constant for a given experiment, and y_{N2} is slowly increased until the flame lifts or becomes unsteady, which allows the point of transition (from attached to lifted and lifted to blown-out) to be recorded. The unsteady regime, in the context of this research, is characterized by repeated transitions from an attached condition to a lifted condition where the liftoff height rapidly increases until blowout, and subsequent rapid ignition of the jet reactants. When re-ignition occurs, an attached flame is again formed and the cycle is repeated. It is important to note that hysteresis effects in influencing the transition to the lifted condition are well known and documented [3], and the boundary between the attached flame and a lifted flame is different when y_{N2} is ramped down instead of ramped up. (e.g., when a flame is already lifted, reducing y_{N2} yields a lifted flame for values of y_{N2} where an attached flame is present if starting from an attached flame and increasing y_{N2}). Nonetheless, a single stability regime diagram for each case is desired for bounding the liftoff height characterization portion for the current research so each experiment starts from an attached flame and y_{N2} is increased until the flame lifts in simplifying the liftoff height characterization which follows. The nitrogen ramping scheme, however, does not affect jet flame stability characteristics in the unsteady regime for the current burner geometry. A sweep of $\varphi_{co\text{-}flow}$ values of interest is investigated and the data forms the stability regime diagrams which summarize the conditions under which the flame is attached, lifted, blown-out and unsteady when y_{N2} dilution is ramped up.

Liftoff Height Characterization Methodology

The lifted regime is further experimentally investigated, and the dependence of L on V_{jet}, y_{N2}, and $\varphi_{co\text{-}flow}$ is characterized. As explained in the previous section, N_2 dilution is required because the broad flammability limits and high diffusivity of H_2 makes lifted H_2 flame generation difficult. For example, at atmospheric conditions and with a jet nozzle diameter of d_{jet} = 2.4 mm, the flame remains attached even at the sonic velocity of H_2 (1300 m/s). Liftoff height L is determined by measuring a time averaged ensemble of schlieren images with a shutter time of 156 μs. The

liftoff height definition is relatively unambiguous at this frame rate and is defined as the location where the schlieren image depicts a noticeable density gradient in the jet stream. The schlieren imaging approach is advantageous over direct imaging as prior research where direct imaging was employed and uncertainty values were computed demonstrated that the magnitude of uncertainty resulting from the long frame rates required with direct imaging are often the same order of magnitude as the liftoff height measurements themselves [28]. In the current research, 50 frames equally spaced apart in a period of 10 seconds were analyzed by hand in determining the mean liftoff height.

The range of operating conditions investigated is broader than prior experimental investigations, allowing an improved understanding of how the stability mechanisms change as functions of operating conditions. The jet diameter (2.4 mm) is smaller than many prior studies. A small diameter jet affects the range over which stable lifted flames exist, while allowing a broad range of jet velocities to be studied with practical flow control mechanisms. Contrary to studies of conventional jet flames (e.g., those with no co-flow), the heated co-flow employed in the current research (along with other aforementioned studies) allows for the possibility of a different flame stabilization mechanism due to increased Damköhler numbers.

The increased Damköhler number promotes terms other than those dominated by flame propagation; terms which were not included by Peters [17] in analyzing flames at atmospheric pressures. Instead, it is possible for autoignition to play a more dominant role than flame propagation at higher temperatures ($T_{co\text{-}flow} > 800$ K) [15] yet the exact nature of flame stability at intermediate temperatures (600 K – 800 K) is not as well characterized. Generally speaking, a combination of (tribrachial) flame propagation and autoignition processes could be influential over the range considered. Numerical simulations are used in improving the understanding of the stability mechanisms which determine the flame regime under selected conditions.

While the effect of this broad range of independent parameters on liftoff height is presented, results are shown with y_{N2} on x-axes instead of $\varphi_{co-flow}$ or V_{jet} because the dependence of L on y_{N2} appears linear, which is not always the case with $\varphi_{co-flow}$ and V_{jet}. Liftoff height measurement results at atmospheric pressure demonstrate that when 3 independent parameters are made variable, significant scatter in liftoff heights result which is a significant modeling challenge. Development of a robust correlation which describes the liftoff height dependence on y_{N2}, V_{jet} and $\varphi_{co-flow}$ is also challenging. RMS values, minimum and maximum values, and a PDF of the liftoff heights, while extremely useful, are not included in the present research because the manual nature by which of liftoff heights are measured made these additional statistical determinations prohibitively time intensive.

Since several stability mechanisms are likely influential when the entirety of the independent parameter space in the current research is considered, no attempt is made here to improve the theoretical understanding of the individual flame stabilization theories nor is any attempt made to propose a new theory. Instead, attempts are made at identifying the conditions under which existing theories apply in various regions of the stability regimes diagrams. Moreover, the current research is intended to provide a broad experimental data set for numerical model benchmarking. The numerical models can subsequently be used for applications where many flame stabilization mechanisms are influential and in assisting the modeling community in

determining the conditions under which particular numerical methods are applicable and when they are not.

The operational conditions investigated include co-flow equivalence ratios of $0.00 \leq \varphi_{co-flow} \leq 0.35$ (corresponding to co-flow temperatures of $293\ K \leq T_{co-flow} \leq 1200\ K$) and jet N_2 mole fractions of $0.0 \leq y_{N2} \leq 0.55$. For all experiments, the jet fuel temperature is approximately $T_{jet} \approx 293$ K and the co-flow bulk velocity before combustion is held constant at $u_{co-flow} = 0.67$ m/s (7.3 m/s in the holes in the plate). The co-flow velocity of the combusted products of the lean premixed flame ranges from roughly 0.67 m/s (for co-flowing air) to roughly 3.2 m/s (for $T_{co-flow} = 1200$ K). Co-flow temperatures are estimated using an experimentally developed correlation [25] of the form:

$$T_{co\text{-}flow}\ (K) = 2462(\varphi_{co\text{-}flow})^{0.69} \qquad (1)$$

Equation 1 was developed for $0.15 \leq \varphi_{co\text{-}flow} \leq 0.5$ and accounts for non-adiabatic conditions. The correlation was based on Raman-Rayleigh thermometry measurements with a reported uncertainty of 3% versus the uncertainty correlated with thermocouple measurements of 5%. Thermocouple measurements performed with the upgraded apparatus also fall within the 5% uncertainty value. The co-flow blowoff limit with the upgraded burner is in agreement with the co-flow blowoff limit observed here, and the burner design is scale similar with Cabra's original design. Thus, there exists greater confidence in the accuracy of the correlation developed by Cabra et al over thermocouple measurements and this correlation is consequently opted for co-flow temperature characterization in lieu of thermocouple measurements.

Since the speed of sound in pure H_2 is ~1300 m/s, much higher jet velocities than the speed of sound in air are achievable with this fuel. As N_2 dilution is increased, however, the speed of sound in the jet fluid decreases. For example, for the case with the maximum amount of N_2 dilution investigated in the current work ($y_{N2} = 0.55$), the speed of sound in the jet fluid is ~500 m/s. Consequently, it is not possible to achieve N_2 dilution values greater than 0.55 with the jet nozzle used. Additionally, compressibility effects are critical for high y_{N2} values and should be included when modeling flames with high y_{N2} values.

Unsteady Regime Characterization Methodology

The frequency of ignition in the unsteady regime was also characterized. As with the liftoff height determination experiments, the jet velocity was kept constant at $V_{jet} = 300$, 400 and 500 m/s. The co-flow temperature was adjusted by adjusting the co-flow equivalence ratio as the temperature increases with increasing equivalence ratio. The co-flow equivalence ratio varied between 0.20 and 0.27. For every co-flow equivalence ratio used, the nitrogen dilution mole fraction was adjusted from the point where the flame is first unsteady until the point where the flame is completely blown out. This way a large part of the unsteady portion of the stability regime diagram is investigated. The case with a jet velocity of 400 m/s was investigated in most detail spanning the entire range of co-flow equivalence ratios between 0.2 and 0.27 with hundredths intervals. The cases with jet velocities of 300 m/s and 500 m/s were investigated with co-flow equivalence ratios of 0.20, 0.22, 0.24, 0.25 and 0.27. The average frequency of ignition was found for varying nitrogen dilution mole fractions for each of the cases. The exit

temperature of the jet was approximately $T_{jet} \approx 298$ K. The flow rate of the co-flow was held constant at 300 lpm which corresponds to a velocity of 0.65 m/s before combustion.

Ignition frequency is measured with a microphone. A representative raw unfiltered sound file of an unsteady flame is shown in Figure 9:

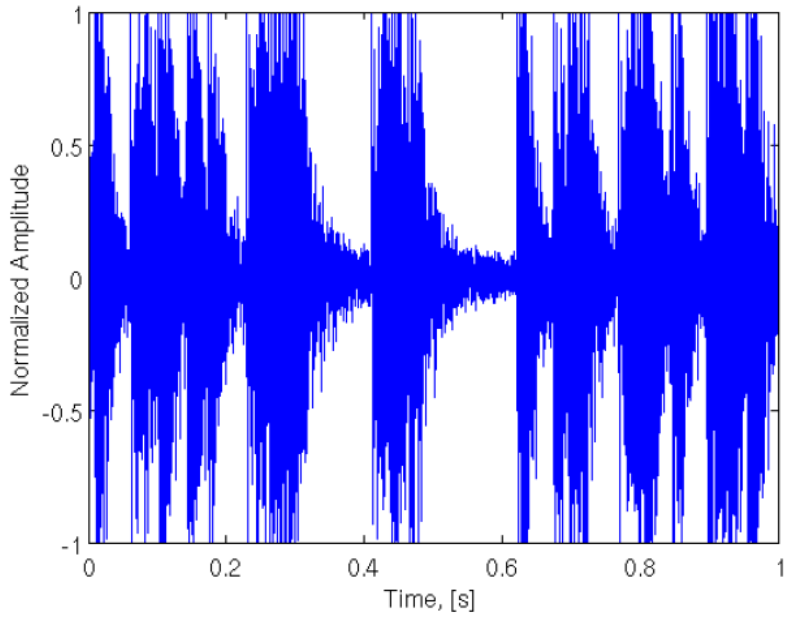

Figure 9: Representative time-amplitude curve of the noise emitted from an unsteady flame.

In this case, it is a simple matter to manually count the peaks and divide by time to determine the frequency of ignition and extinction. In some cases, however, the frequency is much higher and it is more difficult to discern between peaks that are very close to one another. For this reason, alternative methods of automatically determining the ignition frequency were developed. One of the most promising methods of automating the ignition frequency measurements was to filter the time-amplitude signal and apply a Fast Fourier Transform (FFT) to the result. Several filter options were investigated, but ultimately, the result was not repeatable and did not generally agree to the results obtained by counting the peaks manually.

Another method investigated has been given the name the integral method. The idea was to determine the most common frequency by taking into account information from all low frequency components of the FFT through integration. The integral of the FFT from zero Hz to a predetermined maximum relevant frequency is first computed. Then, the frequency which splits this area in half is found. This frequency is theoretically the average frequency. Unfortunately this method also did not repeatedly give the correct frequency. One of the problems with this method was that it gives a different frequency for different frequency ranges chosen to integrate over. Another problem with the method was the low frequency background noise which weighted the output towards the low frequency side. A background correction was therefore performed on the signal where the background noise was subtracted from the original sound file. This method still did not produce results consistent with the counting method, possibly because of the background noise. Consequently, the method of manually counting acoustic amplitude

peaks on the measured time-amplitude response curves was ultimately opted as the primary method of determining frequency ignition for the unsteady regime analyses.

b) Transient Elevated Pressure Research

With the elevated pressure apparatus, heat loads to the walls of the combustion chamber exceed levels at which reasonable methods for achieving steady state conditions via traditional wall cooling techniques could be employed. Instead, the burner is designed for operation in a quasi-transient mode, where the walls do not reach steady state conditions, while liftoff characteristics remain steady over the time span during which data is gathered. The co-flow burns for 6.5 seconds before jet reactant flow begins. The jet flows for 2 seconds and data is gathered for the last 500 ms of this time period. The timing sequence was determined through an iterative process achieving a workable balance between obtaining 1) manageable combustor wall heating per experiment, 2) eliminating flow transients at startup, and 3) capturing a statistically significant mean value for L. The adequacy of the time span over which the mean liftoff height is determined is assessed by ensuring that a minimum number of repeating turbulence events occurs within the measurement span and that the pressure and flow rate variation over the selected time span is acceptably low. The minimum number of repeating turbulence events is estimated by counting the number of times L oscillates during the chosen time span. Typical oscillation counts vary between 10 and 20 occurrences over the chosen time span.

The independent variables explored in the elevated pressure research include environment temperature, y_{N2}, and V_{jet} as before as well as the added independent parameter of environment pressure (P_{chamb}). The effects of varying each of these independent parameters on L are investigated in detail. Remapping of the stability regimes diagrams is attempted with the elevated pressure VCB with limited success due to issues resulting from confinement. As with the atmospheric pressure VCB, the environment temperature is dependent on the equivalence ratio of the co-flow ($\varphi_{co\text{-}flow}$ determines $T_{co\text{-}flow}$). The impact of environment temperature is assessed in a sensitivity analysis of L to $\varphi_{co\text{-}flow}$, while the effect of pressure is investigated more heavily. For the pressure investigations, $\varphi_{co\text{-}flow}$ is held constant at $\varphi_{co\text{-}flow} = 0.15$ in keeping the data set size manageable, which corresponds to a co-flow temperature of ~664 K.

All reactant flow rates are controlled via sonic flow control orifices. H_2 and N_2 timing control is accomplished with solenoid valves. The ignition system timing and valve actuation is controlled via LABVIEW. A high speed camera is triggered by illuminating a light emitting diode in the field of view and the camera's control software is set to begin capturing video data when the light is illuminated with LABVIEW.

Pressure Control

Extensive work was performed on optimizing the means by which the pressure of the chamber is controlled in the vessel. A primary challenge encountered is associated with the fact that the position of the exhaust valves must remain constant during each experiment. This limitation is complicated by the large pressure spike that occurred in early experiments when the co-flow and jet ignited (caused by a sudden expansion of a large volume of combusted gases). It was found

that taking liftoff height data at the end of an experiment minimizes pressure transients, as well as other transients during the time span over which data is gathered.

Figure 10 shows the resulting pressure trace for a representative experiment where data has been taken. Pressure variability in the final 500 ms of the test is acceptably low. Concurrently, Figure 11 demonstrates acceptably low variability in N_2 and H_2 flow rates during the time period of data gathering.

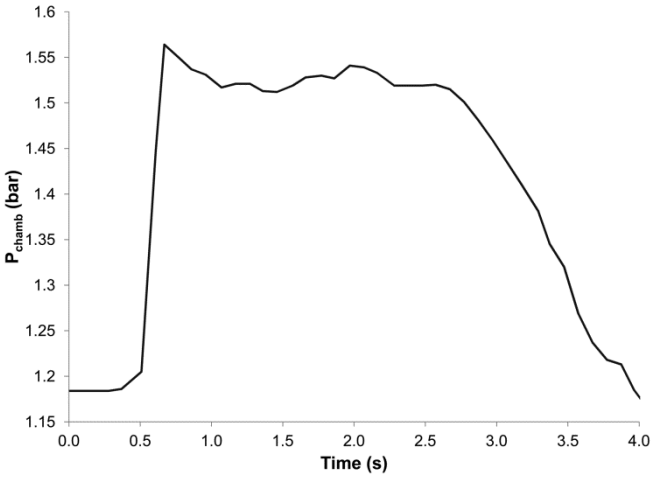

Figure 10: Pressure trace for a representative experiment with a quasi steady-state pressure of ~1.5 bar.

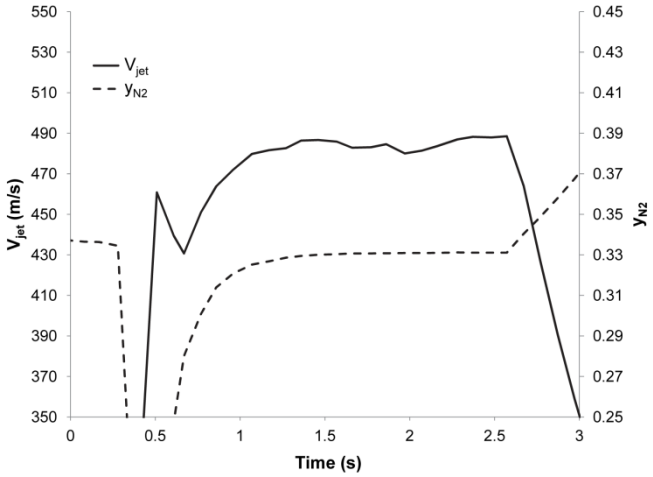

Figure 11: y_{N2} and V_{jet} traces corresponding to the pressure trace given in Figure 10. The quasi steady-state y_{N2} value is 0.33 and the quasi steady-state V_{jet} target is ~500 m/s for this example case.

Co-flow Ignition

Initially, several problems were encountered when attempting to ignite the co-flow. A standard spark plug was investigated initially, but did not extend far enough into the co-flow to achieve reliable ignition. The igniter used instead is designed for steam boilers. Even with this igniter, however, the co-flow would not ignite for equivalence ratios below 0.20. To solve this problem, it was decided to simply increase the equivalence ratio of the co-flow during ignition, and reduce it again before the test. A simple way of achieving this functionality was to install a 1 L tank

between the co-flow hydrogen bottle and the solenoid valve that controls the flow of the hydrogen. The hydrogen tank regulator then sets the pressure of this tank such that the resulting equivalence ratio of the co-flow for this pressure flowing through the sonic flow control orifice will be ignitable. Before the test, however, the regulator is reset to deliver the pressure that will result in the equivalence ratio target. In this way, the tank expels its elevated pressure hydrogen during ignition, but once the tank has emptied, the hydrogen regulator delivers the correct pressure for the test. This scheme fixed all the ignition problems.

Overall Burner Control

The burner operation is controlled by a combination of LABVIEW, manual needle valves on the exhaust, and manual pressure regulators connected to the gas bottles. The sequence of events that occurs for each test is as follows:

1. Set the position of the exhaust valves based on the last test run to achieve the approximate pressure of interest
2. Set the position of the jet hydrogen bottle, jet nitrogen bottle, and co-flow hydrogen bottle regulators based on a previous test to achieve the desired co-flow equivalence ratio, jet velocity, and nitrogen dilution percentage
3. Open the co-flow air valve (air should always be running, even between tests to help cool the apparatus)
4. Start the LABVIEW program
5. Ensure that 450 lpm of air is flowing and that the chamber pressure is below 1.1 bar
6. Press the fire button in Labview. Labview executes the following commands:
    a. Check to make sure that the chamber temperature is less than 40 C, otherwise exit the program
    b. Open the co-flow hydrogen valve and begin sparking (both co-flow spark igniter and jet spark igniter). Sparking occurs for the entire test to ensure that unburned hydrogen does not build up in the vessel
    c. Allow the co-flow to establish for 6.5 seconds to achieve a uniform temperature within the vessel
    d. Check to make sure that the temperature of the chamber is at least 40 C, otherwise exit the program. This ensures that the co-flow has actually lit. If the co-flow has not lit, initiation of the jet can initiate a bulk lighting event of the co-flow which can result in large pressure spikes
    e. Start the jet and let the jet run for 2 seconds
7. The co-flow equivalence ratio, jet velocity, nitrogen dilution percentage, and chamber pressure are plotted continuously in Labview. The program is paused after the firing sequence when the values corresponding to a quasi steady state condition reach the y-axis so that these values can be recorded.
8. Iterate the position of the exhaust valve, jet hydrogen regulator pressure, co-flow hydrogen regulator pressure, or nitrogen regulator pressure according to the next test that needs to be performed.

Addition burner control improvements were also incorporated in increasing the safety features of the system. These changes were made in LABVIEW, and are detailed below.

1. Safety checks were added which ensure that both the co-flow and the jet ignite on time, otherwise the program shuts down and enters a safe state. This improvement prevents the reactor from building up combustible gases and over pressurizing.
2. The jet duration was reduced to 2 seconds (from the original setting of 3.5 seconds), reducing the amount of time that hot water vapor has to accumulate in the dead space, which caused erratic behavior. The reduction in jet duration was made possible because of the ignition system improvements.
3. The control system code was made more robust by simplifying the communication between "while" loops, eliminating outdated structures, and re-coding control language that was originally coded in a less robust manner.
4. The amount of post processing needed to analyze the data was reduced by adding automatic routines in the code.

This method of controlling the burner proved satisfactory from both performance and safety standpoints.

Functionality Testing

With the burner control strategy established, the capabilities of the apparatus were then tested. This process was iterative, so that in the event of a failure the failure would be as low risk as possible. First, the exhaust valves were fully closed and the vessel was slowly pressurized to 2 bar in ensuring that the vessel could hold this pressure under cold conditions. Next, the exhaust valves were fully opened and the co-flow was ignited for an equivalence ratio of 0.15. The pressure remained at 1 bar for this entire test. Next, the hydrogen jet was turned on with a supply pressure of 0.1 bar and the jet lit without issues. Additional tests were run at higher and higher supply pressures until the jet velocity reached 400 m/s. At that point, a small pressure spike was observed during ignition of the jet, but the chamber pressure leveled off to 1 bar when the jet velocity stabilized. Then, the nitrogen supply pressure was incrementally increased until the nitrogen dilution percentage of 15.0% was achieved and a lifted flame was generated. Finally, the exhaust valves were slowly closed until the pressure leveled off to 2 bar at the end of the test. Once all of these tests had been completed, the apparatus was deemed fully functional.

ii. *Numerical Methods*

a) Atmospheric Pressure Research

Flame speed, S_L, flame thickness, δ, and the chemical timescale corresponding to mixtures of jet reactants and co-flow products are calculated using Chemkin II PREMIX [27]. In PREMIX, mixtures of the jet and co-flow are pre-calculated and used as inputs which determined an overall global equivalence ratio $(\overline{\varphi}_{Global})$. Note that $\overline{\varphi}_{Global}$ is distinct from $\varphi_{co\text{-}flow}$. Mixture averaged properties are assumed. The flame thickness is defined as the region between 10% and 90% of the temperature difference between the burned and unburned sides of the premixed flame. An

example computation set of S_L versus $\overline{\varphi}_{Global}$ for cases with $\varphi_{co\text{-}flow}$ was fixed at 0.18 for four selected y_{N2} values is presented in Figure 12. A relationship between the laminar flame speed S_L, the mean local equivalence ratio $\overline{\varphi}_{Global}$ and y_{N2} is fit to the form $S_L(\overline{\varphi}_{Global}) = a\ \overline{\varphi}_{Global}^{\ b}\ exp(-c\ (\overline{\varphi}_{Global} - d))$ using data computed from PREMIX. The constants a, b, c and d are functions of y_{N2}. Note that the unburned mixture temperature varies with $\overline{\varphi}_{Global}$. The detailed H_2 chemical kinetic mechanism from Li et al. (2004) [30] [31] is used for all numerical simulations and equilibrium $T_{co\text{-}flow}$ and compositions are assumed. The fitting relation matches the computed laminar flame speed well, with an average error around 10% overall and with lower errors for the regions of interest. The chemical timescale is defined as the ratio of δ to S_L and is hereafter referred to as the flame time. These results are summarized in Figure 12. The computed flame time values are used in correlating experimental data.

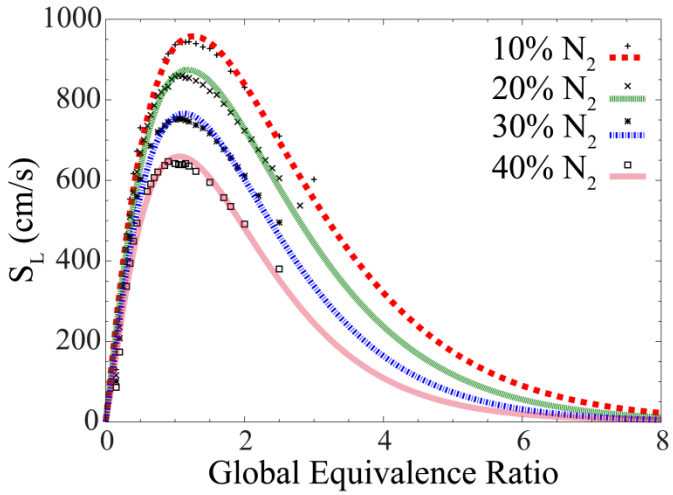

Figure 12: Computed laminar flame speeds versus jet N_2 dilution and global equivalence ratio and the correlation results plotted alongside (solid lines) for an example case with $\varphi_{co\text{-}flow}$ = 0.18.

The CHEMKIN results are used in developing liftoff height correlations as well as inputs to the RANS code detailed next.

The stability regime diagrams are also analyzed numerically. As the autoignition temperature of H_2 is slightly surpassed when $T_{co-flow}$ > 810 K [33], it is likely that both autoignition and flame propagation are present in the flame. A steady 1-D Reynolds Averaged Navier-Stokes (RANS) parabolic code is used to simulate the VCB. The RANS parabolic code allows for only autoignition in stabilizing the flame, and has been shown to reasonably predict flames where autoignition dominates simulated flame characteristics [11] [13]. Turbulence-chemistry interactions are modeled with a joint scalar-PDF approach, and mixing is modeled by the Linear Eddy Model, details of which are discussed in [34]. Post processing of the RANS parabolic code is conducted to allow a simplistic prediction of flame location based on a flame speed correlation, detailed below. The detailed H_2 chemical kinetic mechanism from Li et. al. (2004) [30] [31] is again used and equilibrium $T_{co\text{-}flow}$ and compositions are assumed. An approximate turbulent flame speed S_T is then computed using the following form from Muppala et. al. (2007) [35]:

$$\frac{S_T}{S_L} = 1 + \frac{0.46 Re_t^{0.25}}{e^{Le-1}} \left(\frac{u'}{S_L}\right)^{0.3} \qquad (2)$$

where, *Le* is the Lewis number, u' is the local turbulent fluctuating velocity and Re_t is the turbulent Reynolds number, defined as $Re_t = u'l/v$, where l is the local turbulence length scale and v is the local kinematic viscosity.

The RANS parabolic code is used by Frederick et. al. [37] in supporting experimental work to analyze the computed flow field and to determine regions where the local turbulent flame speed is greater than the local velocity. By comparing the local turbulent flame speed to the local turbulent mean axial velocity (<*U*>) maps of regions where S_T is greater than <*U*> are created. The regions where S_T > <*U*> indicate regions where a propagating flame is sustainable, so this method is useful for determining whether a stable flame is possible for regimes where propagation dominates stabilization.

The RANS method [37] also provides a rough estimate of lift-off heights based on flame propagation. This flame propagation approach is used in determining estimated liftoff heights where the minimum *z* location (regardless of radius) where an uninterrupted region exists with the computed turbulent flame speed greater than the local mean velocity is taken as the liftoff height. Note that the aforementioned approach computes the local velocity without a flame, and thus the intent is to capture trends more than details.

b) Elevated Pressure Research

Experimental liftoff height results from the elevated apparatus were correlated using the same methodology used for atmospheric pressure research. The pressure effect modifies the flame time computation, and not the flow time. With the elevated pressure research, the global equivalence ratio, $\overline{\varphi}_{Global,}$ is computed algebraically via Equation 3 instead of with CHEMKIN.

$$\bar{\varphi}_{Global} = \frac{0.5 + 2.38/\varphi_{co-flow}}{\left(1/y_{H_{2,G}} - \frac{y_{N_{2,j}}}{1 - y_{N_{2,j}}} - 1\right)\left(1/\varphi_{co-flow} - 1\right)} \qquad (3)$$

Equation 3 was derived by balancing the co-flow combustion reaction first, and then balancing the following combustion reaction of the jet reactants with the co-flow products.

3. Experimental Apparatus

i. *Atmospheric Pressure VCB*

The atmospheric pressure VCB consists of a high velocity jet issuing into hot co-flowing products of lean combustion, as shown in Figure 4. The inner diameter of the jet is d_{jet} = 2.4 mm, the outer diameter of the jet is d_o = 6.4 mm, and the outer diameter of the co-flow is D_o = 9.7 cm. The co-flow is generated with a perforated plate consisting of 348 (1.6 mm diameter) holes drilled into a 9.5 mm thick brass plate arranged in a hexagonal pattern with 4.8 mm separation between holes, and an overall blockage of 89%. The jet nozzle extends 25 mm above the base of the co-flow burner plate, and a 19 mm tall shroud is placed around the co-flow which reduces

outside air entrainment while maintaining visibility of the jet nozzle. Figure 13 shows a photograph of the Vitiated Co-flow Burner used in this research.

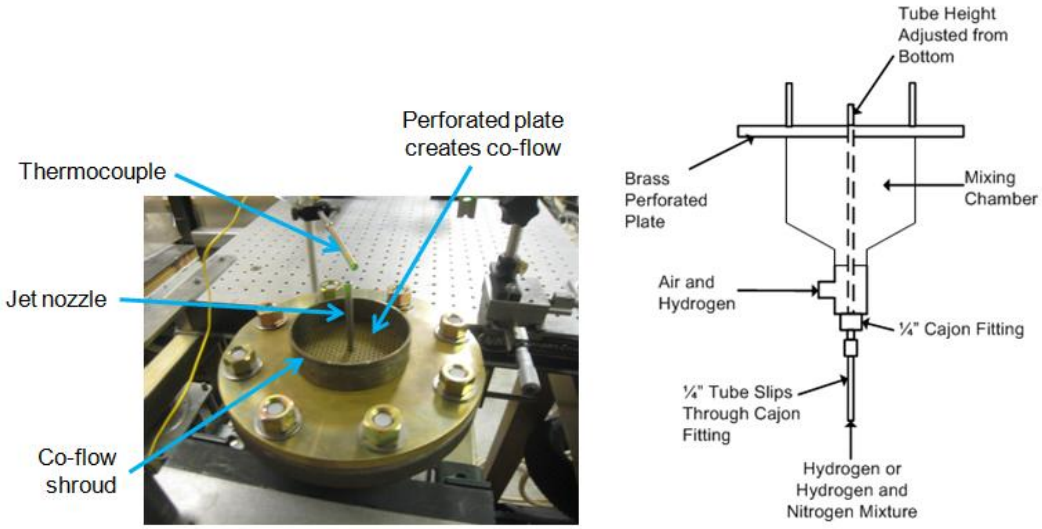

Figure 13: Photograph of the Vitiated Co-flow Burner used for atmospheric pressure research (left) and a profile view schematic of the burner.

A blunt-edge nozzle (also known as a squared-off nozzle) is used because early scoping work indicated that changing from a blunt edge nozzle to a tapered nozzle bears no discernible impact on the liftoff height *L*, which is the primary focus of the research. It is assumed that the insensitivity of liftoff height on nozzle geometry occurs because the liftoff heights generated with this burner configuration are sufficiently far away from the nozzle ($L/d \geq 10$ in all cases) for negligible liftoff height contributions from local recirculation effects around the nozzle exit. Since a blunt-edge nozzle facilitates modeling (primarily because meshing a square nozzle is significantly less complicated), a square nozzle is used.

Thin walled tubes are avoided in reducing heat transfer from the co-flow products to the jet reactants. Simple 1D heat transfer calculations where performed which show that even with the most conservative assumptions (1. outer wall tube temperature equaling the greatest co-flow temperature investigated of 1200 K, 2. pure hydrogen fuel, 3. a minimum jet velocity of 300 m/s), the fuel temperature would rise by only 28 K. The conservative nature of the assumptions invoked with this calculation indicates that fuel temperature increases in the jet nozzle are negligible.

The co-flow sizing is selected to be scale similar to Cabra's original design [24], even though the burner has been scaled down. The most important aspect of scale similarity is the ratio of the jet nozzle inner diameter to the co-flow diameter. Cabra performed flow investigations in ensuring that the co-flow stream remains unperturbed by outside air in the regions where the jet ignites. Otherwise, data gathered would be stochastic and difficult to model. Figure 14 shows this point pictorially.

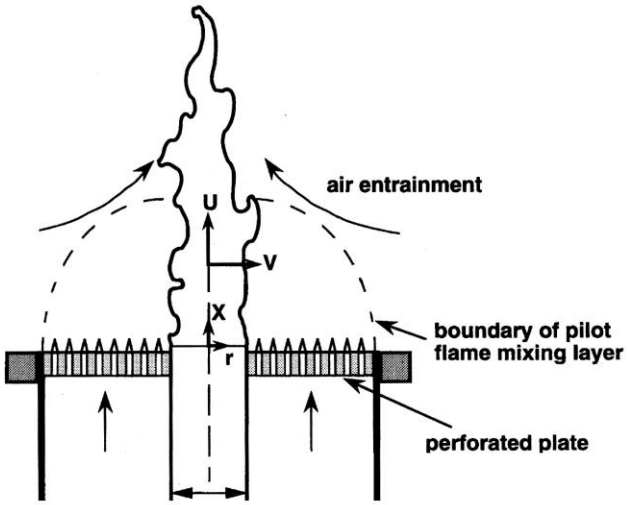

Figure 14: Drawing showing how the co-flow uniformity can be a function of distance from the co-flow outlet.

The region where the co-flow is unaffected by outside air is termed the potential core. The potential core height with this burner is ~42 jet diameters, which is greater than the greatest liftoff height measured in this research.

The flow rates of the reactants feeding the 1 bar burner are controlled by sonic flow orifices. To extend the dynamic range of flow rates that can be delivered with the sonic flow orifices, a system of three orifices in parallel has been implemented. The larger pipes on the left side of Figure 15 control the air flow rate to the co-flow while the orifices on the right control the flow rate for the hydrogen feeding the jet. The co-flow hydrogen flow rate and the nitrogen flow rate are controlled via single sonic flow orifices not shown in Figure 15. Each orifice in parallel can be decommissioned by closing a ball valve on both the air and hydrogen flow control orifices. This system allows a broad range of flow rates, and consequently equivalence ratios in the co-flow and velocities in the co-flow and jet to be delivered.

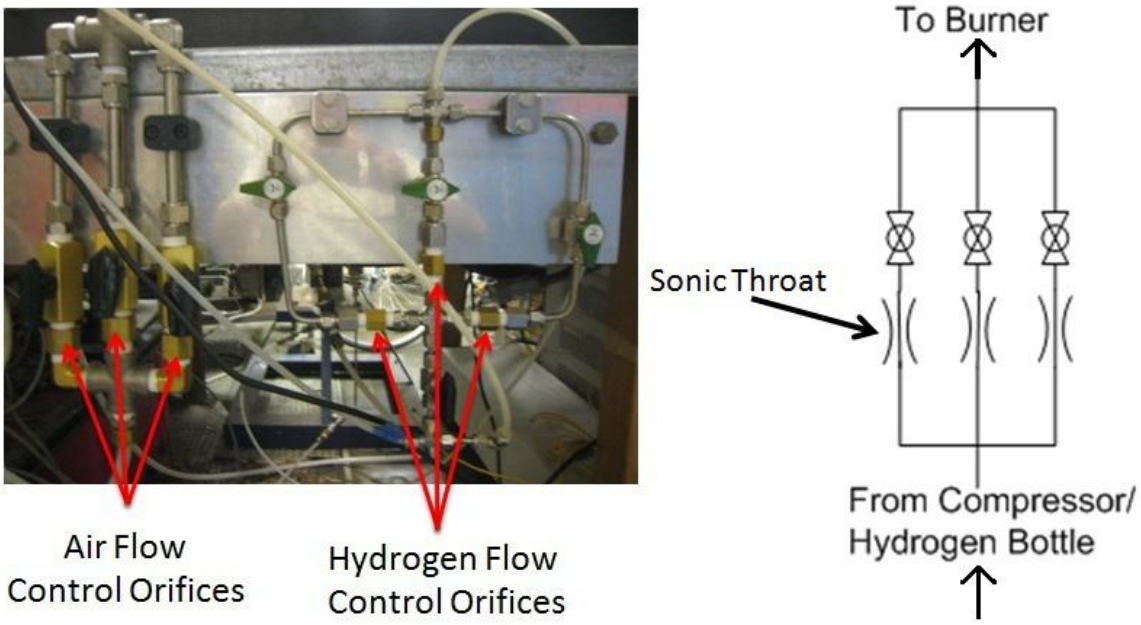

Figure 15: Sonic orifice flow control system used for the 1 bar burner.

Ensuring the flow rates delivered to the burner are accurately controlled and measured was an area of particular interest. Sonic flow orifices were selected for flow control due to their high dynamic range and repeatability. The delivered flow rate is unaffected by the downstream pressure with sonic orifices, so the upstream pressure is all that is needed to determine flow rate. The upstream pressure is measured by a pressure transducer that is read by the data acquisition system. Equation 5 shows the method by which the mass flow rate can be determined for sonic flow orifices.

$$\dot{m} = C_D A_{orifice} P_{upstream} \sqrt{(\gamma M/RT)(2/\gamma + 2)^{(\gamma+1)/(\gamma-1)}} \qquad (5)$$

where C_D is the discharge coefficient, $A_{orifice}$ is the area of the orifice at the narrowest point, $P_{upstream}$ is the pressure upstream of the orifice, γ is the heat capacity ratio, R is the universal gas constant and T is the upstream temperature.

Unfortunately, the discharge coefficient, C_D, is often unknown to sufficient accuracy and requires measurement. Since the easiest way to measure the discharge coefficient is to calibrate the orifices, calibrating the orifices was all that is necessary, eliminating the need to calculate C_D. The relationship between volumetric flow rate and upstream pressure was measured for each orifice and gas being used. The volumetric flow rate was then converted to mass flow rate using known gas densities. The volumetric flow rate was measured using a wet displacement flow meter.

ii. *Elevated Pressure VCB*

Following the completion of atmospheric pressure research, the VCB was redesigned for elevated pressure operation to operate in a transient mode, where the jet fires for a few seconds

for each test to avoid excessive heating of the pressure vessel walls. The reduced heat loads results in a significant reduction in the complexity of the design because the walls of the vessel do not need to be cooled. This section summarizes the detailed design of the elevated pressure VCB. As mentioned in section 1.iv, the overall original design of the elevated pressure burner has remained relatively unchanged from the atmospheric pressure version.

In the initial planning stages, several potential reactor designs were considered. During this period, a piece of hardware in the shape of a cross with 12.5 cm openings on each side was identified and deemed an ideal chamber starting point for the transient elevated pressure VCB. The cross is an ideal size to support the burner on one end, house the exhaust system on the other end, and provide viewing access for the imaging diagnostic on the other two ends. The cross is depicted in Figure 16.

Figure 16: 12.5 cm cross around which the elevated pressure burner was designed.

With the flange dimensions and the maximum size of the burner determined by the dimensions of the cross, many of the design constraints were already set. From there the inlet system, burner, exhaust system and viewing windows could be designed.

The finalized elevated pressure burner design is shown in Figure 17 through Figure 19.

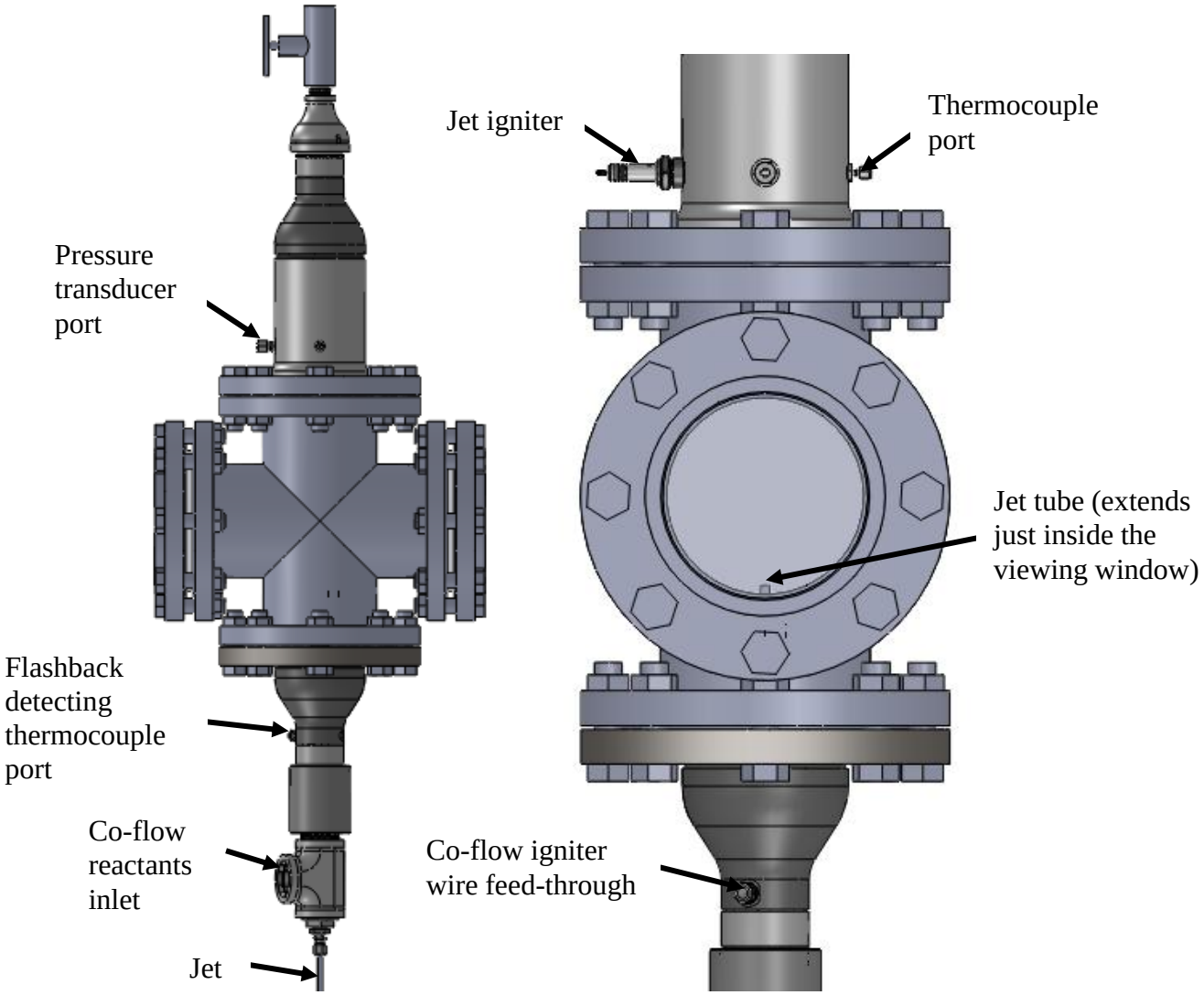

Figure 17: Front and side views of the final design of transient the elevated pressure VCB.

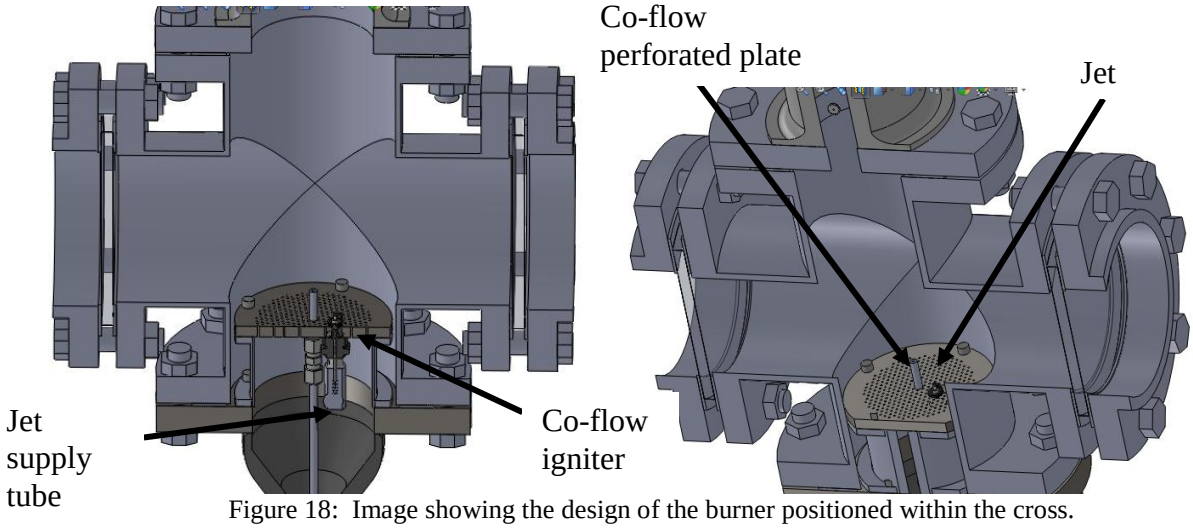

Figure 18: Image showing the design of the burner positioned within the cross.

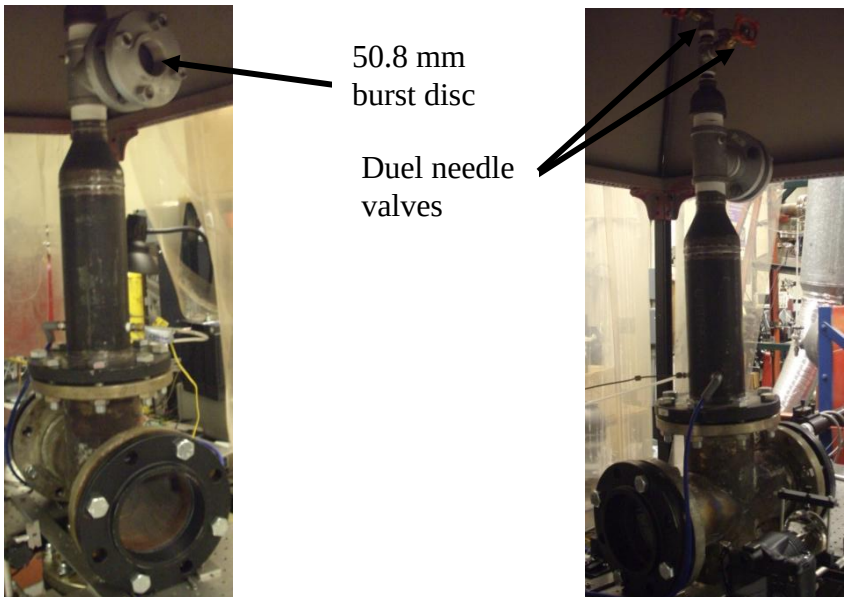

Figure 19: Fully assembled transient elevated pressure VCB.

The jet tube extends just inside the viewing window to maximize the height of the jet that can be viewed through the window while keeping the top of the tube in view so that liftoff heights can be measured directly from the images gathered. Also, the burner co-flow perforated plate was positioned to extend into the cross so that the jet tube nozzle can be as short as possible to avoid high pressure drops associated with the small jet diameter (2.4 mm). The perforated plate perforation pattern is identical to the atmospheric pressure burner design.

The igniter shown in the model is slightly different from the one actually used as it was found through initial testing that a standard spark plug does not extend far enough into the co-flow to achieve reliable ignition. The actual igniter used is shown in Figure 20.

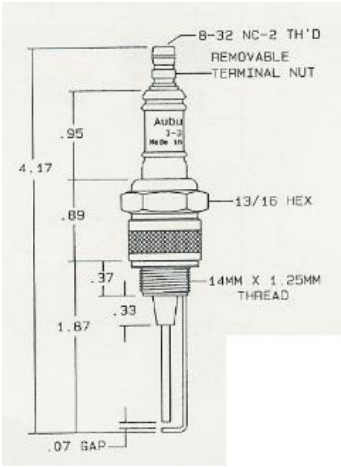

Figure 20: Final spark igniter used to light the co-flow.

The jet supply tube inner diameter is different than the jet nozzle inner diameter for minimizing the pressure drop resulting from the high velocities targeted in the jet. The inner diameter of the jet supply tube is 4.6 mm (versus the inner diameter of the nozzle of 2.4 mm). All machined

parts were manufactured by a local machine shop in Berkeley, CA. The burner in various states of assembly is shown in Figure 21.

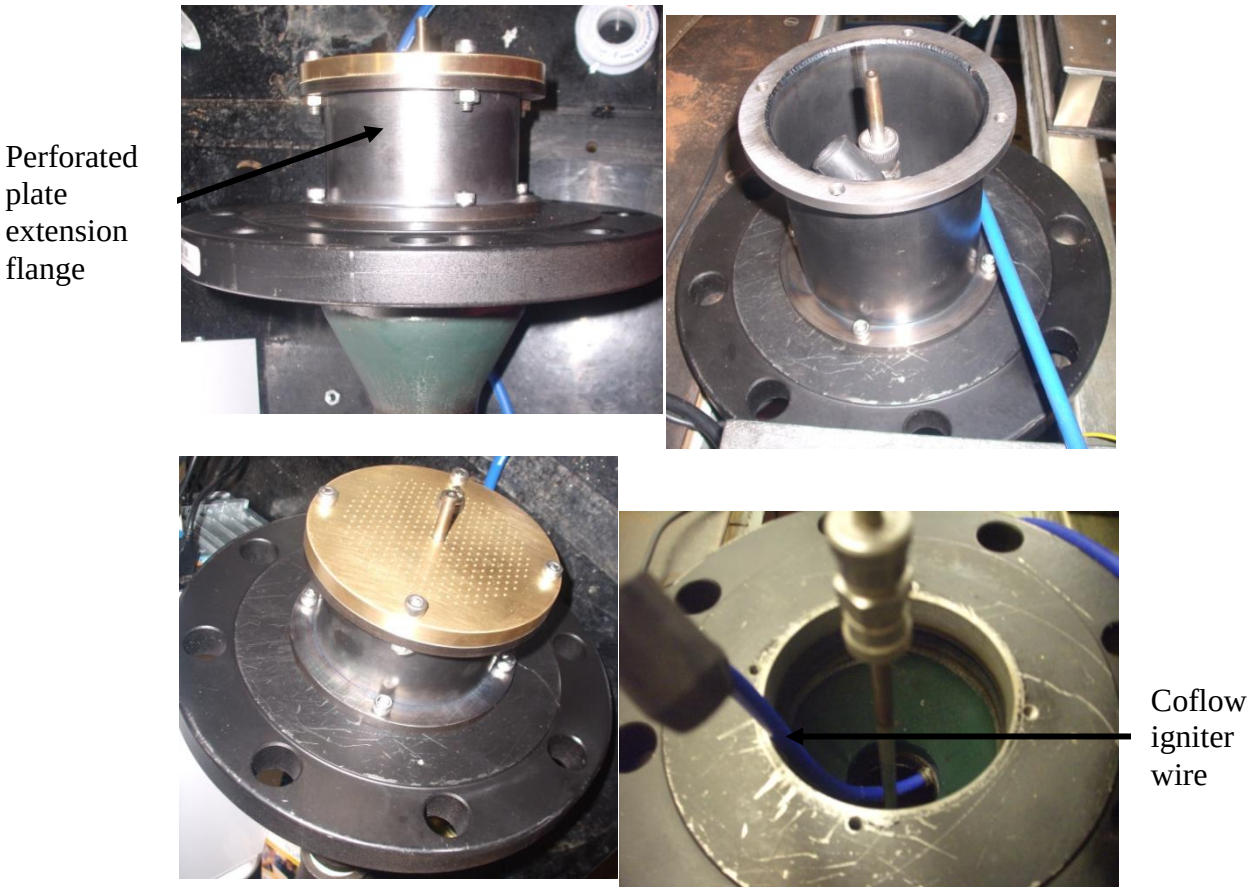

Figure 21: Elevated pressure VCB in various states of assembly.

The co-flow igniter wire feeds though the inlet manifold and the connection to the igniter are made while the perforated plate is being mounted to the perforated plate extension flange. The entire assembled inlet manifold is shown in Figure 22.

Figure 22: Inlet manifold assembly.

An image of the cross mounted in its final position is shown in Figure 23.

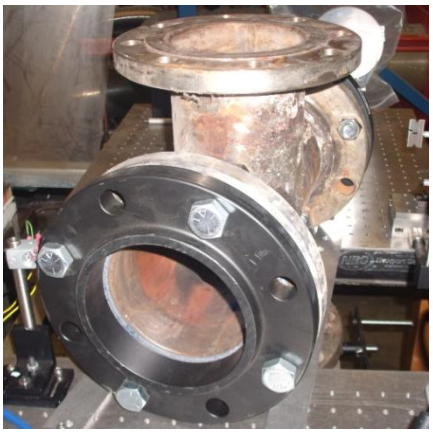

Figure 23: 12.5 cm cross mounted and aligned with the imaging system.

The transient elevated pressure VCB with all components included is shown in Figure 19. A burst disc is included into the system to avoid breaking the quartz windows in the event that an ignition event results in a pressure spike that would exceed the maximum pressure that the windows can withstand (16 bar). The burst pressure of the burst disc used was selected to be 4.4 bar. A cylinder of high temperature insulation was placed on the inside of the burst disc to keep it cool so that it would not burst prematurely. It was also decided to involve 2 needle valves to control the pressure of the vessel. One needle valve provides coarse pressure control, while the other needle valve provides fine pressure control. The dual needle valve arrangement is also necessary for the highest jet velocities and co-flow equivalence ratios investigated because a large enough single valve could not be found that can keep the pressure of the vessel near

atmospheric for the most extreme tests. This capability was necessary to be able to complete all planned tests. These features are also pointed out in Figure 19.

a) Elevated Pressure Burner Design Evolution

Experimental progress and subsequent troubleshooting efforts led to several upgrade implementations to the burner and control system. Many of these upgrades are explained briefly, with no further information needed. The most notable upgrades include a redesign of the jet nozzle and the implementation of a co-flow shroud, improvements to the ignition system, improvements to the burner control and fluid delivery system and improvements to the imaging system.

Nozzle Tapering

A 15 degree tapered nozzle was investigated in the effort to increase the lifted flame range. The taper is intended to extend the lifted range to potentially higher co-flow temperatures because the recirculation zone near the blunt edge bluff body may tend to cause an attached flame at higher nitrogen dilution percentages than a tapered nozzle would. Figure 24 shows the original and tapered designs of the nozzle.

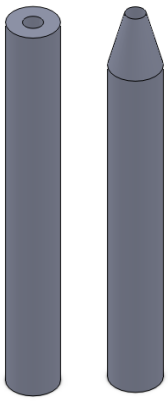

Figure 24: Original (left) and tapered (right) nozzle configurations.

Atmospheric pressure results (not presented) indicated that while the stability regimes diagrams may differ between the two nozzle configurations (not fully investigated), the value of the liftoff height for the lifted regime appears unchanged between the two nozzles. Additionally, the tapered nozzle does not facilitate the generation of lifted flames at higher co-flow temperatures, contrary to expectations. Since meshing the tapered nozzle geometry for CFD is challenging, and therefore modeling the lifted case is more complicated than the square edge nozzle, the original square edge nozzle was opted finally for use with all reported data. A direct comparative study was performed which demonstrates that the tapered nozzle presents no significant advantage to this research.

Co-flow Shroud Implementation

In the effort further resolve the issue regarding the inability to produce lifted flames at co-flow equivalence ratios greater than 0.20, an investigation was conducted in characterizing the co-flow temperature, and it was determined that the position of the fixed thermocouple that measures the co-flow temperature is too far downstream of the co-flow to get an accurate measurement of the co-flow temperature. To more accurately characterize the co-flow temperature with confinement versus position and co-flow equivalence ratio the following steps were taken:

1. The windows were removed and the co-flow temperature was characterized at various positions
2. The temperature was still much lower than it was without confinement, and much lower than the equilibrium temperature
3. A methane tracer was added to the co-flow, and it was found that only ~ 5 cm of the center core of the 10 cm diameter co-flow was burning
4. Several example shrouds were constructed in the effort to solve the problem and it was determined that when a shroud is 1.9 cm tall, and surrounds co-flow as tightly as possible, the co-flow can burn fully with an equivalence ratio as low as 0.15. A shroud any taller than 19 mm would make viewing the tip of the nozzle difficult, thereby making liftoff height measurements more difficult and less accurate. The resulting co-flow shroud is depicted in Figure 25.

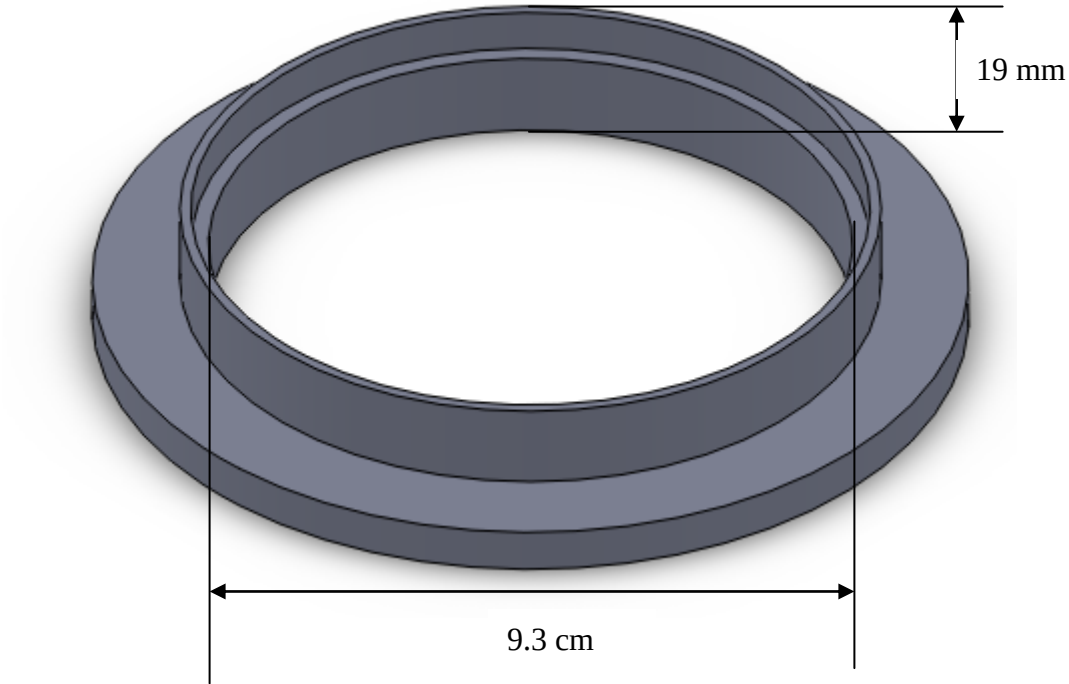

Figure 25: Co-flow shroud used for elevated pressure burner.

The shoulder on the inside of the shroud was needed to close the gap between the "stock" diameter of the tube used to form the shroud and the actual co-flow outer diameter, which is needed to ensure efficient co-flow combustion with low co-flow equivalence ratios.

With the co-flow burning hotter resulting from increased combustion efficiency due to the addition of the shroud, it was found that it is very difficult to achieve a steady lifted flame with co-flow equivalence ratios greater than 0.15. With the shroud, the co-flow is presumably hotter with confinement than without, so it is reasonable to assume that the co-flow temperature at a co-flow equivalence ratio of 0.15 with confinement is closer to the case without confinement when the co-flow equivalence ratio is 0.20. Peters [17] explains that larger jet diameters can produce steady lifted flames with higher co-flow temperatures due to reduced strain rates with equal jet momentum values. In keeping experimental results consistent with atmospheric pressure results, the jet nozzle inner diameter was nonetheless kept at 2.4 mm, with the negative consequence of limiting the equivalence ratio range where stable lifted flames may be generated with confinement.

Ignition System

Extensive work in optimizing the ignition system was performed. First, a solid state relay was added to actuate the ignition coils. Originally, the ignition coils were actuated with the National Instruments SPDT relays included in the DAQ board. It was discovered that the current needed for ignition was greater than the rated limitations of the SPDT relays. The SPDT relays consequently periodically failed to switch consistently, which presented a safety risk (delayed ignition causes over-pressurization). The relay addition also significantly decreased the amount of time that the reactor needs to reach steady state pressures because the jet ignites sooner, which reduces the ignition pressure spike, allowing shorter jet durations to be used. The relay selected is shown in Figure 26.

Figure 26: A solid state relay similar to the one installed to actuate the ignition coils. Image source: omega.com

Figure 27 through Figure 30 show representative pressure traces for experiments conducted without the relay and with the relay as well as traces in jet velocity, supply pressures, flow rates, and the jet control signal timings for the case with the new relay.

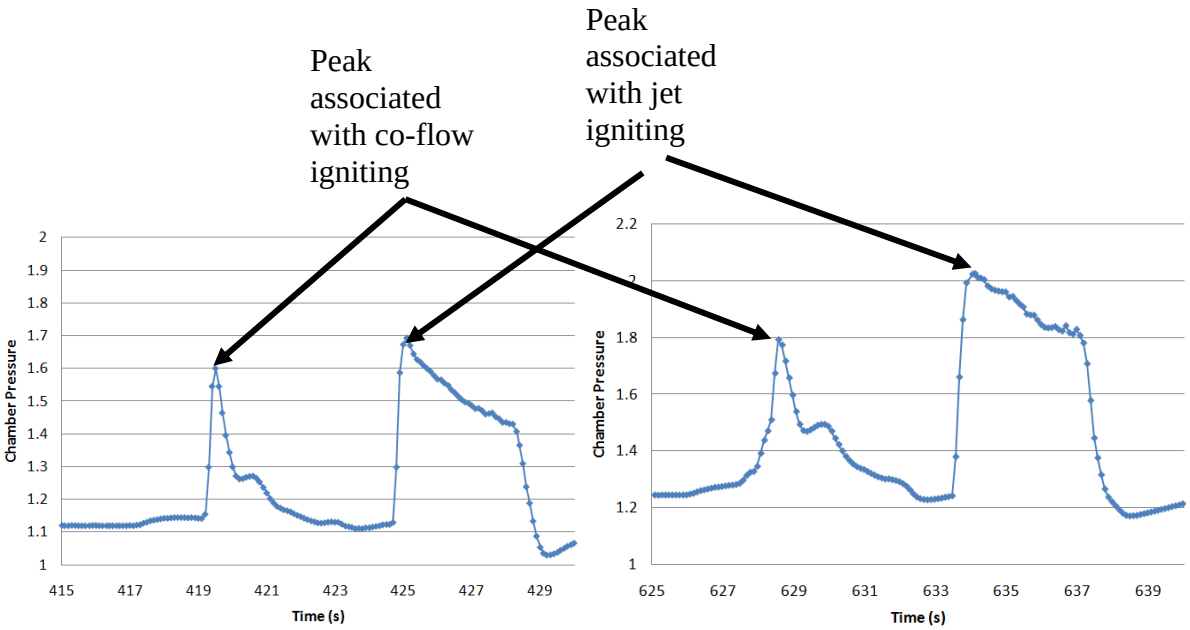

Figure 27: Representative tests showing the pressure trace during ignition of the co-flow and jet for pressure targets of 1.4 bar (left) and 1.8 bar (right) with original burner ignition system

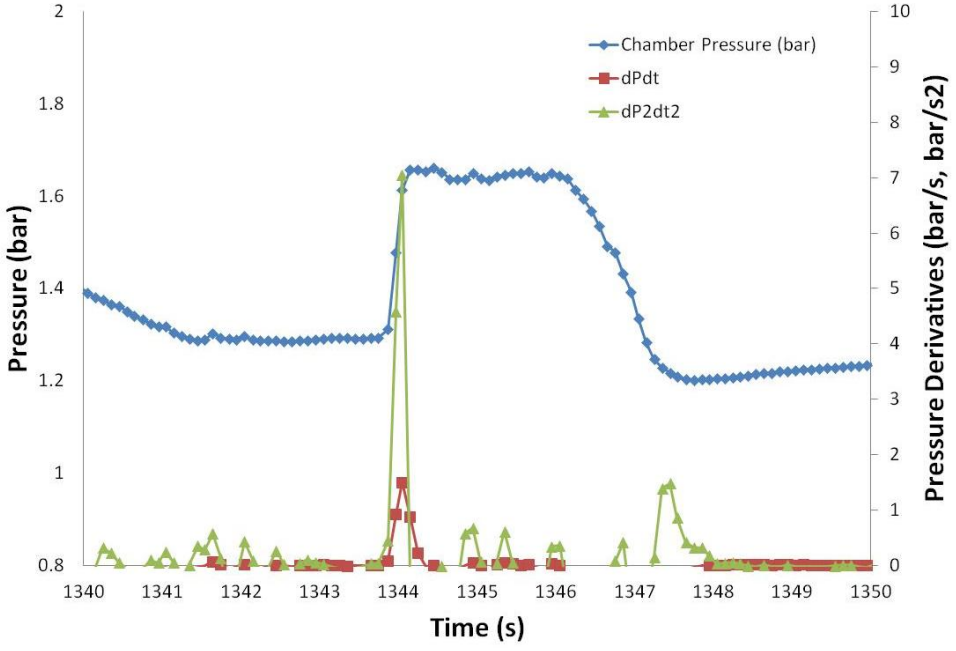

Figure 28: Jet ignition pressure trace (and derivatives thereof) from a representative test with the improved ignition system.

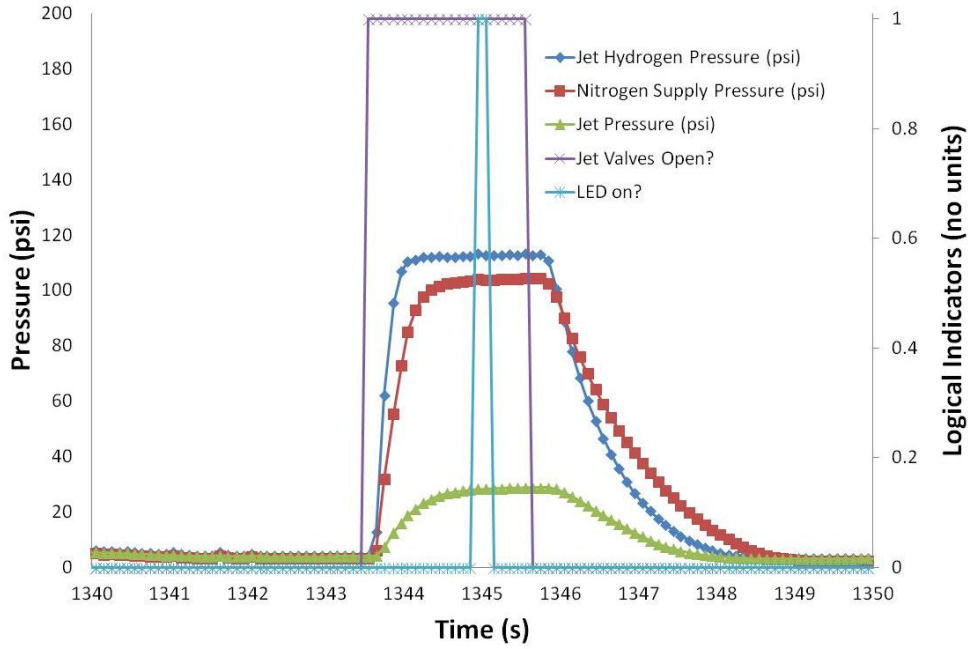

Figure 29: Just supply pressure traces and control system logic values during a jet ignition event from a representative test with the improved ignition system.

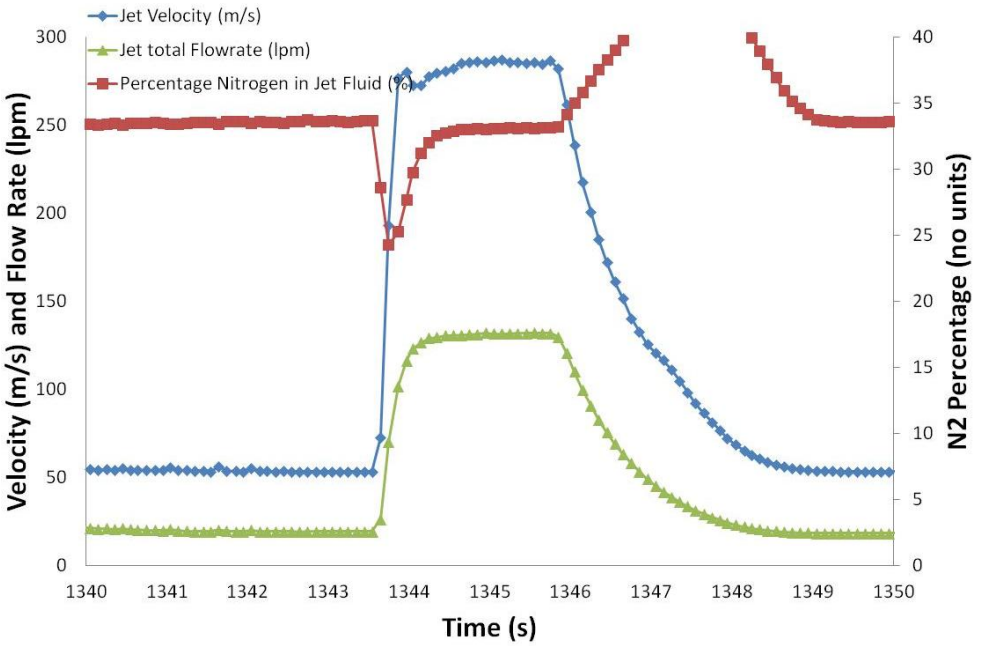

Figure 30: Traces of jet velocity, jet flow rate, and nitrogen dilution percentage during a jet ignition event from a representative test with the improved ignition system.

Signal transients were significantly reduced with the improved ignition system.

Finally, a trickle charger was added to the ignition system which charges the battery during testing to ensure that the battery is always at maximum charge for continuous reliable ignition.

In addition to reducing ignition transients, this improvement also reduces the risk of delayed ignition resulting from low battery voltages, which can also cause over pressurization.

Flow Delivery Upgrades

Several improvements to the burner flow delivery system were made during the initial testing phases. Firstly, the supply lines for the hydrogen jet (H_2 and N_2) were upgraded with copper tubing (originally nylon tubing) and new pressure regulators were installed which deliver pressures up to 18 bar to the sonic flow control orifices, instead of the original regulators which could not deliver pressures greater than 7.8 bar. Also, the original single N_2 flow control orifice was replaced by three orifices in parallel (each can be blocked by closing manual ball valves) for greater dynamic range in jet nitrogen mole fraction and jet velocity over the pressure range of interest. These improvements increased the dynamic range of the system (in terms of both pressure and velocity) significantly, and reduce the likelihood of encountering non-sonic conditions in the orifices.

In ensuring that the co-flow flow-field is uniform, a flow straightener was added to the co-flow mixing chamber. This addition was intended to troubleshoot an issue observed where large fluctuations in liftoff height occurred when the co-flow equivalence ratio was increased. A helical mixing tube was also added to the co-flow supply lines with the purpose of ensuring that the hydrogen and air are well mixed upstream of the flow straightener. Minor additions to the flow delivery system include the addition of a manual shut-off valve at the end of the jet supply line to allow rapid leak checking and a hard-wired emergency shut-off switch installed to allow rapid shut-down of the experiment in the case of an emergency situation.

iii. *Steady State Elevated Pressure Burner Design*

In addition to the transient elevated pressure burner, a version of the burner capable of operating in a steady state mode was also designed in keeping with initial plans of eventual steady state investigations. Steady state operation requires significant implementation of expensive cooling systems. Consequently, the steady state version of the burner has not been fabricated. The design is nevertheless presented here for completeness.

A pressure vessel which satisfies the design constraints needed for the intended research was first identified which is suitable for regulating the environment pressure up to 8 bar at wall temperatures up to 470 K. This pressure vessel is complete with a back pressure valve, piping and flow control for various gases, and instrumentation for a wide variety of investigation types. The pressure vessel is capable of operating at pressures up to 8 bar with a maximum wall temperature of 470 K. The wall temperature limitation is most important for the optical windows, but was also placed on the stainless steel walls for safety because the strength of stainless steel as a function of temperature can vary among various samples of stainless steel. The vessel contains 12 window ports; 4 rectangular ones closest to the burner and 8 circular ones further downstream. The 4 rectangular windows were anticipated to be the ones most useful for instrumentation/viewing for this research because these windows are in the region where the liftoff height and other characteristics are of primary interest may be observed. The vessel is shown in Figure 31.

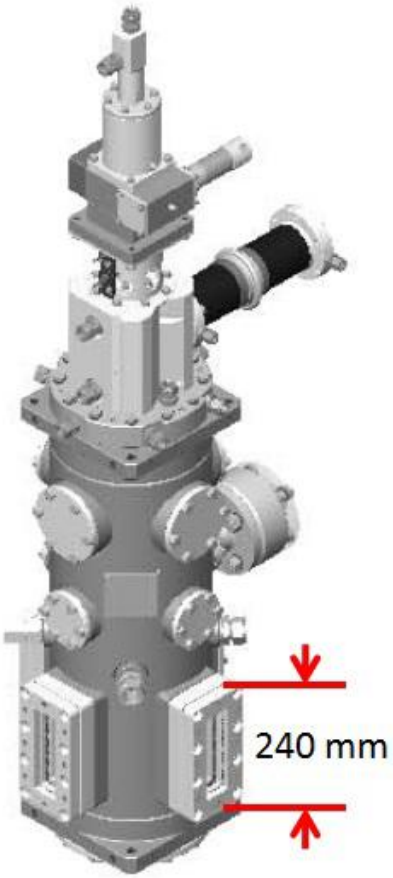

Figure 31: Existing pressure vessel into which the vitiated co-flow burner would mount.

The burner purposed designed for this vessel replaces an existing experimental apparatus at the bottom of Figure 31. The majority of the design task, then, was to design a burner that 1) fits within the size constraints given by the pressure vessel, 2) is capable of traversing the range of operating conditions of interest, and 3) incorporates adequate cooling to keep the outer walls and windows below 470 K.

Since the pressure vessel was already available, a fairly extensive list of design constraints was already in place. The geometrical constraints are summarized below:

1. The inner diameter of the existing pressure vessel walls is 240 mm. This constraint could not be ameliorated. The burner, instrumentation, and all cooling systems needed to fit within this diameter.
2. The apparatus had to be able to slide into place through a 190 mm diameter opening near the inlet as shown in Figure 32.

These geometrical constraints ultimately limited the size of the co-flow, limiting the degree by which the co-flow flow field could be approximated as uniform flow along the axis of the combustor. Since the flow characteristics need to be independent of the distance from the co-

flow outlet for meaningful data collection, the diameter of the co-flow was maximized in ensuring that the liftoff height is not affected by a varying co-flow flow field.

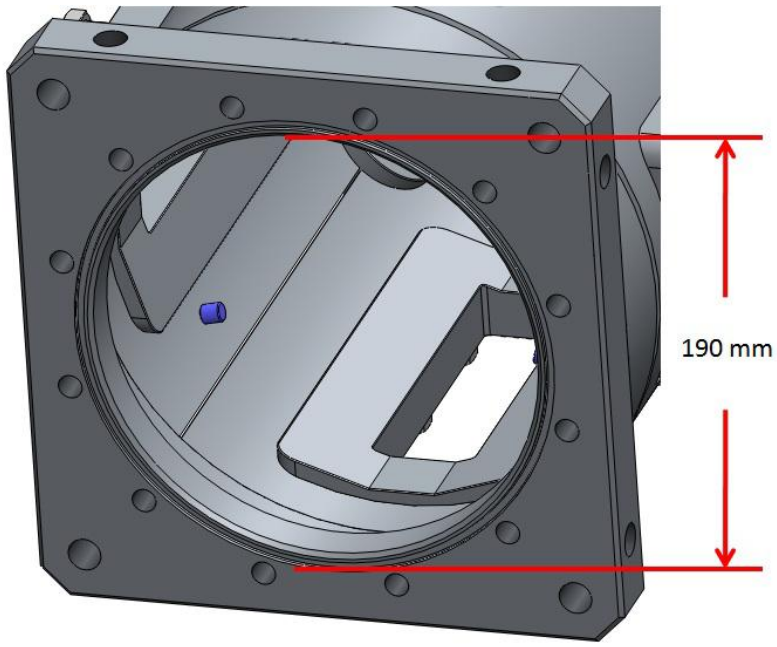

Figure 32: Pressure chamber opening through which all burner components needed to fit.

Additionally, the design was constrained by restrictions on the various maximum flow-rates that could be delivered by the gas delivery system, which was also fixed. The flow rate constraints are summarized below:

1. The maximum air flow rate is 150 g/s.
2. The maximum CO_2 flow rate is 83.2 g/s.
3. The maximum hydrogen flow rate is 3.6 g/s.
4. The maximum nitrogen flow rate is 6.3 g/s.

These flow rate limitations ultimately limited the range of operating conditions that could be tested, but they also affected the most effective design in making geometrical design decisions. The following summarizes the manner in which design decisions are affected by the flow rate constraints:

1. The overall diameter of the co-flow needed be selected such that the velocity through the perforations is high enough to prevent flashback. Since the maximum velocity is also dependent on the maximum air flow rate that could be delivered, the flow rate restriction influences the design choice on the co-flow diameter.
2. The maximum velocity of the jet is dependent on the jet inner diameter and the maximum hydrogen flow rate. Consequently, the choice of jet inner diameter was affected by the maximum hydrogen flow rate that could be delivered.
3. The cooling effectiveness of the cooling system is dependent on the heat release rate which is proportional to the maximum hydrogen flow rate. Consequently, the

cooling system design depended on the maximum hydrogen flow rate that could be delivered.

The jet tube was designed fully adjustable in height and the jet inner diameter was designed variable from 0.093" to 0.18" by replacing the tube with others of different inner diameters but the same outer diameter of 0.25". The cooling manifold design ensured that equal flow of CO_2 would be delivered to each of the four double walled windows. Figure 33 shows a view where the cooling jacket design can be viewed more easily.

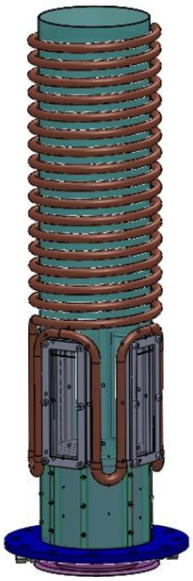

Figure 33: Isolated view of the steady state elevated pressure VCB cooling jacket.

The outer diameter of the cooling jacket design is 12 mm and the inner diameter is 10 mm. The cooling jacket design accommodates a flow rate of 0.45 kg/s, resulting in a total pressure drop of 3.7 bar, which can be accommodated by the water supply. At this flow rate, the water is capable of removing 56% of the total maximum heat load of 270 kW. It was assumed that this cooling capacity is more than enough to absorb the heat load that the cooling jacket would encounter, but experimental validation of this assumption would still be needed.

The flow begins at the bottom of the device. The cooling jacket traverses the space between windows twice per gap between windows to ensure that radiation heat transfer from this area does not occur excessively between the heat shield and the outer wall in this region. The area below the cooling jacket would not be heated by combustion so it was not designed with any cooling systems attached.

Figure 34 shows two close up views of the double walled window cooling design. The walls are 45 mm wide, 267 mm long, and the space between windows is 12.3 mm in thickness. This thickness establishes a workable balance between generating high convection coefficients, and keeping the outlet temperature of the coolant below untenable levels. The thickness choice was part of the optimization process.

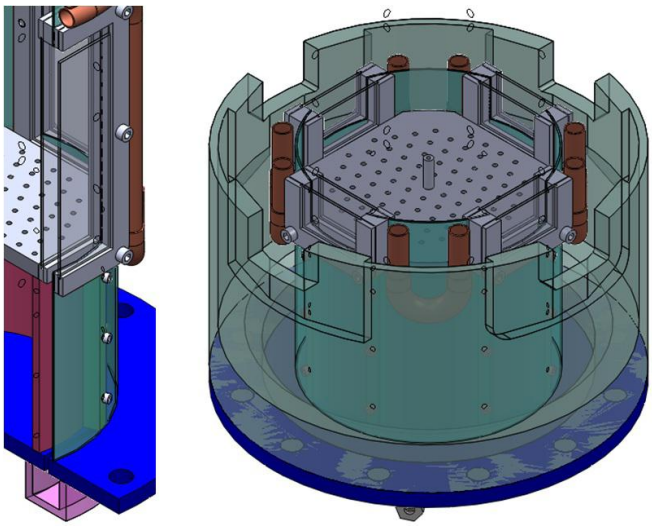

Figure 34: Close up view of the double walled window cooling system.

The flow rate design constraints are summarized in the Process Instrumentation Diagram (PID) shown in Figure 35. The gas flow rates are regulated with mass flow controllers with appropriate capacities. The CO_2 flow path illustrated is significantly distinct from what would be used for this research, since the CO_2 would only be used as a coolant for this research whereas it was used as a research gas in the original purpose of the device. Nonetheless, the flow control mechanism provides adequate control over a sufficient range of flow rates for the purposes of this research. All control systems are monitored and controlled via the Automatic Burner Controller (ABC) shown at the bottom of Figure 35. Similar to the burner chamber, the ABC was adapted for this research.

A section view of the final version of the steady state VCB design is shown in Figure 36.

Steady State Elevated Pressure VCB Diagnostics Strategy

The diagnostics strategy needed to be reconsidered with the steady state apparatus in making full use of the steady state capabilities. It was important to ensure that data gathered from experimental investigations are sufficiently accurate and thorough for model validation. Both schlieren imaging and line of sight OH* chemiluminescence measurements were selected as initial diagnostics options for model validation. Since schlieren imaging is also used in the atmospheric pressure research, the technique is not detailed here.

Line of sight OH* chemiluminescence was selected for its ability for capturing the formation and growth of ignition kernels. With this approach, a band pass filter would be used, which would only allow light which is at a wavelength similar to that of the first vibrational excitation frequency of OH* to pass through. The transmission spectrum for the chosen band pass filter is shown in Figure 37.

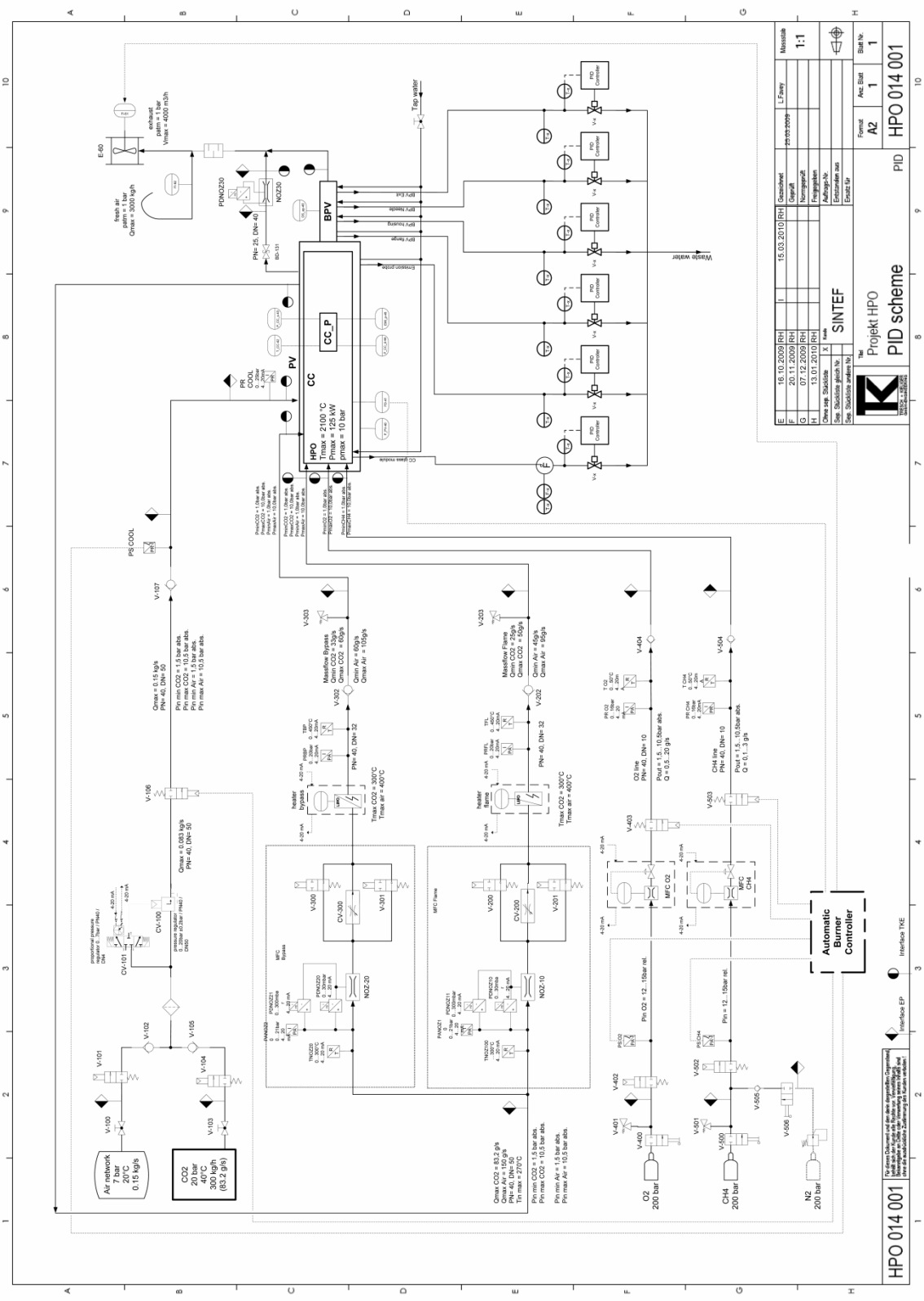

Figure 35: Process Instrumentation Diagram for the original elevated pressure system.

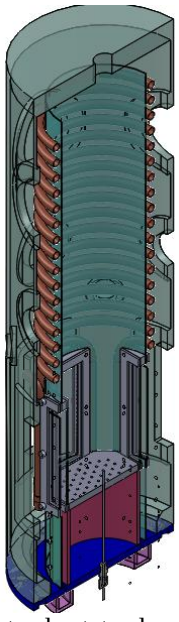

Figure 36: Section view of the steady state elevated pressure VCB final design.

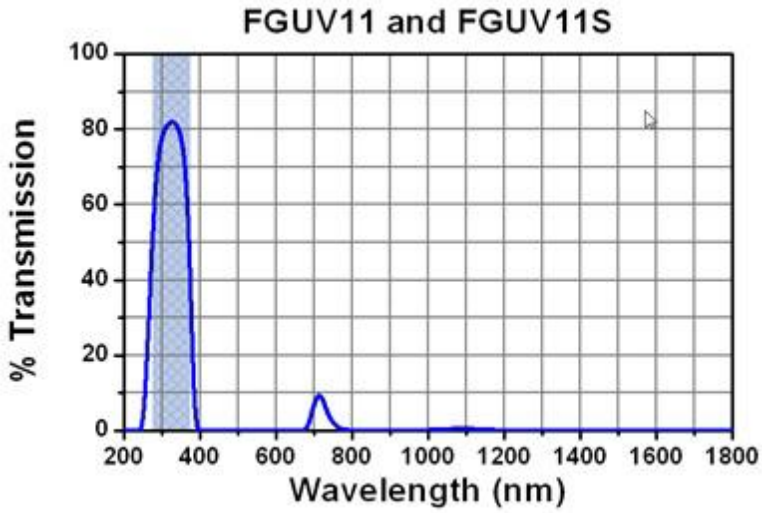

Figure 37: Transmission spectrum for band pass filter suitable for OH* chemiluminescence measurements.

Two sequential pinholes would be strategically placed before this band pass filter to ensure that the measured light intensity at this frequency range only comes from one point (including the depth into the flame from which the light originated). By moving the OH* chemiluminescence measurement system over the problem domain, it becomes possible to obtain an approximate measure of the OH* concentration at every point of interest in the flame. If it is then assumed that the OH* concentration is axis-symmetric (which can be enforced by careful filtering in the azimuthal direction), an Abel deconvolution algorithm may be invoked with the gathered data to obtain OH* concentrations that are a function of *r* and *z* only. The OH* chemiluminescence measurement system would be tested at atmospheric pressure before use at elevated pressure. A conceptual drawing of the OH* measurement system is shown in Figure 38.

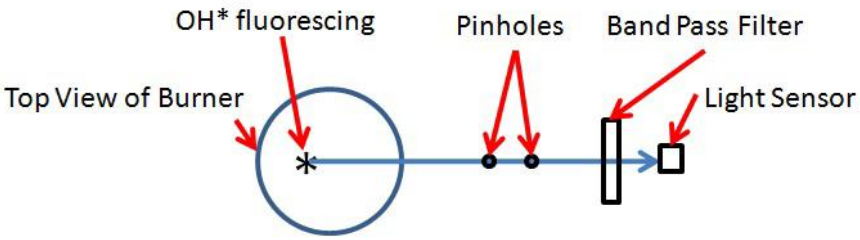

Figure 38: Drawing of the line of sight OH* measurement system concept.

Flashback Arrestor Implementation

A ceramic honeycomb flashback arrestor was designed and implemented into the design of the steady state elevated pressure VCB. The flashback arrestor is shown in Figure 39.

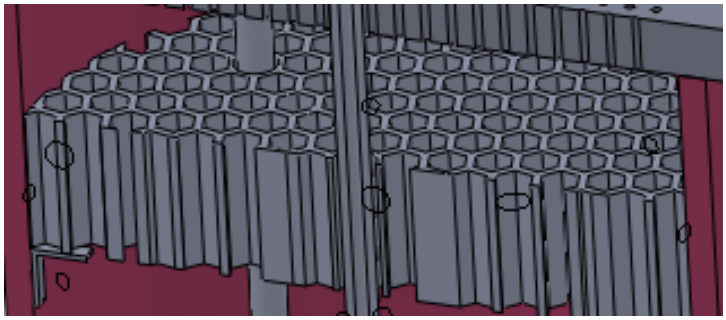
Figure 39: Honeycomb flashback arrestor designed for the steady state elevated pressure VCB.

This device limits the volume of premixed reactants that can ignite in the event that the reactants propagate upstream through the perforated plate.

Extended Spark Igniter Implementation

The transient elevated pressure VCB igniter design would have been cumbersome to install in the new pressure vessel infrastructure. Consequently, an analogous ignition system was designed on the co-flow burner to streamline the installation process. The redesigned igniter is shown in Figure 40.

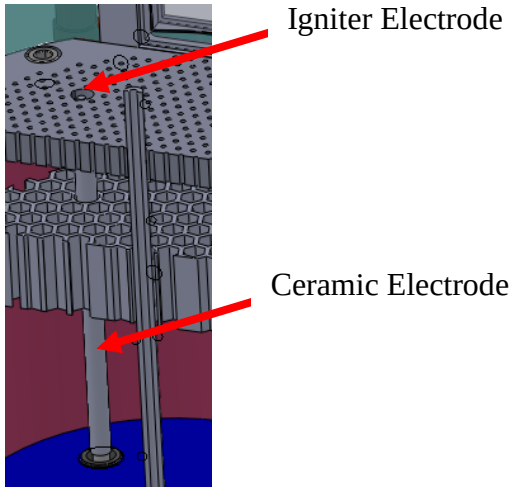

Figure 40: Extended spark igniter.

The design improvement is also less intrusive to the flow field than the original design.

Computational Work Supporting Elevated Pressure Reactor Design

In the process of designing the steady state elevated pressure burner, extensive computational work was necessary to identify a reasonable set of operating conditions for the burner and in facilitating the design of a cooling scheme that would keep the outer walls below the 470 K limitation. This computational work is summarized here.

It was first necessary to determine the total heat load that the cooling system would need to handle. This effort was carried out in an iterative manner, involving several changes in operating conditions and subsequent redesigns of the cooling system. The first step in this process was in determining the total hydrogen flow rate that could be expected. Equation 6 shows the chemical reaction for lean combustion of hydrogen with air.

$$H_2 + 0.5\,(O_2 + 3.76 N_2) \rightarrow H_2O + 0.5\,(1/\varphi - 1)\,O_2 + 1.88/\varphi\, N_2 \qquad (6)$$

This reaction expression was used to select a maximum overall (including the jet hydrogen) equivalence ratio that could be allowed at 8 bar, which would be the highest hydrogen flow operating condition, and thus results in the highest heat load. After several iterations, it was decided that a maximum overall equivalence ratio of 0.66 is tolerable and still provides a broad range of operating conditions to be studied. This operating condition involves a co-flow equivalence ratio of 0.27, with a jet velocity of 400 m/s. The resulting total hydrogen mass flow rate is 2.24 g/s.

Equation 7 can then be used to calculate the total Heat Release Rate (HRR) that can be expected under these conditions.

$$HRR = LHV_{H_2}\,\dot{m}_{H_2} = 121\ MJ/kg \times 0.002238\ kg/s = 270\ kW \qquad (7)$$

where LHV_{H2} is the lower heating value of hydrogen. The cooling system needed to be able to accommodate a maximum HRR of 270 kW under the most stringent operating conditions (8 bar). This value was thus used for the design of the cooling system.

With the total heat load known, an algorithm was developed for quick calculation of the outer wall temperature for a given set of operating conditions. One of the many iterations conducted throughout the design process is now chronicled. This example case involves a single heat shield with single heat shield windows separating the combustion section from the cooling section (see Figure 41). The cooling section is then between the heat shield and the outer pressure vessel walls. CO_2 coolant flows through the cooling section, keeping the outer pressure vessel walls below the maximum temperature threshold.

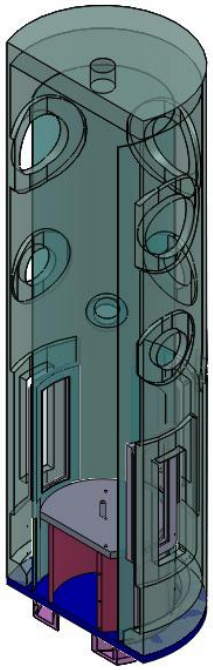

Figure 41: Early design of the steady state elevated pressure burner situated within a mock-up of the pressure vessel. This design incorporates a single walled window heat shield with coolant flowing between the heat shield and the pressure vessel walls.

A few important assumptions are made in this analysis:

1. The heat shield temperature is isothermal at 1200 K and at the temperature of the co-flow. This is the maximum temperature that the heat shield could be at, so this assumption is conservative.
2. The primary mode of heat transfer between the coolant and the outer wall and between the coolant and the heat shield is by convection.
3. Radiation heat transfer dominates heating of the outer wall emanating from the heat shield.
4. The specific heat capacity of the coolant can be assumed constant along its flow path.
5. The coolant head loss over its flow path in the chamber represents a negligible change in density.
6. Radiation absorption by CO_2 in the cooling section can be neglected (conservative assumption).

With these assumptions, it was possible to develop a heat transfer correlation which can be used to determine the mass flow rate of coolant necessary to maintain the pressure vessel wall temperature at or below the 470 K limit. The solution methodology is as follows:

1. Assume the mass flow rate necessary to absorb the heat load (initial guess, actual value to be determined recursively).
2. Determine the resulting convection coefficient via several Nusselt Number correlations (Dittus Boelter (Incropera, 2006) [38], Gneilinski-Petukhov

(Petukhov, 1970) [39], Gnielinski (Gnielinski, 1975) [40], laminar/turbulent superposition (Gnielinski, 1975) [41]).

3. Find the final mid-temperature resulting from this convection coefficient.
4. Find the mass flow rate necessary to match the radiation energy flux between the heat shield and the outer wall.
5. Use Newton's method to converge the calculated mass flow rate with the initial guess iteratively. This iteration was done independently for each convection coefficient correlation.

As noted above, several convection coefficients were used in this analysis for comparison. Each convection coefficient relation is listed below:

1. The Gnielinski correlation [40] below is valid for $3000 < Re_D < 5 \text{ X } 10^6$.

$$Nu_{tube} = \frac{{}^{f}/_{8}(Re_D - 1000)Pr}{1+12.7\frac{f}{8}^{1/2}(Pr^{2/3}-1)} \qquad (8)$$

where f is defined by Equation 9:

$$f = 1 / (1.82 \log(ReD) - 1.64)2 \qquad (9)$$

2. The second Nusselt number relation used is the Petukhov - Gnielinski correlation [39], which is valid for $Re_D > 2300$:

$$Nu_{tube} = \frac{{}^{f}/_{8}(Re_D - 1000)Pr}{1+12.7\left({}^{f}/_{8}\right)^{1/2}(Pr^{2/3}-1)}\left(1 + {}^{D}/_{L}\right)^{2/3} \qquad (10)$$

The Petukhov - Gnielinski correlation is a modification of the original Gnielinski correlation which accounts for entrance effects.

3. The third correlation used is a superposition of a correlation for laminar flow and turbulent flow [41]:

$$Nu_{superposition} = 0.3 + \sqrt{Nu_{lam}{}^2 + Nu_{turb}{}^2} \qquad (11)$$

The superposition correlation is valid for $10 < Re_D < 10^7$. It uses two relations; one for turbulence effects and one for laminar effects, which are given below:

$$Nu_{turb} = \frac{0.037 Re_D{}^{0.8} Pr}{1 + 2.443(Pr^{\frac{2}{3}} - 1)Re_l{}^{-0.1}} \qquad (12)$$

$$Nu_{lam} = 0.664\sqrt{Re_D}Pr^{1/3} \qquad (13)$$

4. Finally, the Dittus-Boelter equation [38] was used for comparison:

$$Nu_{dittus} = 0.023 Re_D^{4/5} Pr^{0.3} \qquad (14)$$

The Dittus-Boelter equation is valid for $Re_D > 10000$.

While the test conditions investigated are within the guidelines for each of these correlations, significant discrepancy was observed between them. The typical discrepancy is on the order of 12% for the relations given in Equations 8, 10 and 14. The third correlation investigated, however, was usually off by a factor of approximately 3.6. Consequently, the other three relations were used in the design.

Ultimately, it was determined that the single window design requires much higher cooling gas flow rates than what was available. This result was also confirmed by computational fluid dynamics models, which are described next. A double walled heat shield window design was determined necessary and is described later.

After completing the preliminary heat transfer calculations, it was necessary to rerun these calculations with Computational Fluid Dynamics (CFD). The preliminary calculations were run in parallel with CFD work conducted by Don Frederick (Frederick, 2010) [42] as the burner design evolved. Figure 42 shows a representative CFD result. This result was for an early design with cutouts where the pressure vessel windows exist. This design was quickly ruled out because the maximum temperature of the pressure vessel walls was well above the limitation.

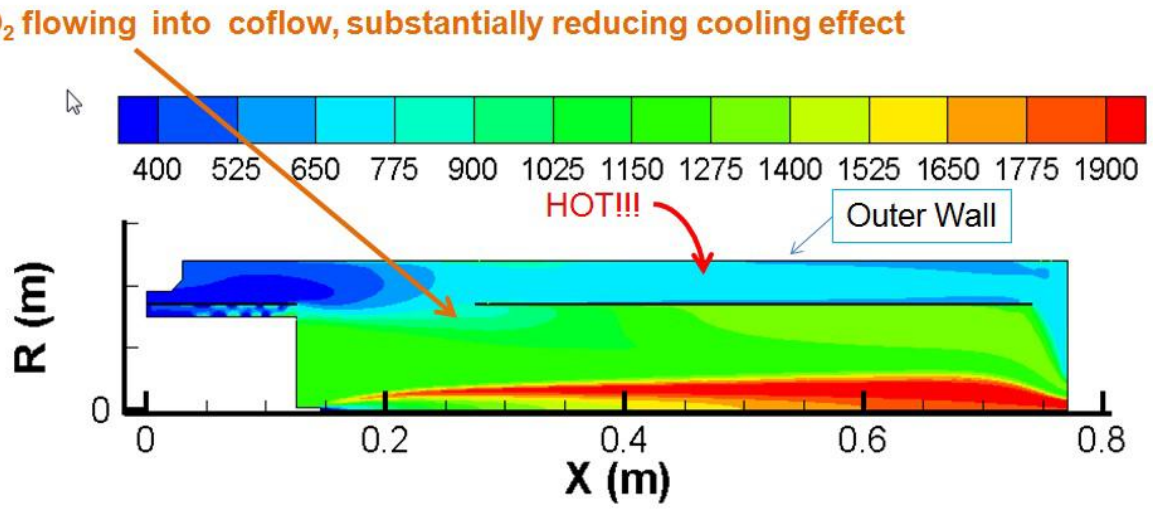

Figure 42: CFD result for CO_2 coolant flowing around heat shield with no inner windows.

Information gleaned from CFD work caused also several other early designs to be ruled out due to inadequate cooling. An example graph used in this analysis is shown in Figure 43. The design methodology involved beginning with the simplest design possible and adding complexity in an iterative fashion as needed. The following outlines the various design considerations in an itemized list.

1. No heat shield with coolant flowing around the co-flow.

2. Single walled heat shield with cutouts for the windows for viewing the combustion event.
3. Single walled heat shield with single walled windows with CO_2 coolant flowing outside of the heat shield.
4. Single walled heat shield with single walled windows with CO_2 coolant flowing outside of the heat shield and water coolant sprayed upward above the windows.
5. Single walled heat shield with "tabs" limiting the total area that must be cooled by CO_2 to reduce the total flow rate necessary.
6. Single walled heat shield with double walled windows outside the heat shield with a water cooling jacket in areas other than the windows.
7. Single walled heat shield with double walled windows that straddle the heat shield leaving less material outside of the heat shield, with a water cooling jacket in areas other than the windows. The straddled window design allowed the co-flow diameter to be slightly increased.

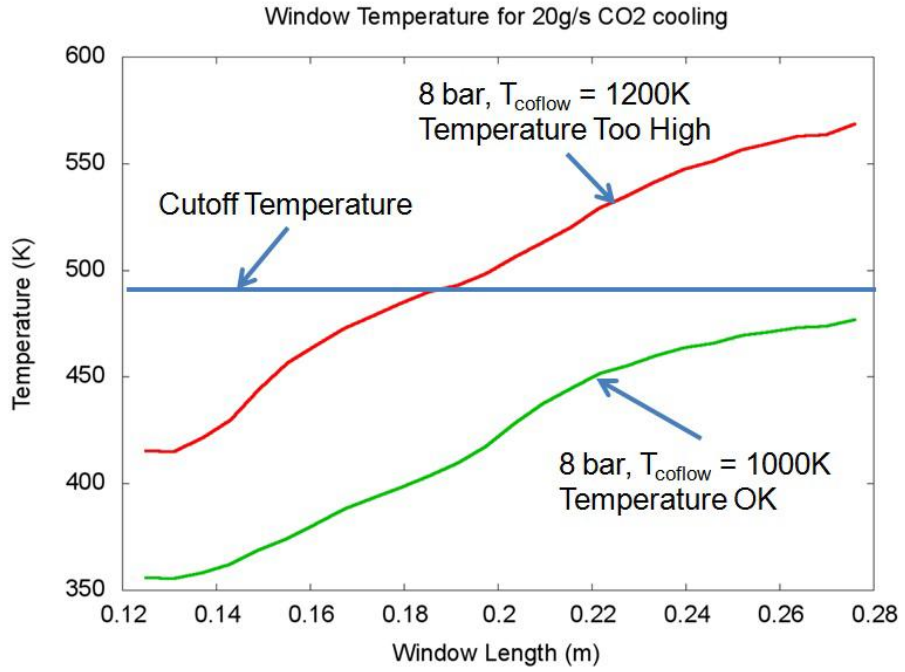

Figure 43: Summary of maximum pressure vessel wall temperatures calculated using CFD with double walled inner window cooling scheme.

Design 7 was the design analyzed in Figure 43 and is viable under the limited operating conditions. Please refer to reference [42] for a more detailed description of the various iterations in the evolution of the design. The wall temperature remains below the threshold value as long as the co-flow temperature does not exceed about 1000 K at 8 bar. The maximum cooling capacity restriction dictated the maximum heat release rate of 270 kW. As a result, the maximum allowable co-flow equivalence ratio at 8 bar was set at 0.27 which corresponds to a co-flow temperature of 1000 K.

The heat shield needs to be water cooled in order for the assumptions made in the CFD computations to remain valid. The high pressure chamber facility is equipped with provisions to provide the water coolant flow rates necessary. The maximum water pressure available was 6 bar, which affects the flow rate of cooling water that can be delivered for a given water cooling design. Any water cooling scheme utilized thusly needed to ensure the pressure drop for the required water flow rate is below 6 bar.

Final Steady State Elevated Pressure Burner Design Details

The water cooling jacket maintains the heat shield below the temperature where radiation from the heat shield would heat the pressure vessel walls beyond their temperature threshold. The double walled windows ensure that the pressure vessel windows do not receive excessive radiation from the heat shield windows. Figure 44 shows a view where the cooling jacket can be viewed more easily. The outer diameter of the cooling jacket is 12 mm and the inner diameter is 10 mm. The cooling jacket can accommodate a flow rate of 0.45 kg/s, resulting in a total pressure drop of 3.7 bar, which can be accommodated by the water supply. At this flow rate, the water is capable of removing 56% of the total maximum heat load of 270 kW. It was assumed that this cooling capacity is more than enough to absorb the heat load that the cooling jacket will encounter, but experimental validation of this assumption would of course be needed.

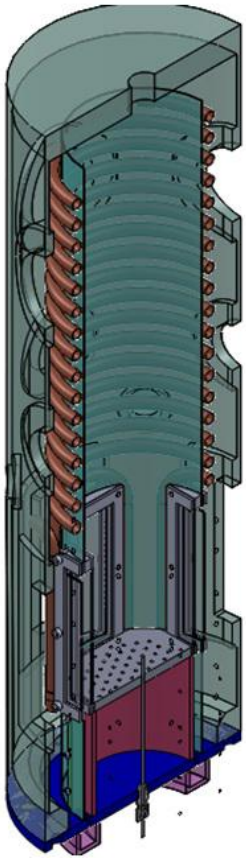

Figure 44: Section view of the steady state elevated pressure burner design situated inside the elevated pressure vessel. The total length of the pressure vessel is 810 mm.

The flow begins at the bottom of the device. The cooling jacket traverses the space between windows twice per gap between windows to ensure that radiation heat transfer from this area does not occur excessively between the heat shield and the outer wall in this region. The area below the cooling jacket is not heated by combustion so it does not need to be cooled.

Figure 45 shows two close up views of the double walled window cooling design. The walls are 45 mm wide, 267 mm long, and the space between windows is 12.3 mm in thickness. This thickness establishes a workable balance between generating high convection coefficients, and keeping the outlet temperature of the coolant below untenable levels. The thickness choice was part of the optimization process.

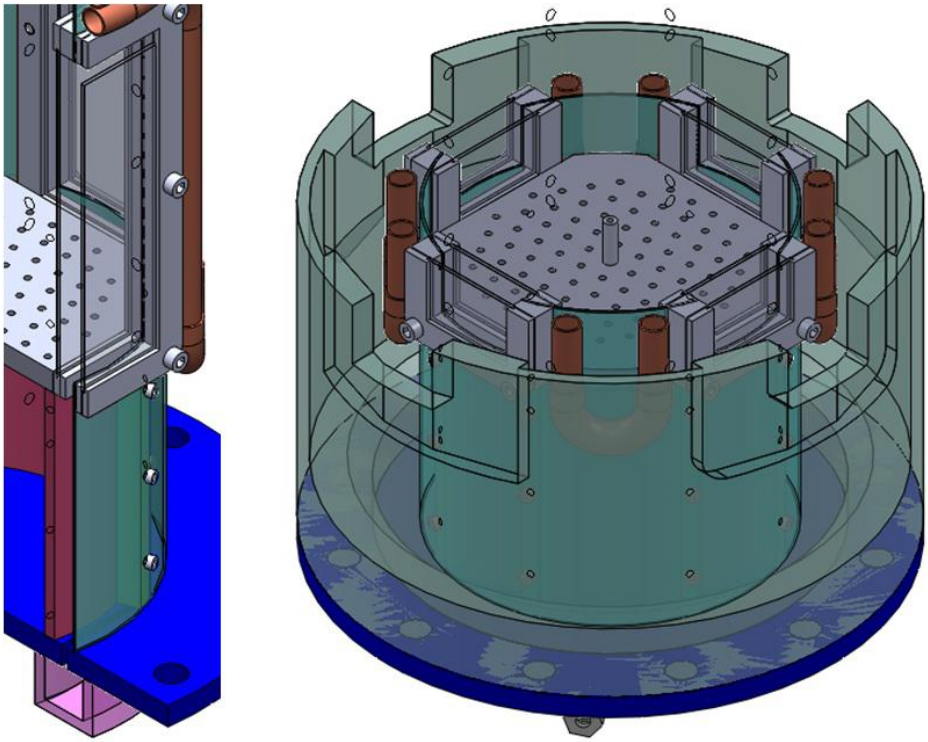

Figure 45: Close up of the double walled window gaseous cooling scheme.

Figure 46 shows a section view of the overall design with all key components labeled, and Figure 47 shows a profile view without the pressure vessel.

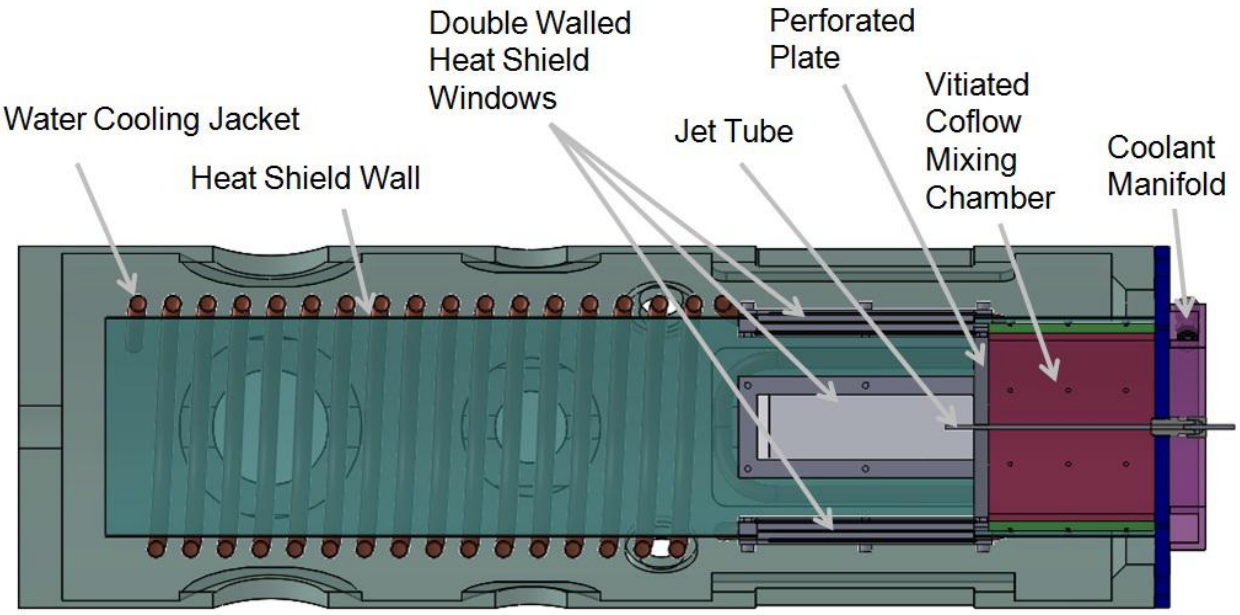

Figure 46: Steady state elevated pressure VCB with key components labeled.

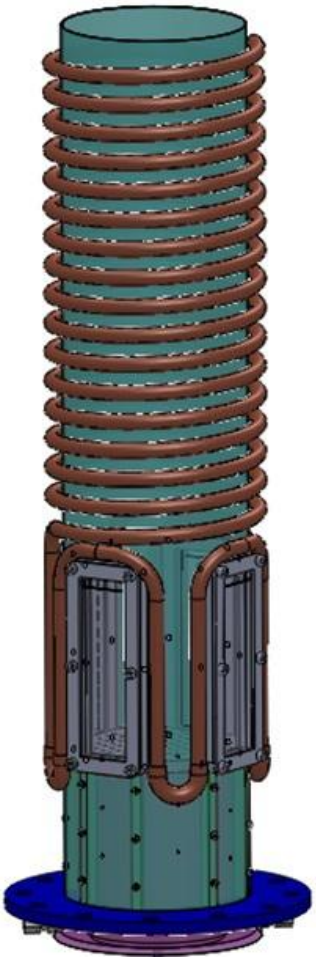

Figure 47: View of the water cooling jacket used to cool the heat shield for the steady state elevated pressure VCB.

Once the physical design was completed, it was necessary to determine how the existing flow control architecture could deliver the gases at the desired flow rates with minimal changes to existing piping and control software. Figure 48 shows the redrafted Process Instrumentation Diagram (PID) for the vitiated co-flow burner for elevated pressure conditions. The flow control architecture outlined in Figure 48 is capable of delivering all fluids under all required and allowable operating conditions.

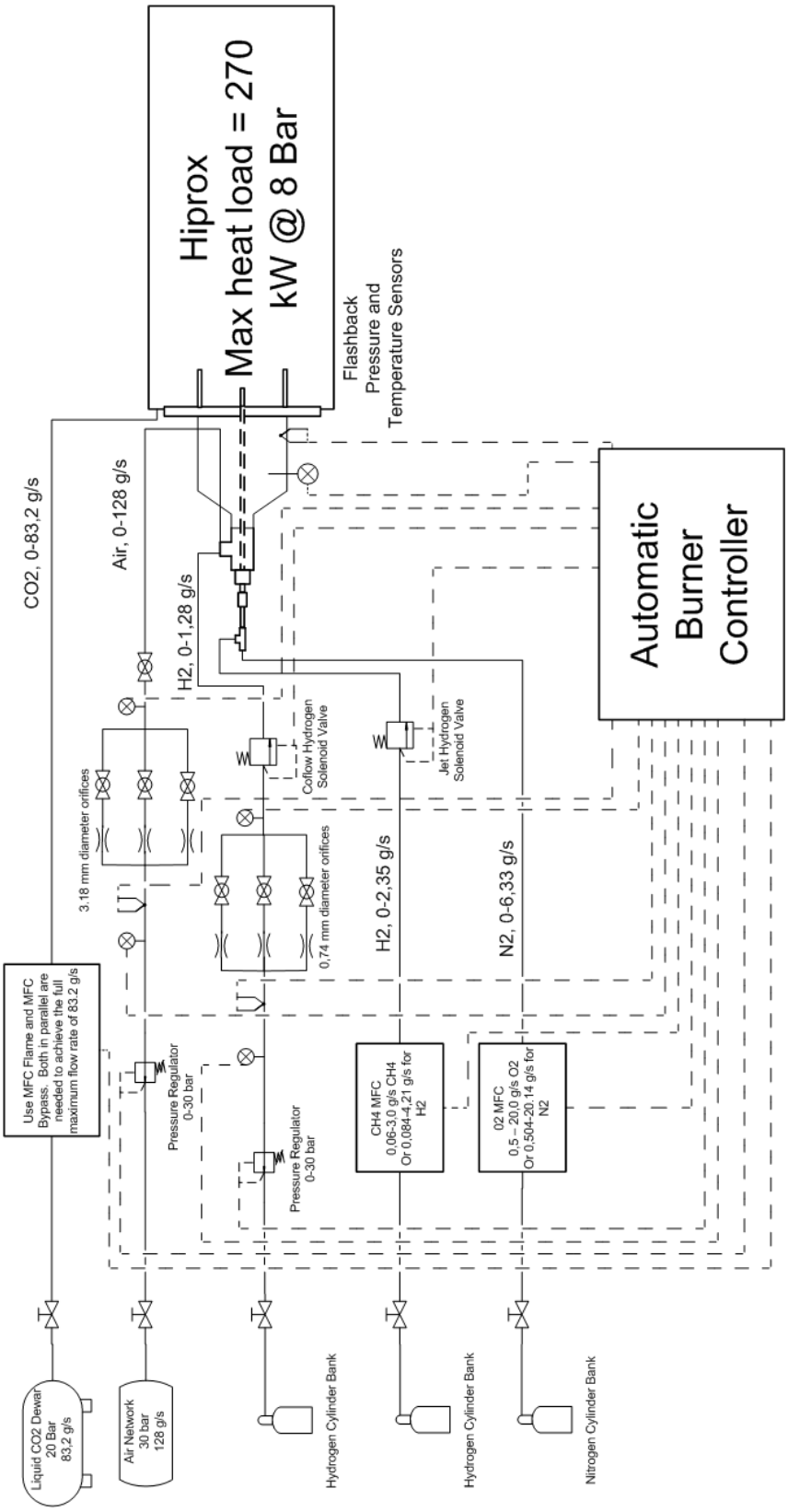

Figure 48: Process Instrumentation Diagram for the steady state elevated pressure VCB operation.

The flow delivery system design keeps the CO_2 delivery system that was used in the original purpose of the device as-is, and using sonic flow control orifices for the air supply. The maximum air delivery pressure available was 30 bar, allowing a high dynamic range to be achieved in the air flow rates delivered, which was necessary for operation from 1 to 8 bar with a single set of sonic flow control orifices.

The steady state elevated pressure burner design is capable of operating at 8 bar with a maximum co-flow equivalence ratio of 0.27 with a hydrogen jet velocity of 400 m/s for an inner jet diameter of 0.093". At 8 bar, the co-flow would utilize all of the available air supply of 128 g/s, creating a co-flow bulk velocity of 0.9 m/s (before combustion).

Alternative "Line of Sight" Steady State Elevated Pressure Burner Designed

It was realized that the steady state elevated pressure VCB may never have employed laser diagnostics, which was the reasoning for implementing 2 pairs of windows. It was therefore decided to prepare an alternative design where only 1 set of windows is used, which is all that would be needed for either schlieren imaging or direct imaging function. The removal of 1 set of windows would represent significant savings with regard to cost, time and design complexity, and it would also increase the total amount of gaseous coolant available for the remaining 2 windows. The operational limits of the device would consequently broaden as well with only 1 pair of windows. The alternative design is shown in Figure 49.

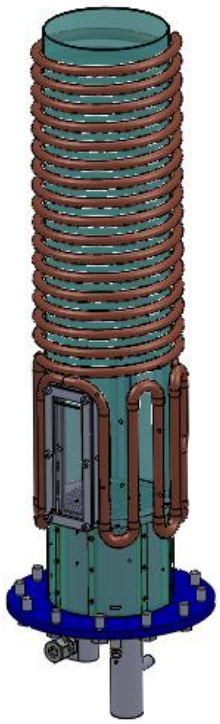

Figure 49: Line of sight steady state elevated pressure VCB design.

The water cooling jacket and the CO_2 inlet manifold also needed to be redesigned in simplifying the means by which CO_2 is delivered to the cooling channels. The alternative CO_2 inlet manifold

design involved two extensions from the inlet mounting plate that simply allows adapter fittings for the inlet tubes to connect to.

iv. *Diagnostics*

a) High Speed Schlieren Imaging

Atmospheric Pressure

The primary diagnostic used for atmospheric pressure research is schlieren imaging. This system has already been briefly described in section 2.a), but will be described here in more detail as it applies to the atmospheric pressure burner. Figure 50 shows the full schlieren imaging system with each component labeled. Figure 51 shows an enlarged photograph of the schlieren imaging system with the burner. The spherical mirrors are 6" in diameter, allowing a broad range of liftoff heights to be studied without adjusting the position of the burner. The maximum camera shutter speed which did not overly diminish image brightness was 25 µsec with this system, which allowed crisp images to be obtained even with high levels of turbulence. Additionally, the camera used is capable of obtaining high speed video at 1200 Hz, allowing various turbulence characterizations to be made. These characteristics are valuable in assisting in developing of subgrid-scale turbulent combustion closure models, if desired.

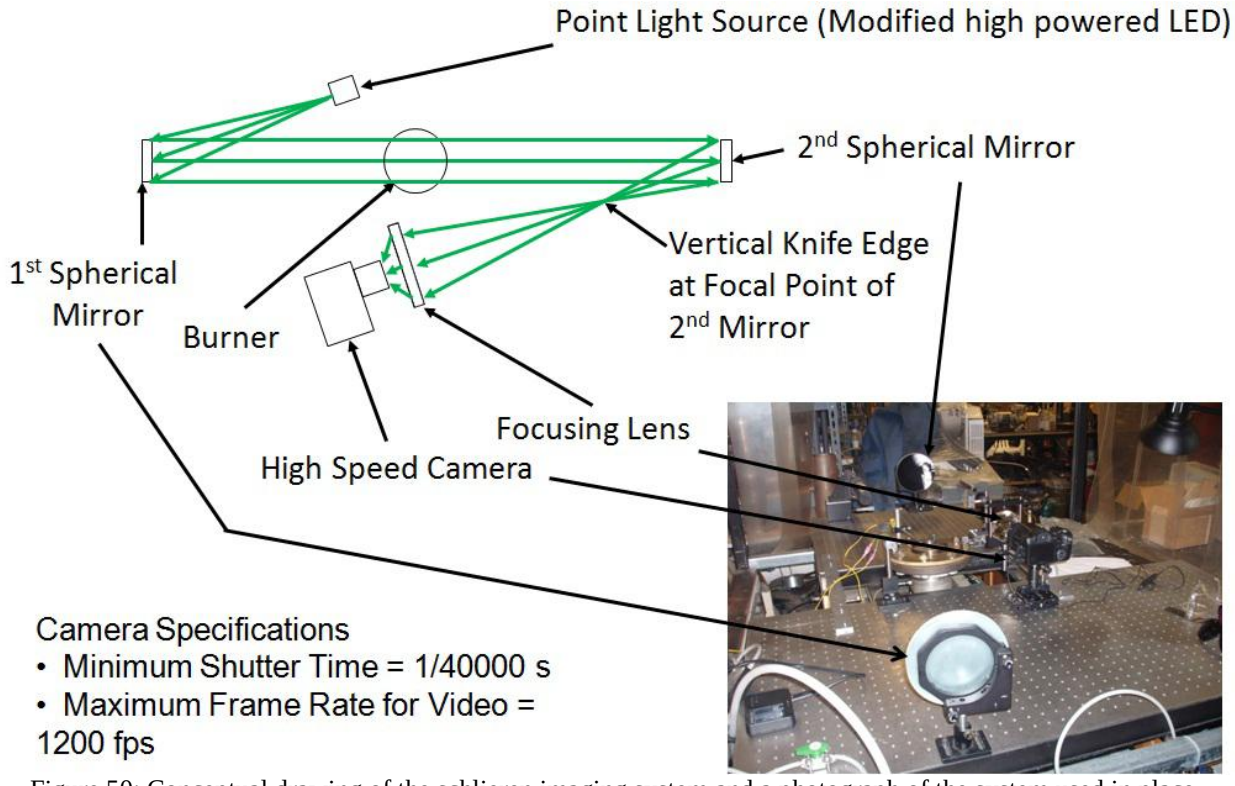

Figure 50: Conceptual drawing of the schlieren imaging system and a photograph of the system used in place.

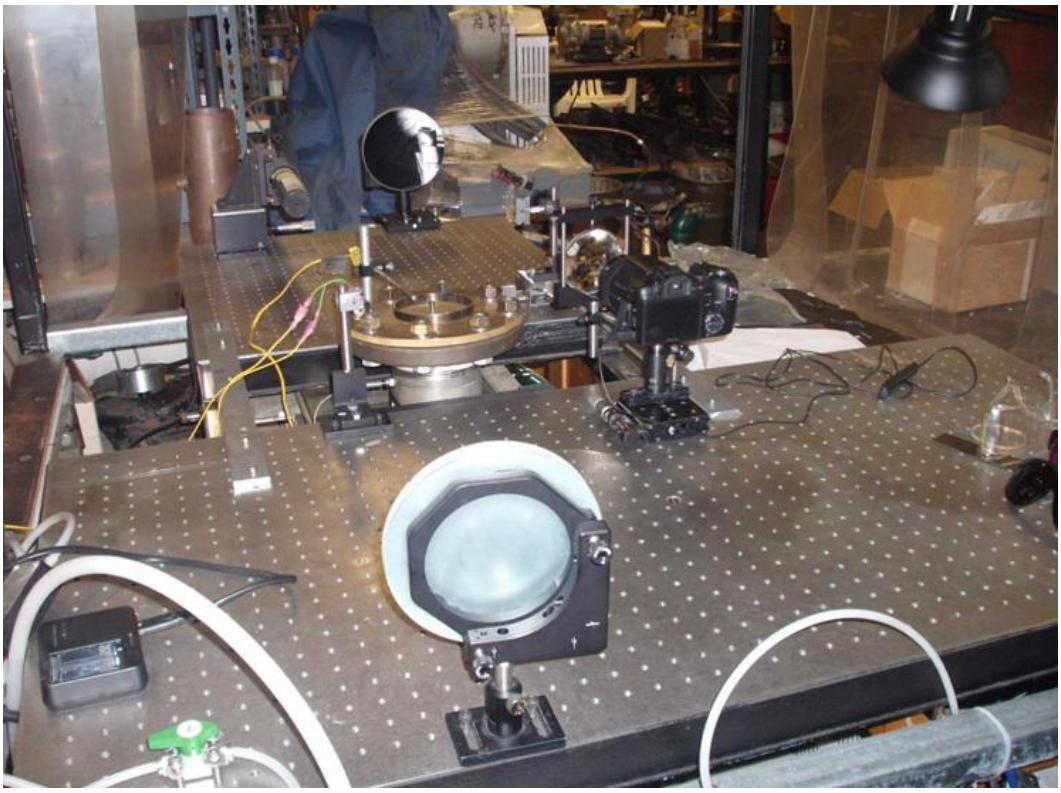

Figure 51: Atmospheric pressure burner with schlieren imaging system. The mirror diameter is 6 inches.

The light from a high powered LED serves as a point light source which is collimated by a spherical mirror. The collimated light passes over the burner and is then focused by a second spherical mirror. A knife edge is placed at the focal point of the second spherical mirror which blocks approximately half of the light. The remaining light is then relayed into the lens of the high speed camera, and the camera used is depicted in Figure 52. The schlieren effect is produced when refracted light resulting from density gradients causes light that would have reached the camera to instead be blocked by the knife edge. This refracted light is manifested as dark areas in the image. The camera is capable of taking still frames with a shutter speed of 25 μs and high speed video up to 1200 frames per second (0.8 ms per frame). Figure 53 illustrates the physics involved when density gradients refract the collimated light and Figure 54 shows a representative schlieren image where the method by which the liftoff height was measured is shown.

Figure 52: High speed camera used for the atmospheric pressure research.

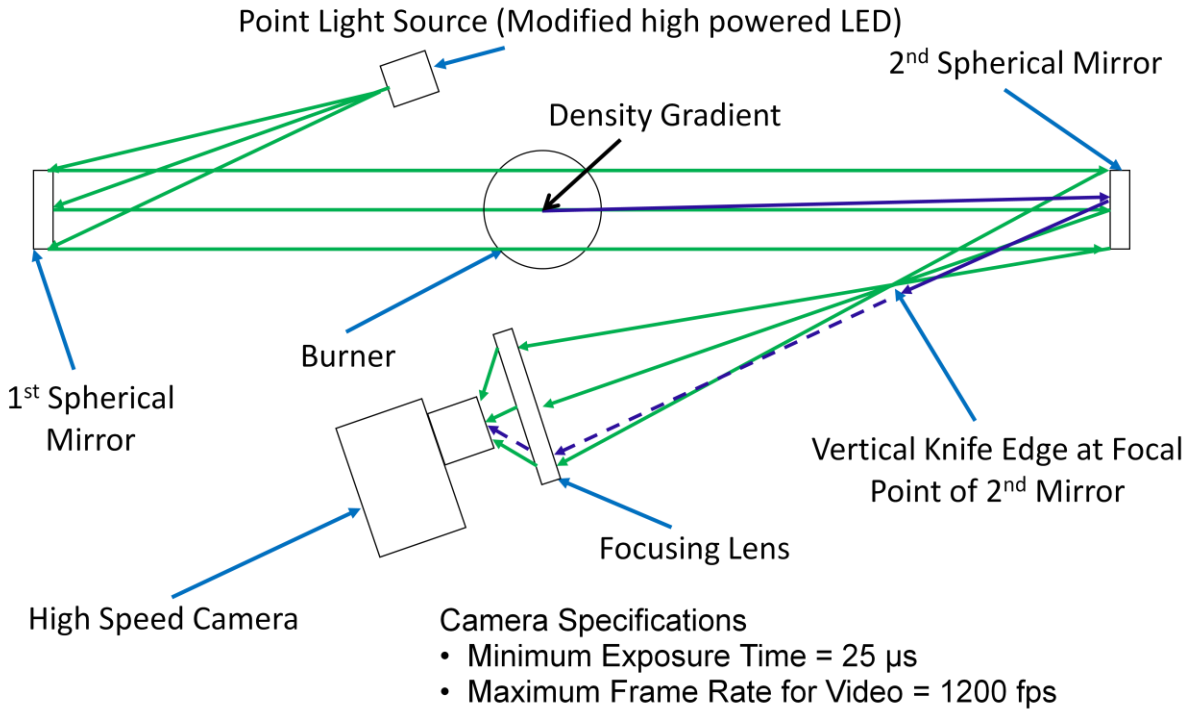

Figure 53: Schlieren diagram with refracted light ray illustrated.

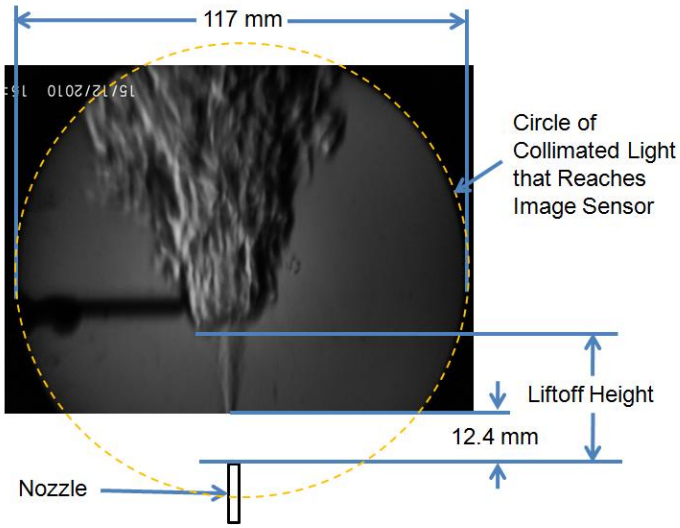

Figure 54: Representative schlieren image of a lifted N_2-in-H_2 jet flame with the method by which liftoff height was measured is illustrated. The exposure time is 156 µs.

The distance between the bottom of the image and the liftoff position is measured and then scaled to physical space. The result is added to the known distance between the bottom of the image and the top of the jet to give the actual liftoff height. The average liftoff height measured from five images was used for all atmospheric pressure liftoff heights reported.

Figure 55 shows a representative set of images obtained with the schlieren imaging system shown in Figure 53. The difference in liftoff height is clearly visible between the two images. Here, the liftoff height is defined as the position where the first density gradient is visible, regardless of distance from the center axis. Direct imaging of the flame is not capable of generating results this clear with lifted hydrogen jet flames. Additionally, it is possible to obtain statistics describing the variation of liftoff height with time with the schlieren imaging system.

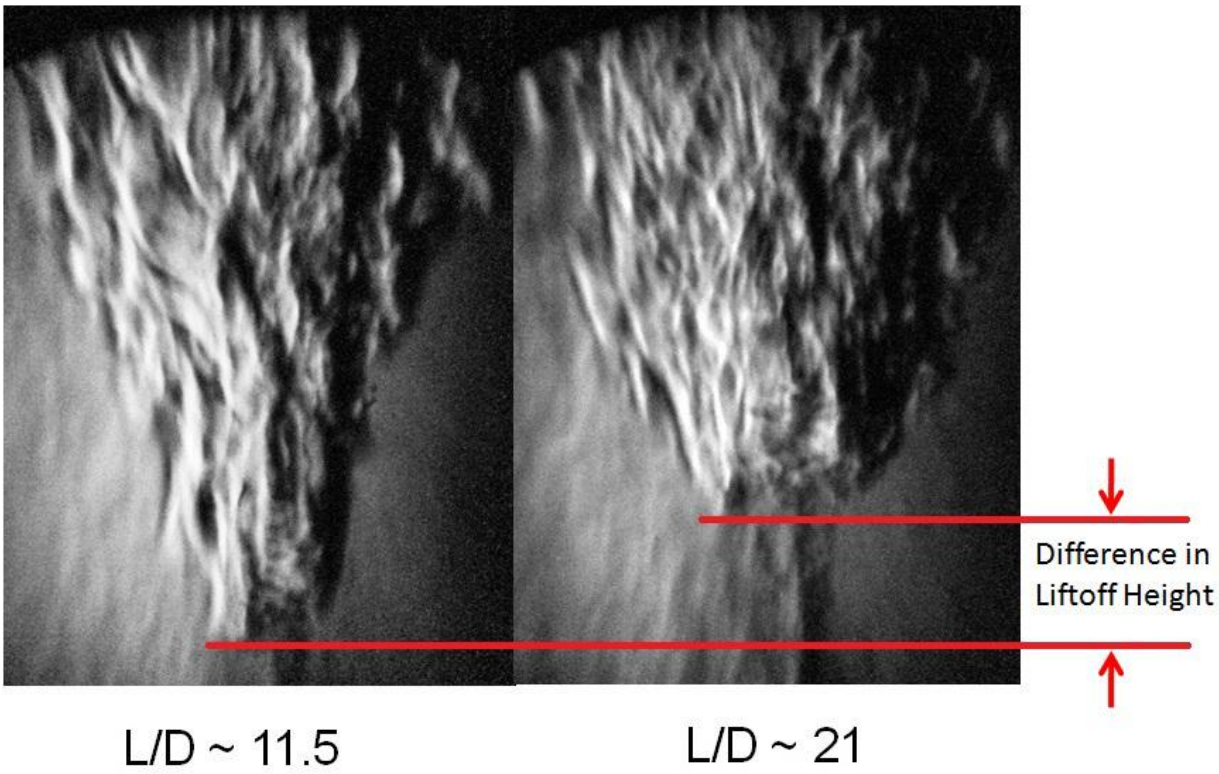

Figure 55: Comparison of liftoff heights clearly made visible with schlieren imaging system.

As previously mentioned, direct imaging produces images that are too time-averaged for the quality of statistical information to be gathered that can be gathered with schlieren imaging. This finding is shown in Figure 56. Hydrogen jet flames are not luminous enough to allow production of images using direct imaging at high enough frame rates that eliminate the time averaging effect. Therefore, schlieren imaging allows the introduction of "artificial" light, which facilitates effective use of higher frame rates than the frame rates that can be used effectively with direct imaging.

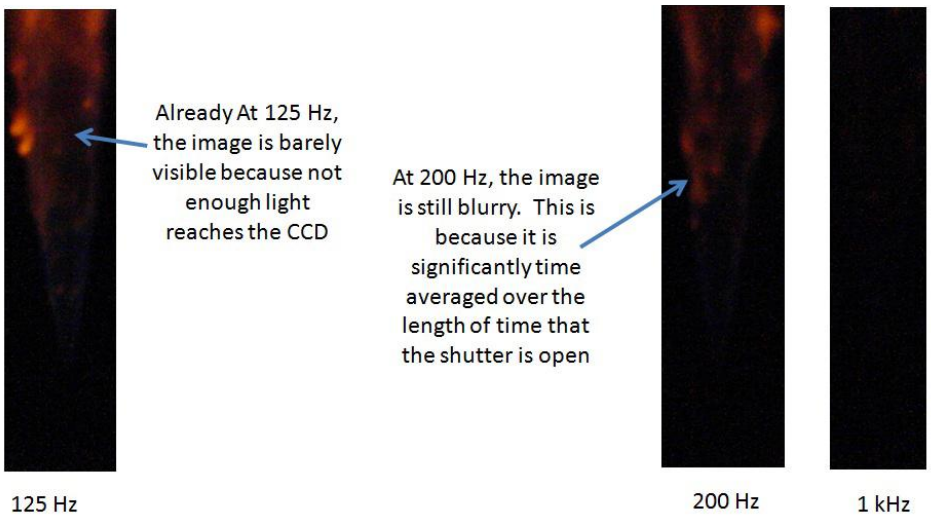

Figure 56: Photographs taken at various frame rates using direct imaging. All photographs show a time averaged depiction of the flame, but image brightness is rapidly diminishing.

It is possible to approximately determine the sensitivity of the schlieren imaging system, as shown in Equation 15 [43].

$$\frac{dn}{dx}_{min} = 0.5 \frac{n0}{L} \frac{a_0}{f_2} \qquad (15)$$

where dn/dx_{min} is the minimum refractive index gradient that would be visible, n_o is the refractive index of the unburned gases or the surrounding gases, L is the depth over which the density gradient being visualized persists, a_o is the unobstructed height of the light source, and f_2 is the focal length of the second spherical mirror. The 0.05 prefactor is called the "contrast threshold" and is assumed in this equation. The prefactor is based on other physical parameters that can be more difficult to estimate. A cursory calculation of the prefactor for this setup yields a value of 0.0152, meaning that the existing schlieren imaging system likely has better sensitivity than that implied by this formula by a significant margin.

The minimum refractive index gradient can be further translated into the minimum density gradient measurable. Equation 15 [43] shows this relation.

$$n - 1 = k\rho \qquad (16)$$

In order to use Equation 15, one must first assume a distance over which the gradient persists and is uniform. In this way, the gradient is discretized, and a density difference can be calculated where the distance over which this gradient persists is the discretization distance. Analyses using these equations can be very elucidating in characterizing the data gathered from schlieren imaging of turbulent jet flames.

It is instructive to compare direct imagining to schlieren imaging in assessing how the information from these diagnostics compare. Figure 57 shows an overly of a direct image taken with a long shutter time onto a schlieren image of the same flame.

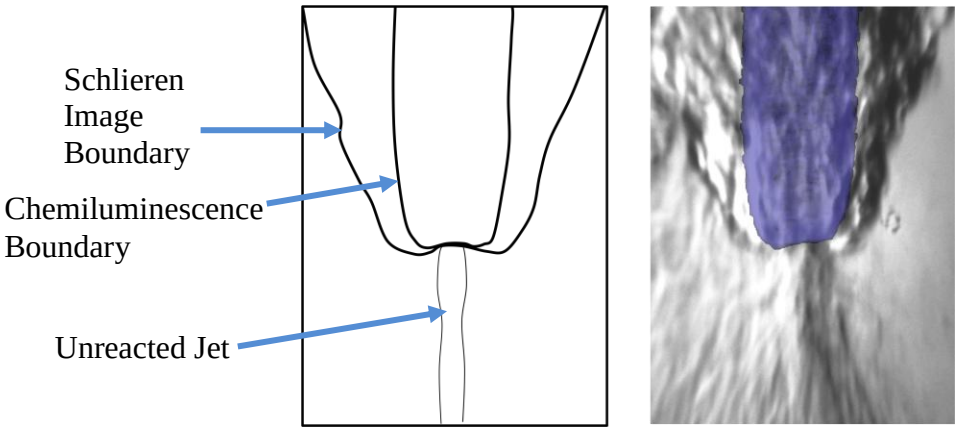

Figure 57: Overlay of a schlieren image of a lifted flame with a direct image (chemiluminescence) with an accompanying conceptual drawing of the image. The schlieren image was taken with a 500 μs exposure time. The direct image was taken with a 50 ms exposure time.

The direct image (chemiluminescence) is a time averaged result over the 50 ms exposure, while the schlieren image is an instantaneous representation of the flame. Figure 57 shows that density gradients persist further radially from the center axis than chemiluminescence at the point of ignition, indicating that either hot products are recirculating in this region, or radial conduction causes these density gradients.

Elevated Pressure Instrumentation

Schlieren imaging was initially the diagnostic planned for use with the elevated pressure experiments, in keeping data consistent with atmospheric pressure results. At low pressure, the apparatus behaves favorably, with clearly measureable liftoff heights. Figure 58 shows flame progression from an attached flame to a lifted flame to a flame where the liftoff height has further increased. These flames are in order of increasing nitrogen dilution for a co-flow equivalence ratio of 0.15, and chamber pressures below 1.5 bar.

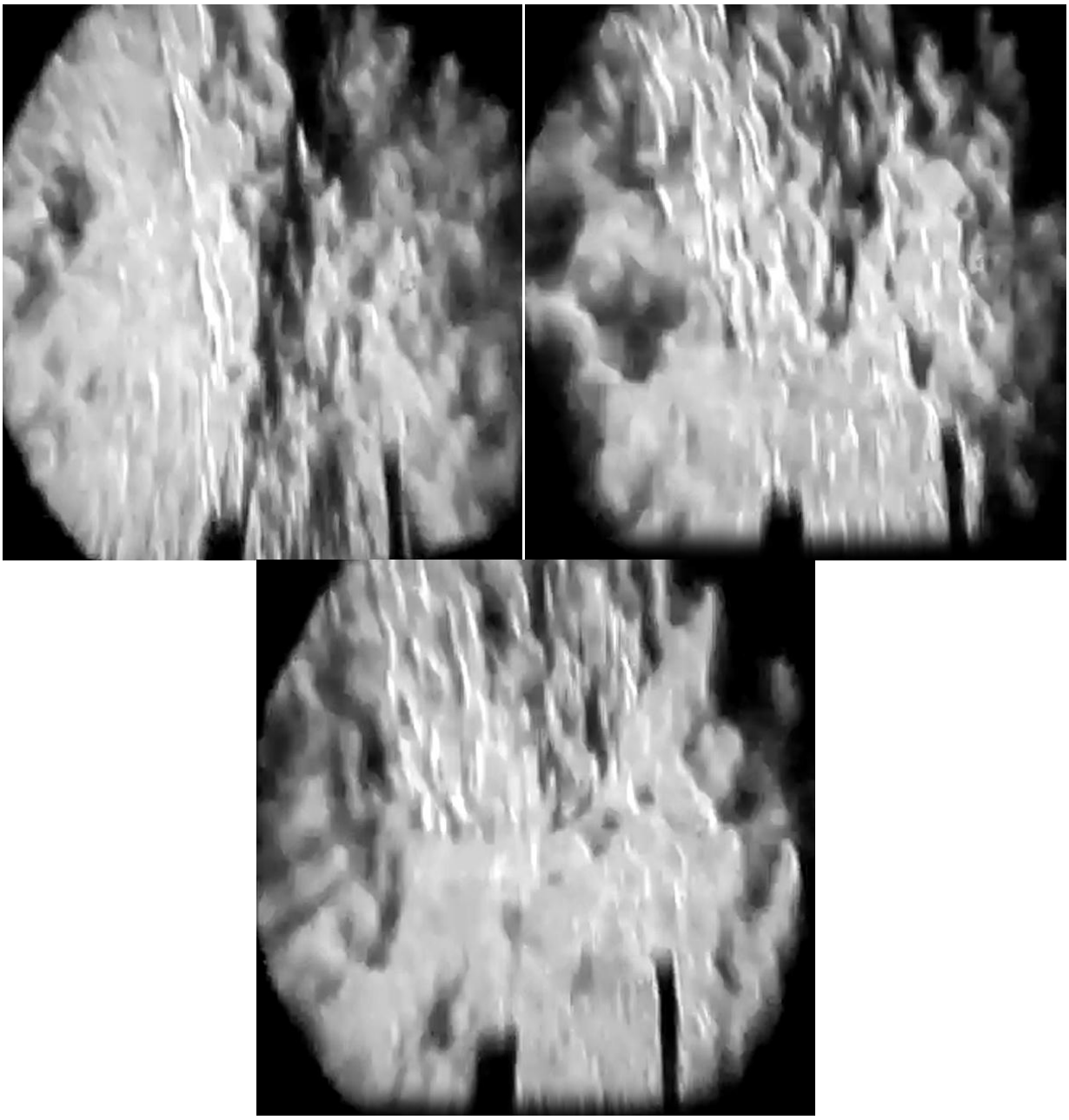

Figure 58: Schlieren images of (top left): attached flame; (top right): slightly lifted flame; (bottom) further lifted flame.

The liftoff height is clearly measureable in these images and each frame is relatively crisp. In contrast, at higher pressures, condensation tends to build up on the windows. This condensation causes the images to darken which complicates the task of measuring liftoff heights. Figure 59 shows this effect.

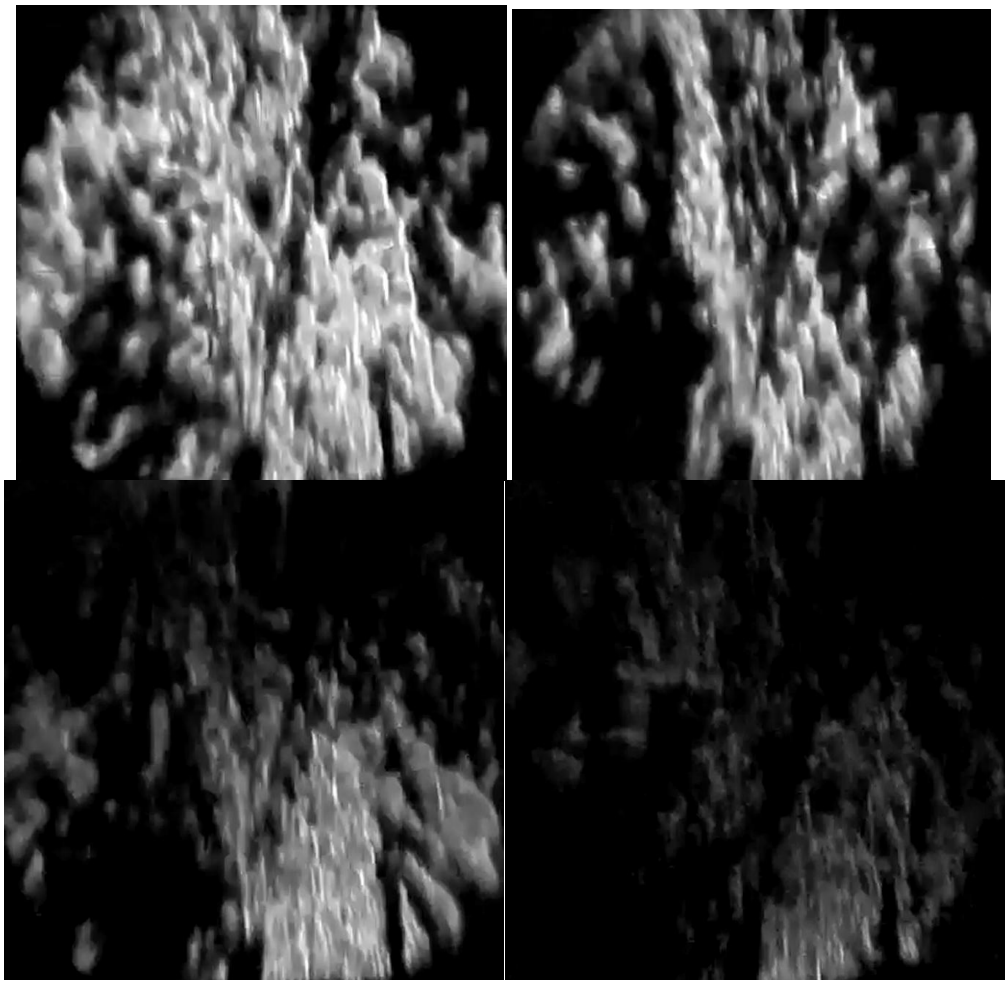

Figure 59: Images of an attached flame at a pressure of 1.8 bar. Images are in chronological order through a single test showing the effect of condensation buildup on the windows.

Several methods of combating the condensation problem were investigated. The first method attempted was to place a glass cylinder around the burner, which would heat up while not holding pressure. This cylinder would also serve as a heat shield for the outer windows. Theoretically, the cylinder should become hot enough during an experiment in preventing condensation accumulation. The glass cylinder investigated is shown in Figure 60.

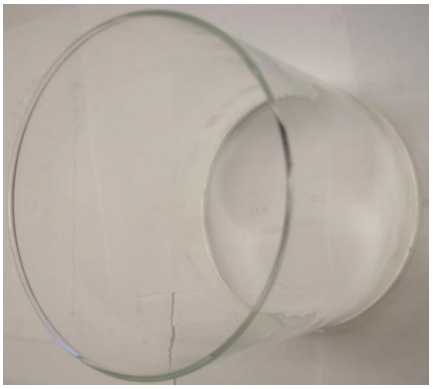

Figure 60: Glass cylinder positioned around the burner for investigating condensation buildup prevention on the outer windows.

It was quickly determined that the cylinder causes the schlieren collimated light 'circle' to be deflected considerably with very little light reaching the image plane. This method was consequently ruled out as a window condensation accumulation prevention technique.

The next method investigated was to run shorter jet durations in reducing the time available for condensation accumulation on the windows. Unfortunately, the greatest pressure gradient exists early in the jet firing sequence, so when the liftoff height measurements include these gradient effects, the average values of liftoff height become less representative of a true steady state average liftoff height. This method was necessary but insufficient for solving issues encountered later for measuring liftoff heights because the reduction in jet duration ultimately invoked was helpful, but not more modifications were needed in accommodating the quasi steady-state requirement as well as the window condensation buildup issue.

The final method investigated for troubleshooting the window fogging problem was to apply an anti-fog coating to the pressure vessel windows. Several anti-fog coatings were investigated, and the chemical with the best performance investigated was from Hydromer, Inc. Figure 61 shows an image from the Hydromer website which demonstrates laboratory performance of the coating.

Figure 61: Example of the anti-fog performance of the coating from Hydromer, Inc. Image source: hydromer.com

Without the coating, condensation on the windows caused the images to darken making it very difficult to measure liftoff heights, as shown in Figure 59.

Figure 62 shows schlieren images taken from a comparable case presented in Figure 59, but after the Hydromer anti-fog coating was applied at a pressure of 1.85 bar.

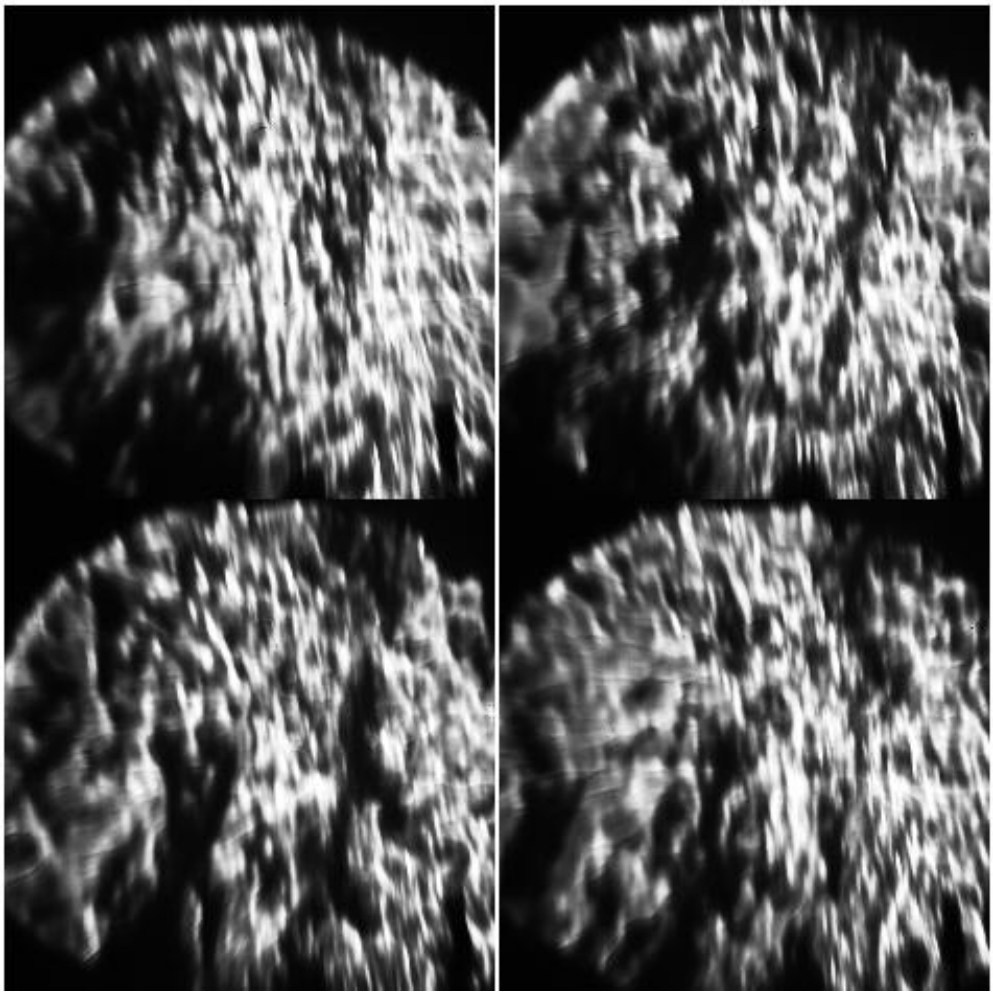

Figure 62: Schlieren images of a flame at a pressure of 1.85 bar taken with the anti-fog coating. Images are in chronological order through a single test showing that condensation buildup is negligible with the anti-fog coating.

No discernible amount of image obscuring from fog was observed after the coating was applied.

b) High Speed Direct imaging

Unfortunately, even with favorable performance of the anti-fog coating, the schlieren imaging method proved troublesome. The quiescent regions between the burner and the windows provide a semi-stagnant atmosphere where hot water vapor tends to recirculate. Density gradients from the heterogeneous mixture of hot water vapor and air tend to dominate the schlieren imaging effect which renders data gathered from this method relatively useless. For this reason, direct imaging was opted as the next most reliable alternative. A high speed camera with a significantly improved light sensor was obtained to allow direct imaging even at high speed to be used with acceptable image resolution. The camera selected is the Photron Fastcam 1024, which has a PC integrated PCI control board, which allows video to be taken at frame rates of up to 100,000 fps at reduced resolution and up to 2000 fps at full resolution. These features represent a significant performance improvement over the original camera used could which could only take video at 300 fps at full resolution and 1200 fps at reduced resolution. Figure 63 shows this camera and the PCI board.

Figure 63: Photron FASTCAM 1024 with PC integrated PCI control board. Image source: photron.com

In configuring the system to make full use of the upgraded camera, an LED (triggered by LABVIEW) which illuminates when camera recording is desired was installed in the camera's field of view. The camera's software was configured to search for a bright spot where the LED is located and to begin recording when a user-specified region specific average threshold pixel value is exceeded. This functionality allows high speed videos of the phenomenon of interest to be taken without saturating the on-board memory limitations. Additionally, a mirror was added at a 45 degree angle in front of the camera with respect to the line of sight of the burner for protection of the camera in the event of chamber over-pressurization. Figure 64 shows a representative direct image from high speed video taken at 6000 fps.

Figure 64: Direct image of a hydrogen lifted flame in the transient elevated pressure apparatus taken from video at 6000 fps.

The lifted flame is clearly visible with this camera at an acceptable frame rate for liftoff height measurements with H_2 jet flames. Additionally, direct imaging allows higher co-flow

temperatures to be investigated because with schlieren imaging, gradients between jet products and co-flow products reduce as the co-flow temperature increases. Consequently, measurement of the liftoff height from schlieren imaging would have always been limited to relatively low co-flow temperature (around 900 K).

Direct imaging also facilitates automatic processing of video data because the liftoff height is typically (and with this research) defined in direct imaging as the location where luminance surpasses a threshold value, whereas with schlieren imaging, determination of the liftoff height is more complicated because detail unrelated to liftoff height is also visualized, so individual investigations of each image are needed. A MATLAB script was written which measures all of the liftoff heights automatically using 100 data points separated evenly over the period of 0.5 seconds (at the end of the 2.2 second jet duration). The resulting measurements involve less bias than those measured from schlieren imaging because the time for each liftoff height measurement is consistent between each case due to the automated nature of the new measurement method.

The post-processing program scans the selected video still-frames starting at the bottom of the image and moves upward until the mean value of the monochromatic signal for the central 42 pixels exceeds a threshold of 60 (a value of 256 represents pixel saturation and a value of 1 represents an absence of light). The 500 ms of video is broken into 50 equally separated frames (in time), and the mean value of L determined from this set of frames is taken as L.

c) Microphone for Unsteady Regime Ignition Frequency Characterization

The recording system used for analyzing the unsteady stability regime consists of a cardio condenser microphone which is a microphone with a heart shaped sensitivity pattern. It is designed for computer-based recordings with a USB digital output. This microphone was chosen because it has an 'at frequency' response meaning that the microphone is equally sensitive to all frequencies. The microphone was connected to a computer applying the software All2WAV Recorder to record the signal and store the signal as a wave file. The wave file was processed numerically with MATLAB. The microphone position is shown in Figure 65:

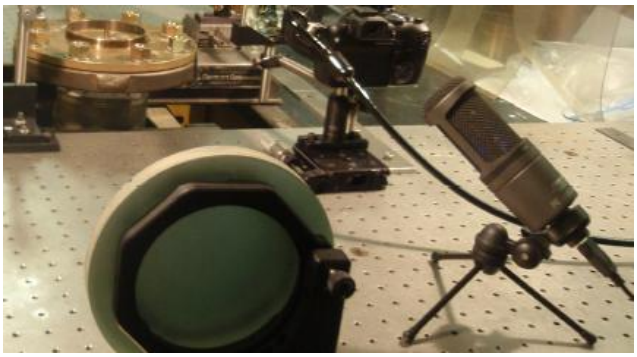

Figure 65: Atmospheric burner with microphone in place along with schlieren imaging system.

High speed schlieren imaging was also used to validate the results obtained from the microphone. High speed videos with playback time spans of 18 seconds were used with frequencies of 600 frames per second for all flames. The videos were studied and the number of

times the flame would appear to have blown out and re-ignited was reported and divided by the time. Playback of the videos was conducted at speeds 20 to 60 times slower than real time.

d) Supporting Diagnostics

With regard to instrumentation which supports the primary diagnostics employed, the following sensors were used:

1. Pressure transducers were plumbed to the insides of the pressure vessel(s) for chamber pressure control and overpressure protection. Pressure transducers were also placed in the mixing chamber of the transient elevated pressure apparatus, as well as upstream and downstream of the sonic flow control orifices
2. A thermocouple was placed in the mixing section which is used as a technique for stopping reactant flows in the event of flashback. The pressure transducer in the mixing section also served as a redundant safety feature for the same purpose.
3. Pressure sight gages were also employed for redundant checks on all pressure transducer readings.

Temperature Instrumentation with the Transient Elevated Pressure VCB

Two methods of measuring the temperature of the co-flow were employed with the transient elevated pressure VCB because this temperature is arguably the most influential factor on the combustion characteristics for the device. The first temperature measurement is an exposed junction K-type thermocouple positioned directly in the co-flow. The position is adjustable is adjusted in practice until the maximum temperature under static conditions is measured. This method facilitated acquisition of measurements closest to the actual temperature of the products without possible interference from unreacted species or outside air entrainment.

The second measurement technique involves direct calculation based on reactant flow rates, and thus the equivalence ratio of the co-flow. Cabra et al (2005) [11] developed a correlation between co-flow temperatures measured also using a thermocouple in addition to measurements from laser thermometry and known reactant equivalence ratios for lean premixed hydrogen combustion. Using this data, and incorporating a radiation heat transfer correction factor to improve the accuracy of the measurements gathered with the thermocouple, Cabra et al were able to develop a simple correlation relating co-flow temperature to co-flow equivalence ratio shown in Equation 16. This relationship is also depicted graphically in Figure 66. The curve above the data and curve fit in Figure 66 is based on a numerical model which uses the adiabatic assumption.

$$T(K) = 2462\ \phi_{co\text{-}flow}^{0.69} \qquad (16)$$

The data acquisition system outputs both the radiation corrected temperature measured with the thermocouple and the one predicted based on the co-flow equivalence ratio. Under most conditions, these two measured temperatures agree favorably. Instances when the temperature measurements likely stem from the fact that the radiation correction factor is assumed constant for simplicity, but is in actuality a function of temperature.

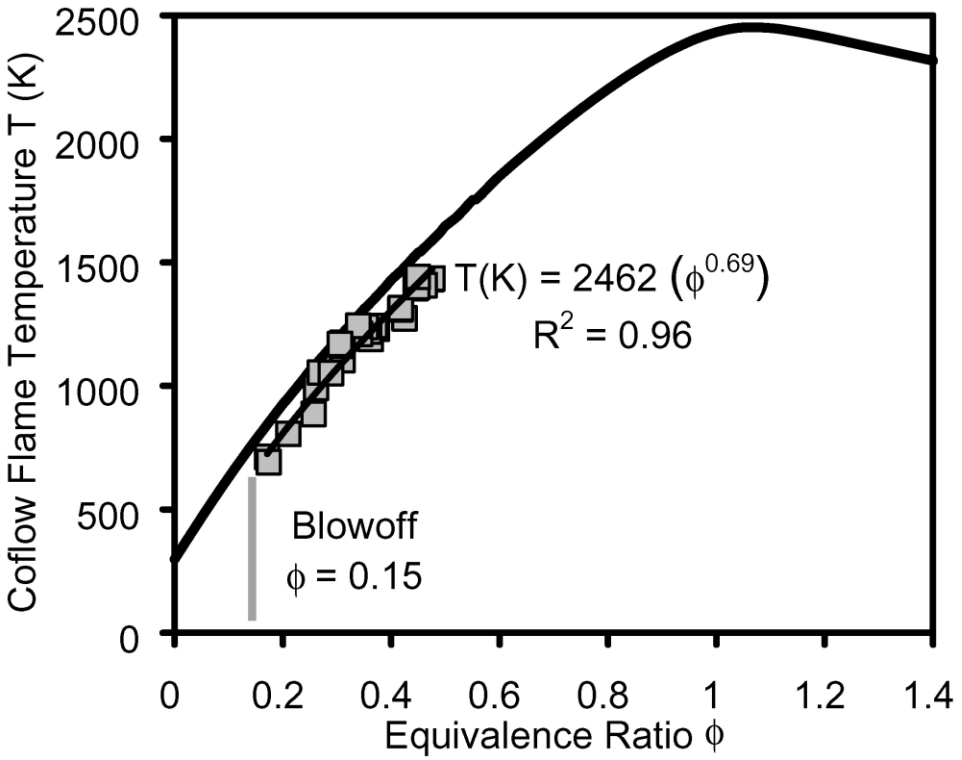

Figure 66: Measured relationship between temperature and equivalence ratio for premixed hydrogen combustion. A curve fit to the data is plotted alongside.

4. Results and Discussion

i. *Preliminary Foundational Work*

Initial research conducted with the goal of understanding how autoignition dominated processes compete with flame propagation is described in this section. This research can be summarized as an attempt at decoupling the flame propagation stabilization mechanism from the autoignition flame propagation mechanism. Ethanol (EtOH) and Dimethyl Ether (DME) serve as ideal fuels for this purpose because both are chemical isomers of C_2H_6O and consequently have similar properties except for their autoignition delay times. The DME and EtOH molecules are depicted conceptually in Figure 67. DME is more prone to autoignite than EtOH. Consequently, through careful comparison of premixed combustion characteristics between the two fuels, it could become possible to identify features caused by autoignition as those that exist within DME flames and are absent within EtOH flames under comparable conditions. Table 1 compares combustion characteristics between DME and EtOH.

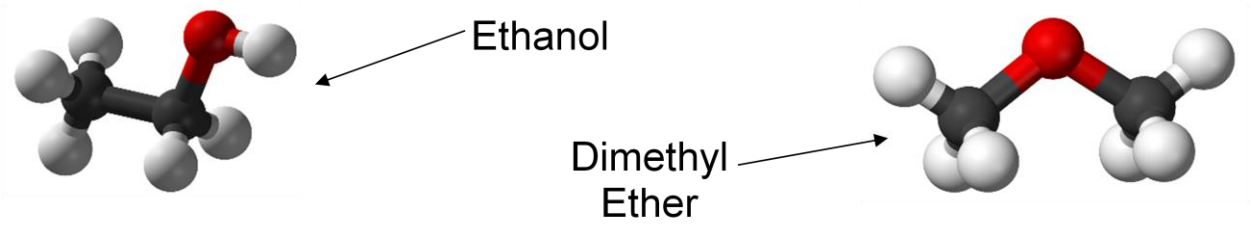

Figure 67: Pictorial comparison between DME and EtOH.

Table 1: Comparison of combustion properties between DME and EtOH.

	DME	**EtOH**	**References**
Autoignition Temperature (C)	350	423	Varish, [44]; Borman, [45]
Molecular Mass (g/mol)	46	46	
Higher Heating Value (kJ/kg)	28000	29700	Varish, [44]; Borman, [45]

The dramatic difference between the autoignition temperatures of EtOH and DME is apparent. Of course, onset of autoignition is influenced by factors other than temperature, namely pressure and equivalence ratio.

a) Numerical Autoignition Investigations

Detailed reaction mechanisms developed by Lawrence Livermore National Laboratories (LLNL) were used in carrying out a computational comparison between the combustion characteristics of DME (Fisher, [46]; Curran, [47]; Kaiser, [48]) and EtOH (Marinov, [49]). The number of elementary reactions included in the reaction mechanisms for EtOH and DME are 383 and 660 respectively. These mechanisms were used together with the equilibrium chemical kinetic solver Cantera [50] in the development of the computational results. Figure 68 compares the computed ignition delay times for DME and EtOH as functions of temperature at equivalence ratios of 0.6, 0.8, and 1.0.

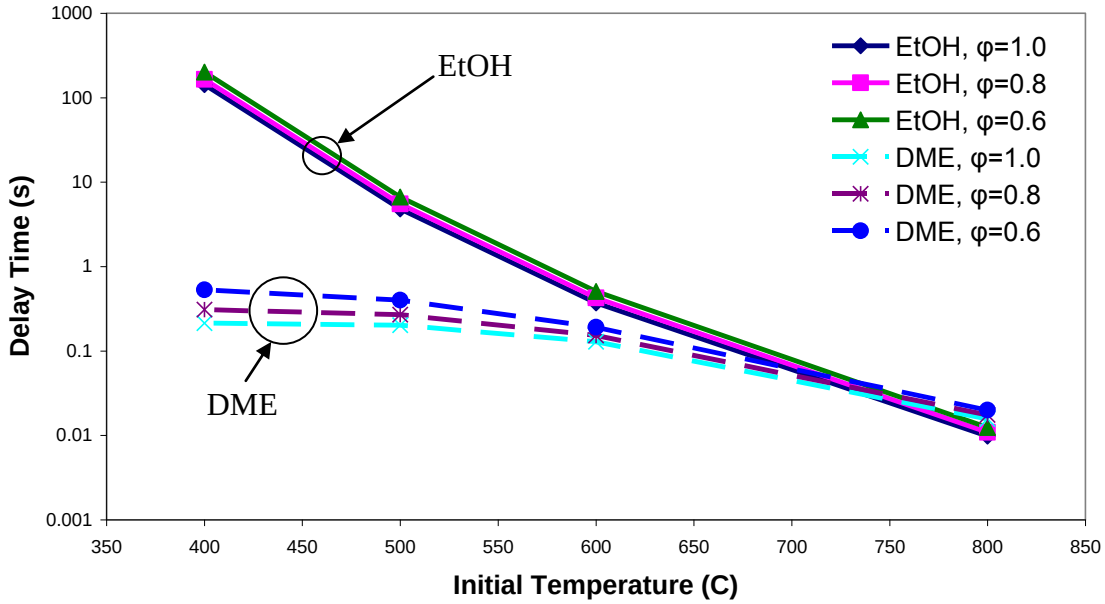

Figure 68: Computed ignition delay times for DME and EtOH diverge at temperatures below 700° C when solved at ambient pressures (1 bar, equivalence ratios of 0.6, 0.8, and 1.0).

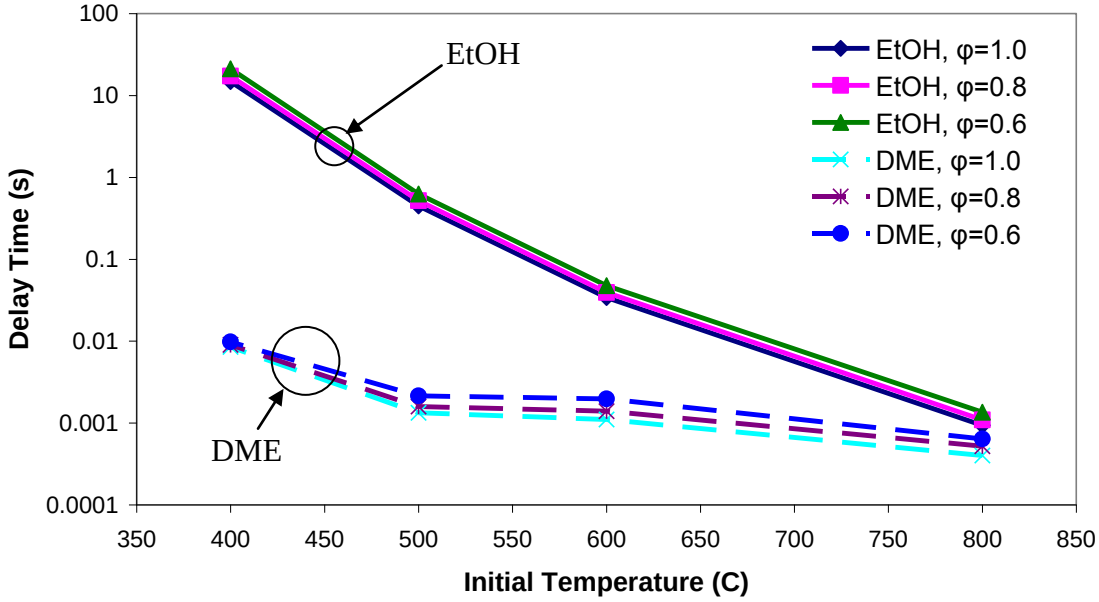

Figure 69: Computed ignition delay times for DME and EtOH diverge at higher temperatures when solved at elevated pressures (20 bar, equivalence ratios of 0.6, 0.8, and 1.0).

In Figure 68, at initial temperatures above 700^{o} C, differences between the two curves are indiscernible. Below 700^{o} C, however, the solutions diverge. Moreover, the fuel type has a much greater impact on ignition delay time than equivalence ratio. At an initial temperature of 400^{o} C, the expected ignition delay times differ by more than two orders of magnitude. The study suggests that observations differentiating DME and EtOH jet flames under identical test conditions are caused by autoignition when inlet temperatures are below 700^{o} C. A similar study

was also conducted at a pressure of 20 bar (Figure 69), which is a representative operational pressure within stationary gas turbine burners.

At 20 bar, onset of solution divergence occurs at higher temperatures than at 1 bar. Typical stationary gas turbine burners operate at pressures ranging between 20 and 40 bar. Assuming a second law compressor efficiency of 90%, these pressure ranges result in combustor inlet temperatures between 460^{o} C and 600^{o} C. Consequently, if it could be shown that combustion stability differs between DME and EtOH at a pressure of 1 bar under conditions that simulate the combustion environment within gas turbine burners, it is conservative to assume that combustion stability would also differ in the pressure range of 20 – 40 bar. It would then follow that autoignition is consistently an influential factor on combustion stability within gas turbine combustors. If combustion stability does not differ between DME and EtOH at 1 bar, experimental investigations at elevated pressures become paramount.

The same LLNL mechanisms were employed in a constant pressure batch reactor simulation for computing the ignition delay times for ethanol and DME. The equivalence ratios studied were 0.2 and 0.5, and reactor pressures of 1 bar and 20 bar were compared for these two equivalence ratios. Figure 70 compares the computed ignition delays versus 1000/T over the range of interest at an equivalence ratio of 0.5.

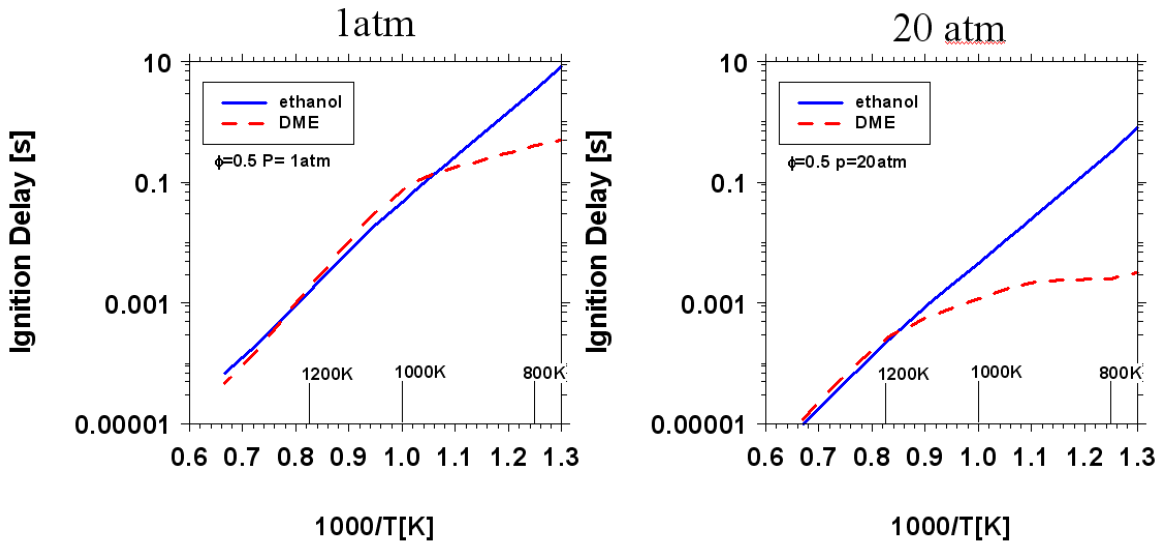

Figure 70: Ignition delay times versus inverse temperature for DME and ethanol at 1 bar and 20 bar with an equivalence ratio of 0.5.

As revealed in Figure 68 Figure 70, at temperatures above 1000 K should show no difference between DME and ethanol at atmospheric pressure.

This calculation was repeated at an equivalence ratio of 0.2.

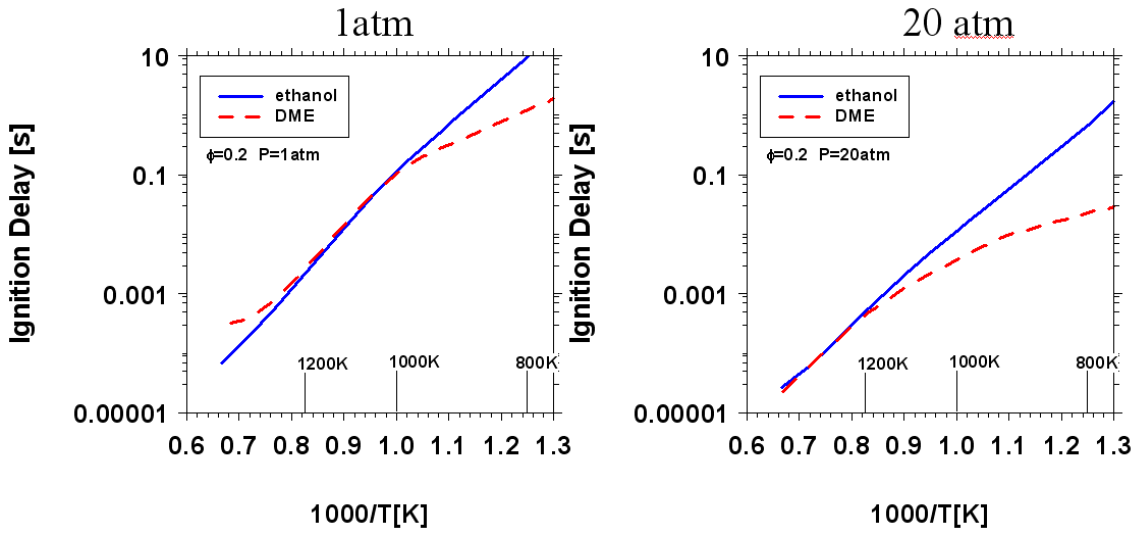

Figure 71: Ignition delay times versus inverse temperature for DME at 1 bar and 20 bar with an equivalence ratio of 0.2. Similar conclusions can be drawn from this computation as were drawn with an equivalence ratio of 0.5.

Again, no discernible difference is observed at 1 bar for temperatures greater than 1000 K.

A Perfectly Stirred Reactor (PSR) (also called a well mixed reactor, or continuously stirred tank reactor) computational study was then performed in guiding experimental investigations. The PSR is a zero-dimensional analysis with one inlet steam and one exit stream. The following parameters can be modified within the PSR computer code used:

- Residence time
- Initial temperature in the tank
- Temperature of the inlet stream
- Reactor pressure
- Initial composition in the tank
- Composition of the inlet stream

The purpose of this study was to determine the residence times at which blowout occurs when the inlet temperature and equivalence ratio are varied. By comparing the blowout limits computed for DME and EtOH, an experimental test matrix could be developed in a manner that maximizes the chances of capturing differences in flame stability. Figure 72 shows a representative curve generated from this analysis. The residence time at which blowout occurs, as identified in Figure 72, is recorded. Figure 73 summarizes the results of this analysis over a range of inlet temperatures from 400^{o} C to 800^{o} C and equivalence ratios from 0.6 and 1.0.

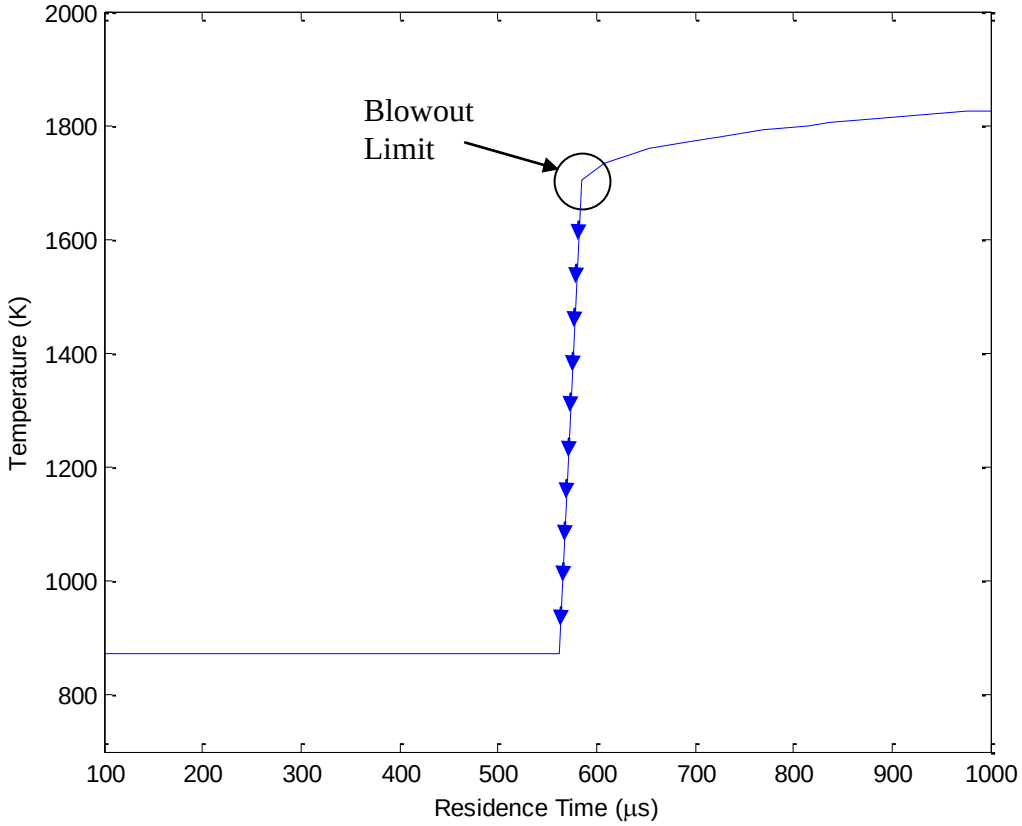

Figure 72: Characteristic result from numerical PSR study showing that the blowout limit is defined as the residence time at which further reductions in residence time no longer allow sustainable combustion (EtOH, 600^{o} C inlet temperature, an equivalence ratio of 0.6, and at a pressure of 1 bar).

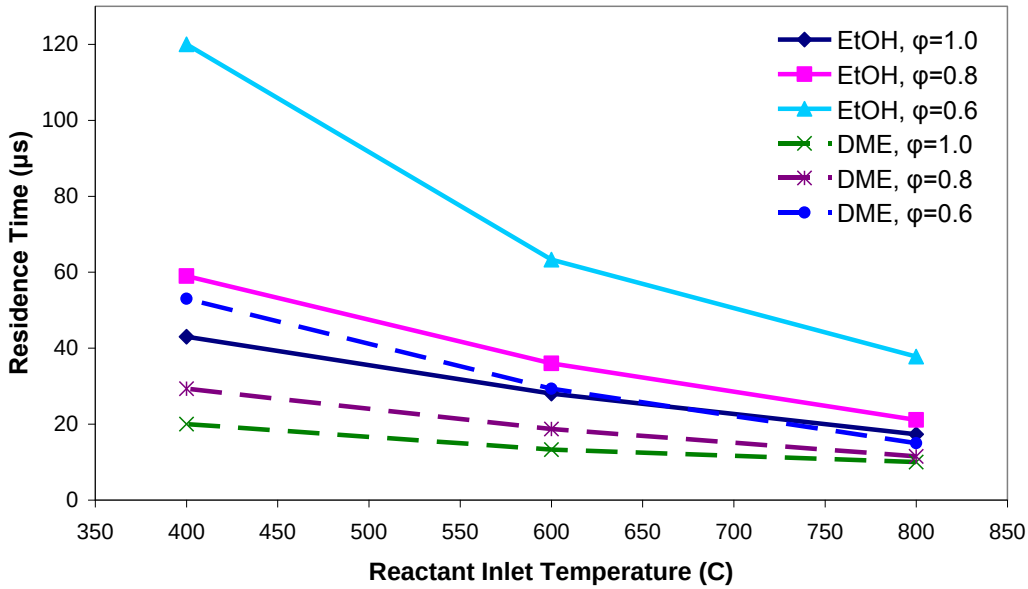

Figure 73: Perfectly Stirred Reactor simulations show that at 1 bar, DME has lower blowout limit residence times than EtOH.

It is clear that at low equivalence ratios and inlet temperatures, if the well mixed reactor assumption is valid, the blowout limits differ significantly between DME and EtOH.

This study was repeated at a reactor pressure of 20 bar, which is a pressure more representative of stationary gas turbine combustors. At elevated pressures, combustion stability differences between DME and EtOH are most pronounced in the lean regime found in stationary gas turbine combustors as shown in Figure 74.

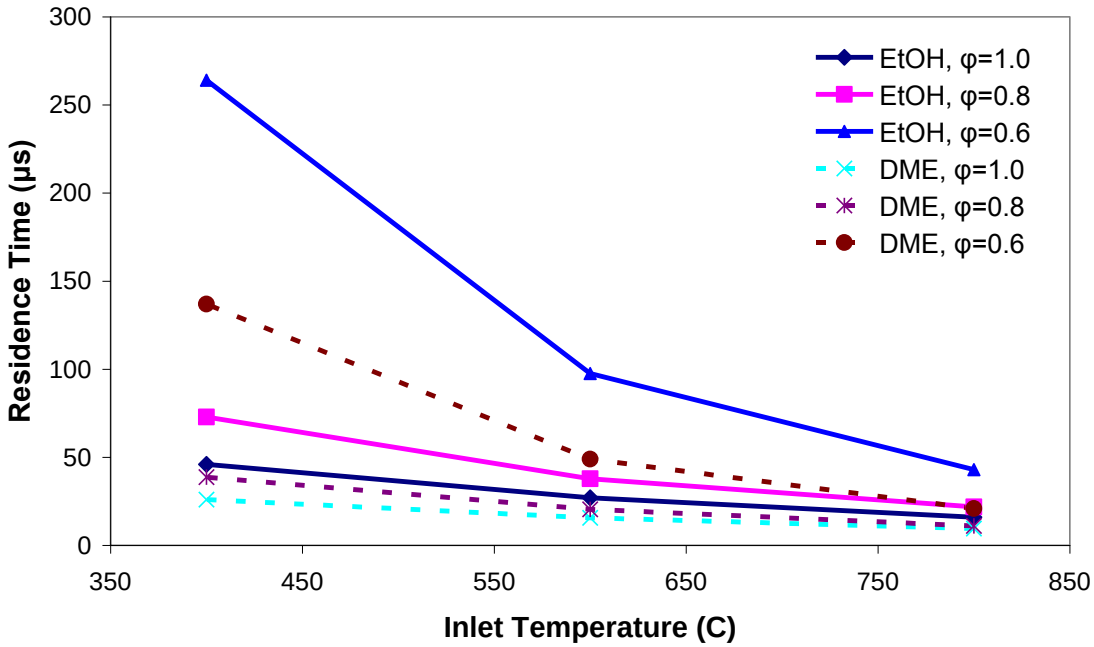

Figure 74: Perfectly Stirred Reactor simulations show that at 20 bar, computed blowout limit residence times differ by the greatest amount at low equivalence ratios.

Next, the perfectly stirred reactor was used to investigate the blowout characteristics under a broader set of conditions. Table 2 summarizes the computed blowout residence times for DME and ethanol.

Table 2: Blowout residence times of DME and Ethanol computed with the perfectly stirred reactor code.

ϕ	T_{inlet} [K]	P_{inlet} [atm]	DME [ms]	Temp [K]	Ethanol [ms]	Temp [K]
0.5	298	1.	0.7	1406	1.3	1390
0.5	298	5	1.	1490	1.5	1462
0.5	298	10	2.	1515	2	1472
0.5	298	15	2.5	1510	2.5	1467
0.5	298	20.	3.	1516	2.5	1439
0.5	500.	20.	0.3	1656	0.3	1589
1.0	298	1	0.06	1778	0.1	1751
1.0	298	5	0.015	1860	0.03	1849
1.0	298	10	0.010	1907	0.025	1949
1.0	298	15	0.009	1965	0.015	1904
1.0	298	20	0.008	1970	0.015	1969

b) Experimentally Contrasting DME Flames Versus EtOH Flames

A simple burner configuration was constructed for the initial experimental investigation of the autoignition research. It consists of a central main through which premixed DME or EtOH and air flows, and a coannular stream through which hydrogen flows. The hydrogen serves as a pilot, expanding the range of equivalence ratios and flow velocities that may be investigated. The burner is depicted in Figure 75. The H_2 piloted burner was used to carry out several experiments in comparing DME and EtOH flames. This investigation led to conclusions regarding effective ways of characterizing combustion behavior in preparation for experimental work which follows.

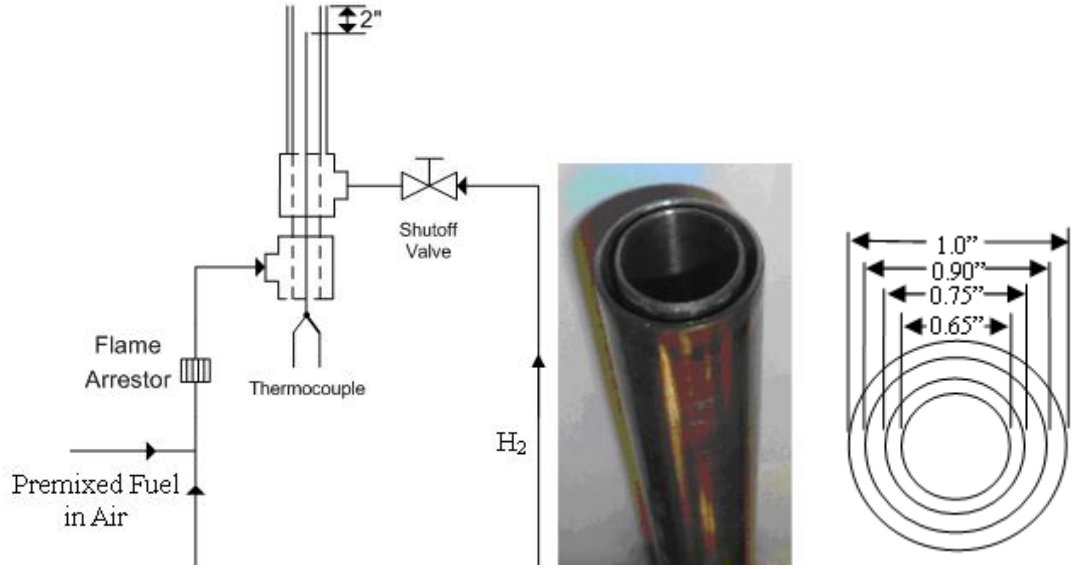

Figure 75: Flow diagram near the burner (left), coannular hydrogen piloted burner (middle), inner and outer dimensions of the flow passages on the coannular hydrogen piloted burner (right).

A fairly comprehensive flow schematic of the burner setup is depicted in Figure 76.

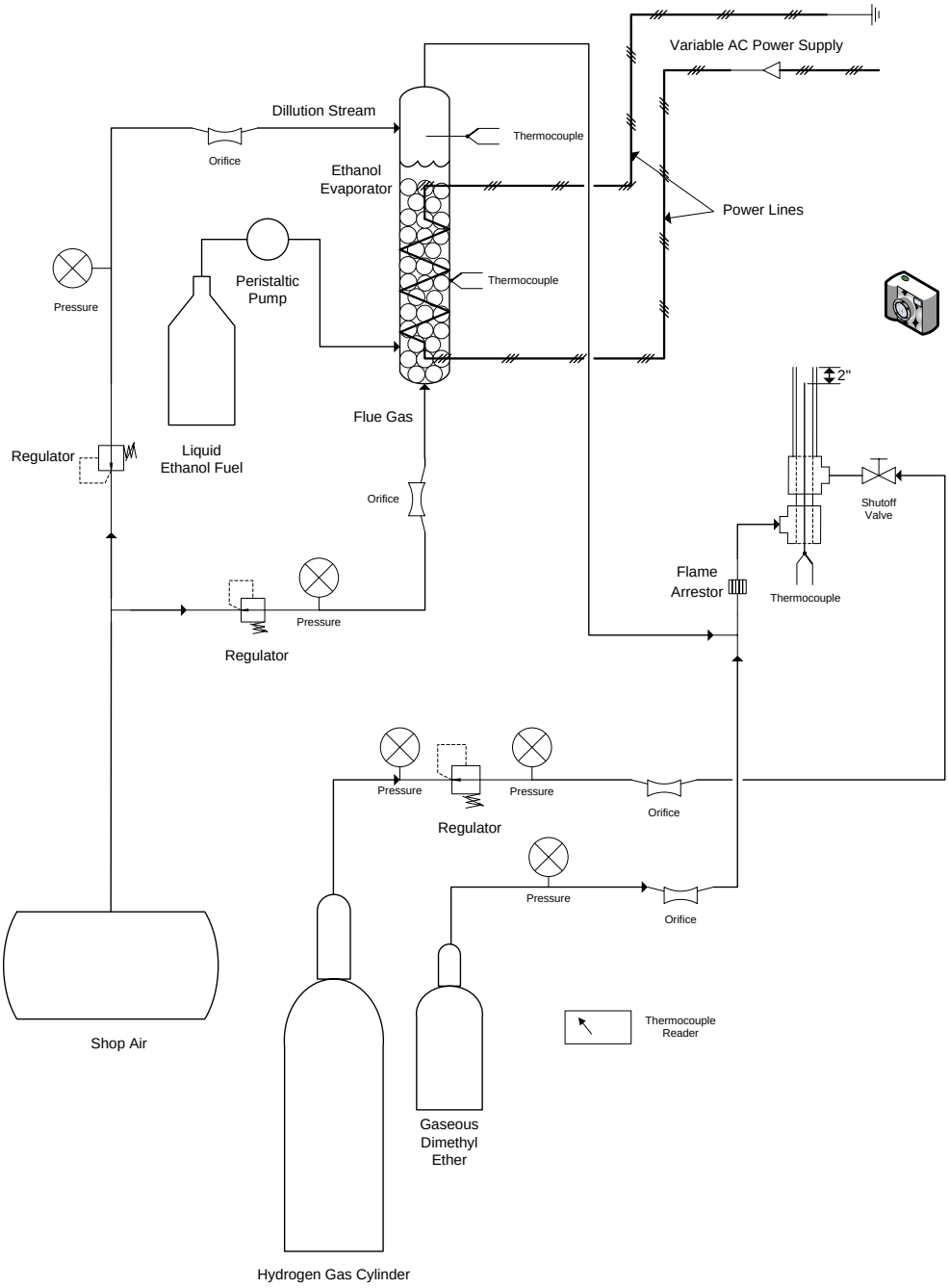

Figure 76: Flow schematic for the hydrogen piloted jet flame burner.

The shop air supply was used and was mixed with DME or ethanol. Ethanol was pumped by a high dynamic range peristaltic pump into an evaporator. The evaporator consisted of a tube filled with glass beads and ethanol. The temperature downstream of the liquid ethanol was measured and controlled such that the saturated concentration of ethanol in air is controlled to

the desired equivalence ratio. The DME flow rate was controlled with a sonic flow control orifice where pressure was measured upstream of the orifice.

The burner was mounted to a Unistrut structure, and the exhaust gases were routed to a fume hood where they were eventually expelled outdoors. Figure 77 shows a portion of the test setup including the evaporator and delivery lines. The perforated plate burner was mounted during the time that the photograph was taken instead of the single jet flame.

Figure 77: A portion of the burner setup is shown for reference.

The burner itself is shown in Figure 78 below:

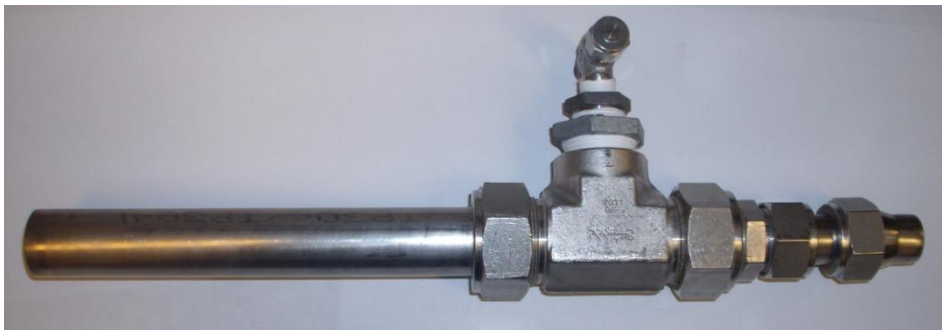

Figure 78: Primary components of the hydrogen piloted jet flame burner.

The main fuel and air mixture is routed through the inlet on the right had side of the figure. The hydrogen pilot stream is routed around the boundary of the ¾" OD main through the use of a 1" tee. The ¾" main tube is swaged onto the ¾" side of a 1" to ¾" reducer, but the tube itself actually continues all the way to the end of the 1" OD tube.

The main tube is kept coannular to the pilot tube through the use of three precision ground wedges spaced equally between the tubes. The wedges were positioned 1" upstream of the end of the burner in the effort to ensure that the pilot stream is not azimuthally dependant. Figure 79 shows the result.

Figure 79: Close up view of the annular tubes used to pilot the flame.

A thermocouple was placed within the main (not shown), with its tip located at the center of the tube approximately 1" from the exit of the burner to measure the influent air/fuel mixture temperature.

A thermocouple reader was employed to measure 1) the temperature of the strip heater that maintains the evaporator at the proper temperature, 2) the temperature of the air/ethanol mixture as it leaves the evaporator to ensure that the proper amount of ethanol was evaporated, and 3) the temperature of the air/fuel mixture just before it leaves the burner to ensure that inlet temperatures remain relatively constant from experiment to experiment. The thermocouple reader is depicted in Figure 80.

Figure 80: Thermocouple reader.

High speed direct imaging was used in analyzing the combustion behavior from the hydrogen piloted burner. High speed direct imaging is made much simpler with DME and EtOH flames because the luminosity is much greater with flames from these fuels than with H_2 flames. Figure 81 shows snapshots from videos which compare the detail produced from a standard frame rate video camera to a high speed video camera. Both images depict a case where the flame has lifted from the base of the burner.

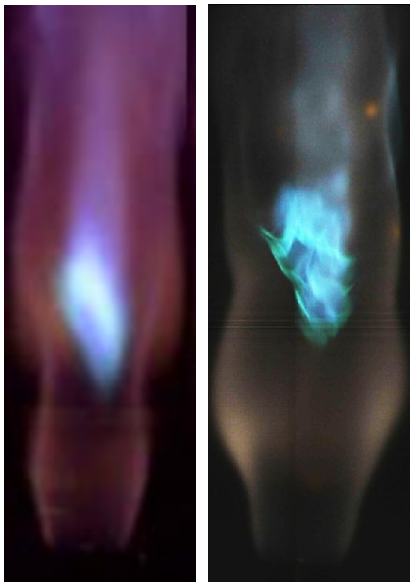
(a) (b)
Figure 81: Lifted DME flame image taken at 30 fps camera (left);
Lifted DME jet flame image taken at 1000 fps (right).

Figure 82 shows a variety of high speed imaging examples to show in more depth the utility of this diagnostic with these flames.

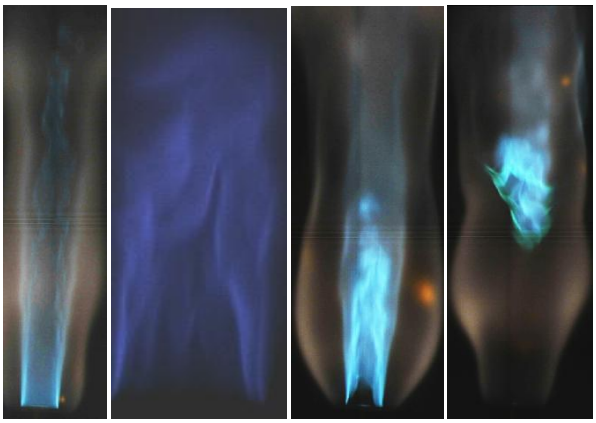

(a) (b) (c) (d)

Figure 82: High speed video screen captures. From left to right: (a) hydrogen piloted lean premixed DME flame, (b) Stoichiometric DME flame with no pilot, (c) hydrogen piloted rich DME flame near liftoff, (d) hydrogen piloted rich DME flame after liftoff.

The leftmost image depicts the DME flame near stoichiometric conditions with a hydrogen pilot. The nature of turbulence can be better understood through careful study of this image. The second image was taken with a lower flow rate so that a stable flame could be produced without a hydrogen pilot. The three dimensional nature of turbulence can be seen from this image. The two rightmost images show the DME flame just before and after liftoff. The lifted flame is highly turbulent and produces a considerable amount of audible noise.

The high speed video results give an instantaneous depiction of the flame, allowing detailed conclusions to be made regarding flame behavior. A diagnostic which is less useful with experimental investigations of H_2 jet flames. The highly detailed features that can be identified from Figure 82 indicate that high speed video footage allows detailed analysis of flame behavior to be made. Contrasting Figure 82 from Figure 81, it is clear that the lifted flame in Figure 81 is a time averaged image resulting from a slow shutter speed, resulting in a lack of detail in regard to how the flame behaves under highly turbulent conditions where reaction rates are the greatest. This research was the initial motivation for using high speed video for the VCB experimental research which followed.

Figure 82 shows an example comparison of attached DME and EtOH flames from this apparatus.

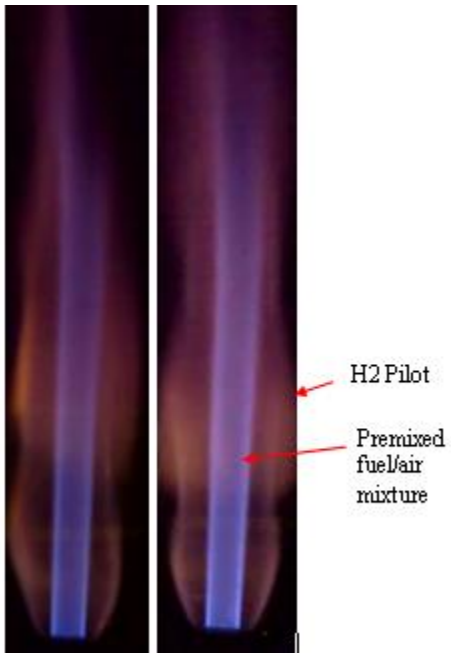

Figure 83: Comparison of attached flames produced by EtOH (left) and DME (right).

It was found that under most conditions, attached DME and EtOH flames appear nearly identical.

Onset of flame liftoff consistently occurs with these flames under rich conditions. Liftoff did not occur under lean operation except when onset of liftoff had already been achieved through rich combustion and subsequent equivalence ratio reduction. The flame then reattached once the fuel supply was reduced to the point of essentially no fuel flow. Figure 84 depicts images of the DME lifted flame right after liftoff occurs under lean conditions, as well as the lifted flame produced once lean conditions were returned.

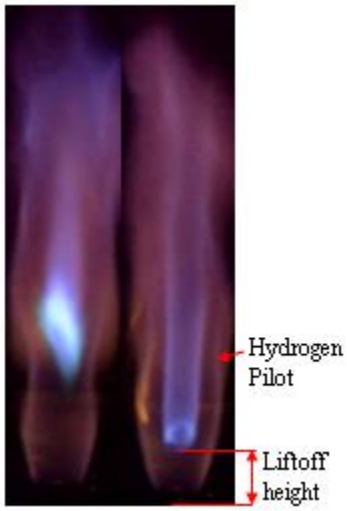

Figure 84: Lifted premixed DME jet flame under rich conditions (left), Lifted premixed DME jet flame under lean conditions (right).

In general, results agree exceptionally well between the DME and ethanol flames. Figure 85 depicts images from a gradual ramp-up of equivalence ratio increases for EtOH.

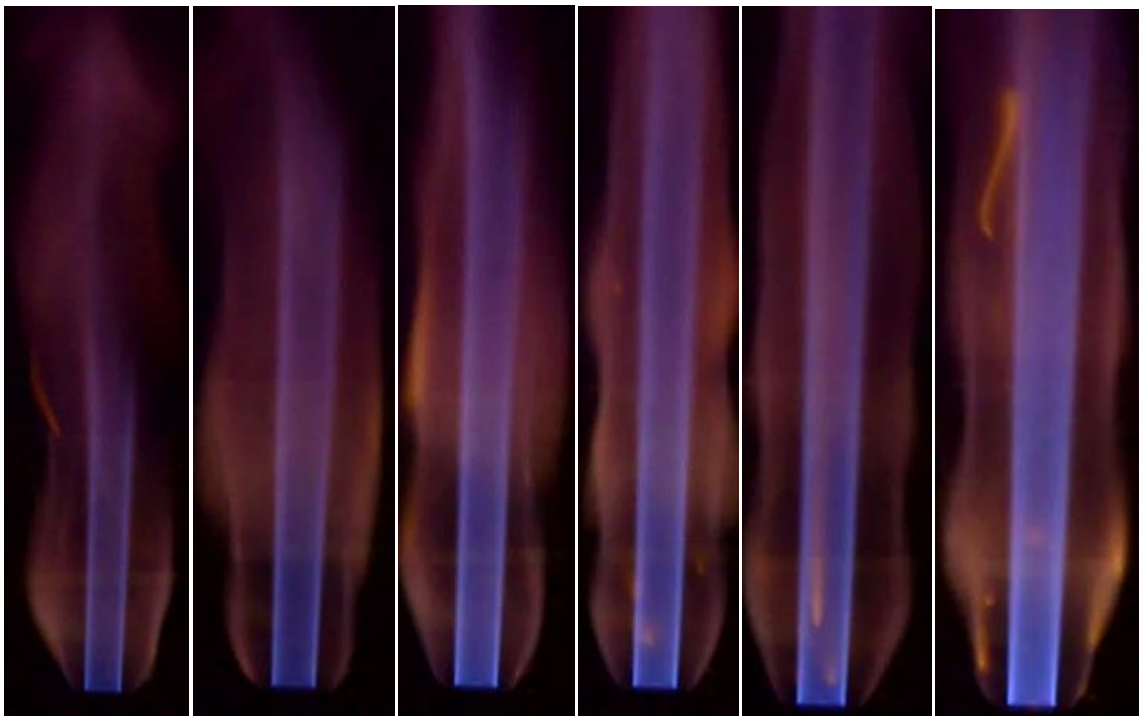

φ=0.1 φ=0.2 φ=0.5 φ=0.6 φ=0.7 φ=0.8

Figure 85: Flames produced by premixed ethanol and air at several equivalence ratios with a hydrogen pilot.

It is clear that the luminosity of the flame increases as the equivalence ratio is increased, but the overall flame structure remains relatively constant.

Similar results were obtained from tests with DME fuel. Because DME is a gas at room temperature, a broader range of equivalence ratios were able to be studied with DME. Figure 86 shows representative images from these tests.

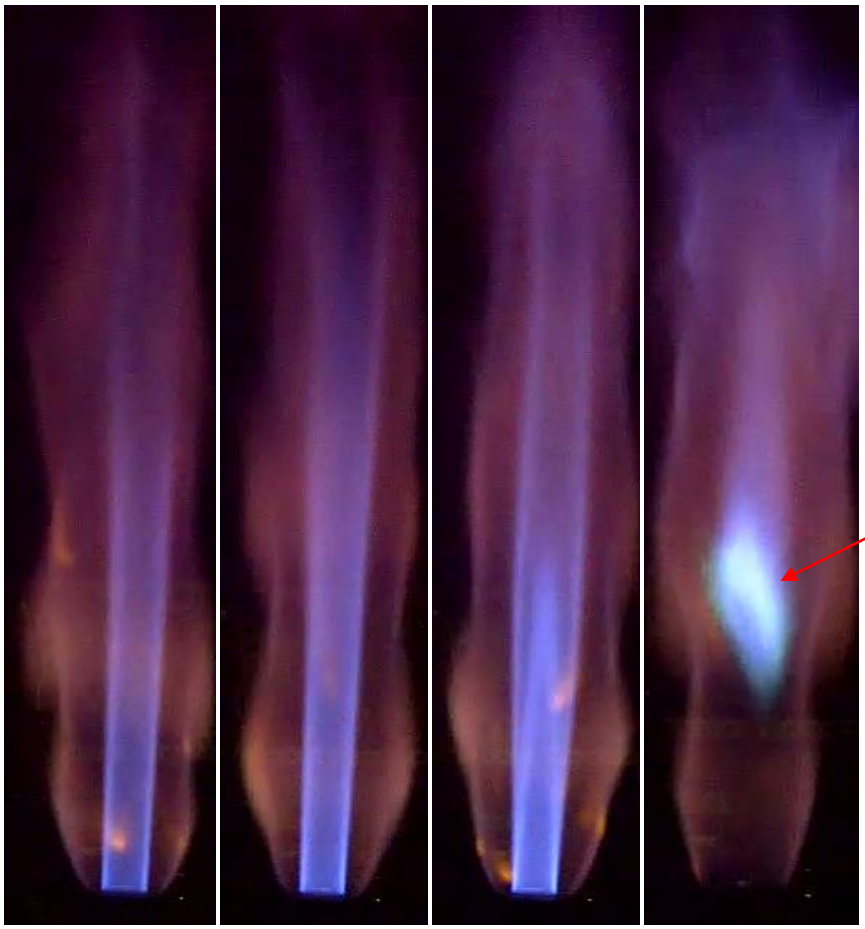

Figure 86: Flames produced by premixed DME and air at several equivalence ratios with a hydrogen pilot.

Notice that a double flame is produced under fuel rich conditions, and soon beyond this point liftoff occurs. This lifted flame is characterized by a bright green ring, which indicates the formation of an ethyl (carbon to carbon) bond. After the flame has lifted, it does not reattach to the base, even under lean conditions until the equivalence ratio has dropped to essentially zero.

The blowout limits of EtOH and DME jet flames were then measured and the results are reported in Figure 87.

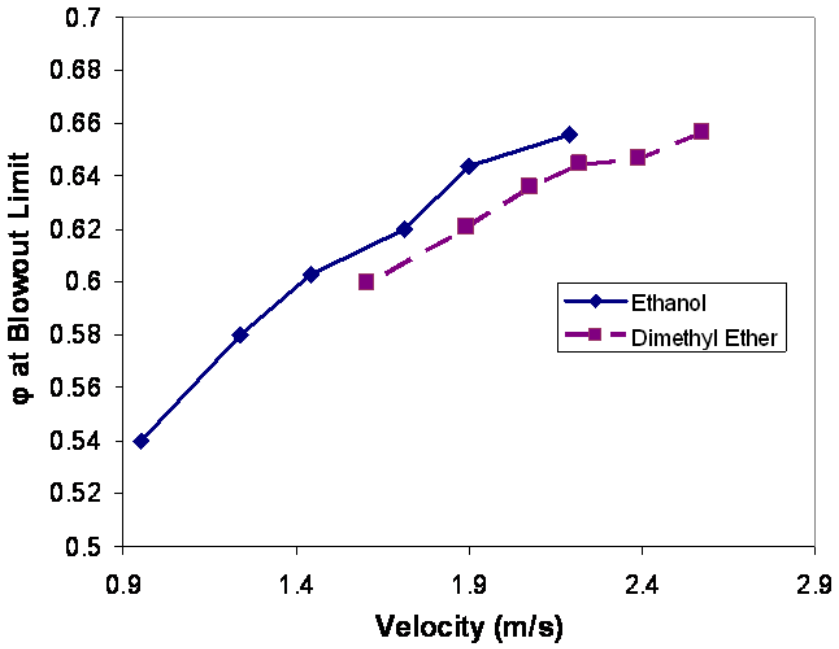

Figure 87: Experimentally measured blowout limits for DME and EtOH.

Again, minimal differences are observed between DME and EtOH experimentally. It should be noted that this burner, with its H_2 pilot, was not testing the sub 1000 K region. Yet, this sub 1000 K region exists for the inlet gases in gas turbine combustors. At 20 atmospheres, deviations between the ignition delay times between the two fuels occur at even higher temperatures, and thus deviations between flame stabilization characteristics are expected to be even more pronounced at the elevated pressure conditions of the gas turbine combustor. Despite the similarities observed in the experimental results between DME and EtOH flames, these points as well as the numerical results suggest that autoignition is still a stabilization mechanism which needs to be considered in premixed gas turbine combustors.

ii. *Atmospheric Pressure VCB Results*

The foundational worked was utilized in crafting the subsequent VCB research which is detailed next.

a) Stability Regimes Diagrams

Figure 88 presents stability regime diagrams produced from the atmospheric pressure VCB for V_{jet} = 300 m/s, 400 m/s and 500 m/s with $\varphi_{co-flow}$ (and hence $T_{co-flow}$) and y_{N2} as the two independent parameters. Results are illustrated with $\varphi_{co-flow}$ on the primary x-axis and with the correlated $T_{co-flow}$ on the secondary x-axis. As shown in Figure 88, four distinct regions of the stability regime diagrams are identified; an attached flame, a lifted flame, a blown-out flame and an unsteady flame. For $\varphi_{co-flow} < 0.15$, the co-flow is blown-out (does not remain lit), thus no data points are generated in the region between $0 < \varphi_{co-flow} < 0.15$. A stability regime is drawn for $0 < \varphi_{co-flow} < 0.15$ nonetheless in allowing placement of a label of the lifted regime for the low V_{jet} cases where the actual lifted regime is small. Therefore the stability limits for $0 <$

$\varphi_{co-flow}$ < 0.15 are implied and not measured. The dashed line for the V_{jet} = 500 m/s cases indicates the boundary between the lifted and unsteady regimes.

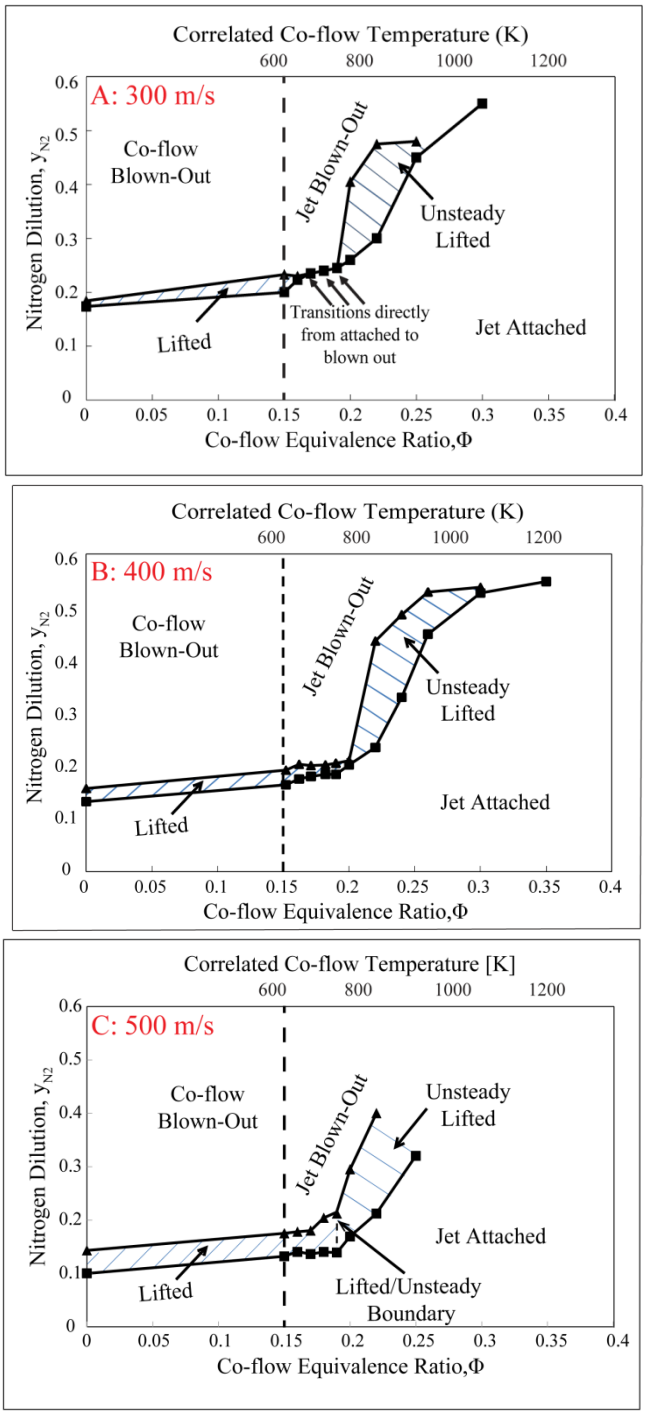

Figure 88: Stability regimes Diagrams which map the flame stabilization behavior for A) V_{jet} = 300 m/s, B) V_{jet} = 400 m/s, and C) 500 m/s.

In the lifted regime, the transition from attached to lifted is abrupt. For y_{N2} values immediately below the lifted regime transition, no visible indicators that the flame is nearing liftoff are

observable. Similarly, in the unsteady regime, the transition from attached to unsteady is abrupt so these transitions are easily delimited. At lower jet velocities and for $0.15 \leq \varphi_{co-flow} \leq 0.20$, the jet transitions from an attached flame to a blown-out one, with no lifted region. Increasing the jet velocity broadens the lifted regime for $0.15 \leq \varphi_{co-flow} \leq 0.20$. For $\varphi_{co-flow} < 0.20$ the co-flow temperature is below the autoignition temperature, meaning that the temperature of any mixture between the fuel (at 293 K) and co-flow (300 K for air at $\varphi_{co-flow} = 0$ and 810 K for $\varphi_{co-flow} = 0.20$) is below the autoignition temperature. Therefore autoignition cannot be the sole flame stabilization mechanism, and tribrachial flame propagation is likely influential for $\varphi_{co-flow} < 0.20$. As $T_{co-flow}$ surpasses the autoignition temperature (near and beyond $\varphi_{co-flow} > 0.20$), increasingly greater y_{N2} values are necessary for jet detachment. For example, Figure 88C shows the stability regime diagram for $V_{jet} = 500$ m/s. The slope of the boundary line between attached and lifted regimes for $0.15 < \varphi_{co-flow} < 0.20$ is much shallower than the slope of the regime boundary line for $\varphi_{co-flow} > 0.20$. For $\varphi_{co-flow} > 0.20$ with increasing y_{N2}, the jet no longer transitions from attached to lifted, but rather from attached to unsteady.

Had y_{N2} been ramped down instead of up, the attached-lifted boundary is slightly reduced owing to hysteresis. However, the stability boundaries in the unsteady regime are unaffected by hysteresis. Cases where y_{N2} are ramped down are not investigated extensively for simplicity since the primary focus of this research is on analyzing liftoff height variation in the lifted regime. Stability hysteresis on $\varphi_{co-flow}$ and V_{jet} slightly affect the stability regimes layout, though for the burner configuration used, stability is most sensitive on y_{N2}, so these hysteresis effects are likely less influential than hysteresis on y_{N2}. Additionally, $\varphi_{co-flow}$ and V_{jet} are fixed in the development of the stability regimes diagrams in reducing the impacts of hysteresis on $\varphi_{co-flow}$ and V_{jet}.

The relatively small inner diameter of the jet used (2.4 mm) leads to high strain with weak tribrachial characteristics which prohibits stable lifted flames when $\varphi_{co-flow} > 0.20$. Peters [17] explains why diffusion flame quenching is responsible for the liftoff of an initially attached flame. When the jet diameter is smaller than the threshold value of ~3 mm (above which liftoff height is linearly dependent on jet velocity) laminar diffusional flamelet quenching drives the stabilization point beyond the threshold liftoff height of $L = 40$ diameters, resulting in flame instability. Consequently, for $\varphi_{co-flow} > 0.20$, stable lifted flames cannot be generated with the burner configuration used since the co-flow temperature is greater than the autoignition temperature. However, the jet is capable of re-igniting once an autoignition event strong enough for full jet ignition becomes favorable, and the cycle is repeated [36]. The frequency of these ignition and subsequent blowoff events ranges between 0 Hz and 30 Hz depending on V_{jet}, $\varphi_{co-flow}$, and y_{N2}.

The unsteady combustion mode is characterized by a loud "popping" sound emanating from the flame with intermittent chemiluminescence. High speed video of these events revealed that the flame continuously blows out, and then relights. The relighting events occur within a single frame at a frame rate of 600 Hz. If flame propagation caused these relighting events, the flame speed would need to be at least 28 m/s greater than the jet velocity because the physical heights of the images generated at 600 Hz are approximately 46 mm ($V_{propagation} - V_{jet} \geq 600$ Hz x 46 mm = 28 m/s). Consequently, the relighting events occur either via a broad autoignition event or due to the flame propagating against the flow at a flame speed much higher than that observed at

$\varphi_{co\text{-}flow}$ < 0.20. If the relighting events occur via flame propagation, it is unclear why the flame speed rapidly increases at $\varphi_{co\text{-}flow}$ = 0.20. The unsteady regime was further characterized later and these results will be detailed in section 4.e).

The cases with jet velocities of 500 m/s, 600 m/s, and 700 m/s show broad regions of lifted and unsteady flames. For the case with a jet velocity of 500 m/s, the lifted to unsteady transition, which still occurs at an equivalence ratio $\varphi_{co\text{-}flow}$ = 0.20, is marked by two distinct stability regimes. In one stability regime (0.17 < y_{N2} < 0.22), the flame oscillates between an attached and lifted flame, with the flame propagating between the two modes. In the other stability regime (0.22 < y_{N2} < 0.30), the flame oscillates between a lifted flame and a blown out flame. Under these conditions, it appears that the relighting event occurs via autoignition because relighting occurs within a single frame of video taken at 600 frames per second. The transition between these two operational regimes occurs at $y_{N2} \approx 0.22$.

For jet velocities of 600 m/s and 700 m/s, the upper bound of the unsteady stability regime could not be determined because more nitrogen would be required than the flow control system can accurately deliver to determine this upper bound. The incomplete upper bound stems from the fact that for $\varphi_{co\text{-}flow} \geq 0.20$, V_{jet} would need to be greater than the sonic velocity of the jet fluid in the nozzle to achieve a fully blown-out condition for these cases and a converging-diverging nozzle is not used. Consequently, the stability regimes diagrams developed for V_{jet} = 600 m/s and V_{jet} = 700 m/s are less complete than those developed for V_{jet} values of 300 m/s, 400 m/s and 500 m/s, and so these results are presented separately in Figure 89.

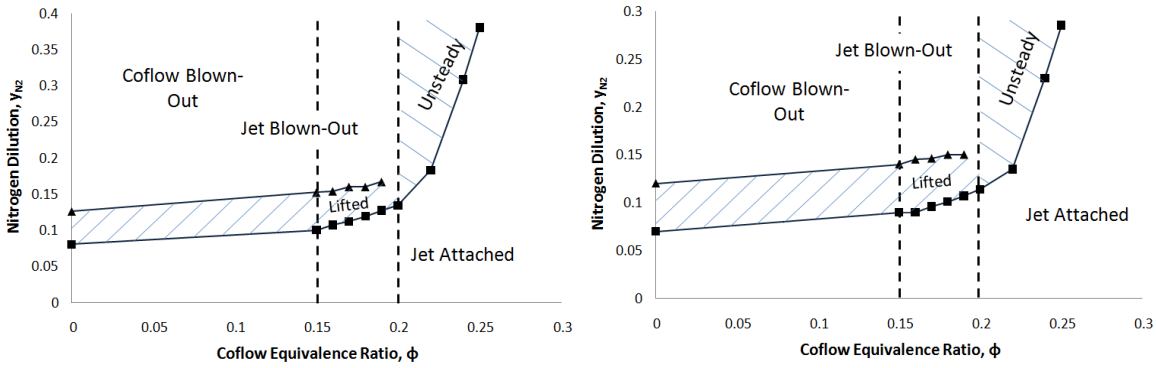

Figure 89: Stability regimes diagrams developed for with V_{jet} values of 600 m/s (left) and 700 m/s (right).

The stability regimes diagrams serve as a convenient tool for predicting H_2-in-N_2 flame behavior under various conditions and for analyzing the numerical and experimental results when available.

b) Numerical Stability Regimes Analysis

The stability regimes are analyzed in a parallel research effort by Frederick et. al. [37]. For lower co-flow temperatures ($T_{co-flow}$ < 810 K, $\varphi_{co-flow}$ < 0.20), it is argued that the flame is mostly stabilized by tribrachial flame propagation due to the low mixture temperature and hence long autoignition delay time. As $\varphi_{co-flow}$ approaches 0.20 autoignition likely becomes more influential. As expected, below $\varphi_{co-flow}$ = 0.20, the RANS parabolic code does not predict a flame stabilized by autoignition and solves only the non-burning flow field. Thus, when predicting

zones where $S_T > \langle U \rangle$, if no flame exists from autoignition, the density (and hence velocity) is not exact. However, the intent of the simulations is to capture the trend in supporting the assumption that propagation dominates flame stabilization in this regime ($\varphi_{co-flow} < 0.20$), and the trend is captured with this method. Maps where $S_T > \langle U \rangle$ are created and depicted in Figure 90 through Figure 92 in investigating regions where a propagating flame could exist and to predict whether the flame is attached, lifted, or blown-out. Presented results are only for V_{jet} = 500 *m/s*, as similar trends are seen for all jet velocities considered (300 m/s, 400 m/s, and 500 m/s).

Results for $\varphi_{co-flow} = 0.15$ ($T_{co-flow}$ = 665 K where the autoignition delay time is too long for autoignition dominated stabilization) are shown in Figure 90. The experimental trend shown in Figure 88 of attached, to lifted, to blown out, is satisfactorily captured. Increasing N_2 dilution reduces the size of the region where $S_T > \langle U \rangle$, until the flame ultimately is not stable around 20% N_2 dilution. Considering next $\varphi_{co-flow} = 0.20$ ($T_{co-flow}$ = 810 K where the autoignition delay time is also too long for a flame to be predicted by the code), a satisfactory trend is again captured, as shown in Figure 91. Around $\varphi_{co-flow}$ =0.225 ($T_{co-flow}$ = 880 K) autoignition becomes important. Figure 92 shows temperature contours which indicate an autoignition flame. Regions where $S_T > \langle U \rangle$ are overlaid onto the temperature profile, which show the flame varying from attached to nearly blown-out, again consistent with the trend in the experimental data. Similar trends are seen for cases with different values of V_{jet}.

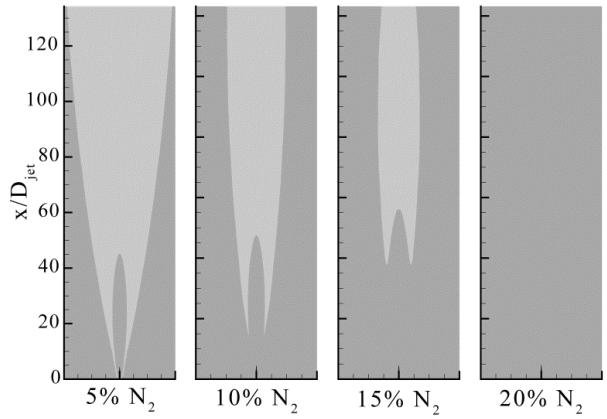

Figure 90: RANS Stability Predictions 1. For $\varphi_{co-flow} = 0.15$, the 1D steady parabolic code, showing regions where $S_T > \langle U \rangle$, accurately captures the effect of increasing N_2 fuel jet dilution from 5% to 20% in determining stability.

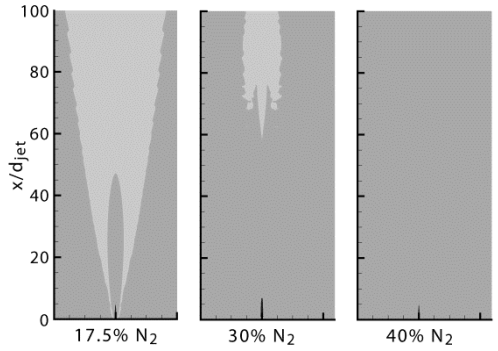

Figure 91: RANS Stability Predictions 2. For $\varphi_{co-flow} = 0.20$, the simulations again accurately capture the experimental trend of the stability regime diagrams.

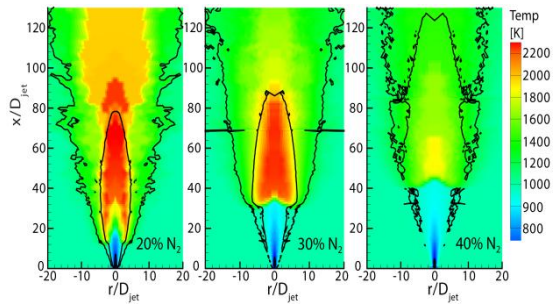

Figure 92: RANS Stability Predictions 3. For $\varphi_{co-flow} \geq 0.20$ ($\varphi_{co-flow} = 0.225$ here), increasing the N_2 fuel jet dilution from 20% to 40% thins the regions where a flame could stabilize and diminishes the autoignition propensity. As expected, the parabolic code accurately predicts an autoignition stabilized flame.

The results suggest that flame propagation indeed plays a role in flame stabilization, especially for $\varphi_{co-flow} < 0.20$. However, further work is necessary to correctly encapsulate the effects of N_2 dilution. Another possible approach is to investigate tribrachial flames directly by using a tribrachial flame speed. Generally, tribrachial flames propagate at $2.6S_T$. Thus, the ability of a simple flame speed correlation to correctly capture the trend reinforces the hypothesis that flame propagation plays a significant role for flame stabilization for a jet in a co-flow, especially when the co-flow is not hot enough for autoignition.

c) Liftoff Height Characterization

Experimental Results

Concurrently in the development of the stability regimes diagrams, the liftoff heights under the same conditions were measured using the methodology outlined in the section on experimental methods. Figure 93 summarizes these results. Note that the liftoff height results presented are fundamentally distinct from those measured by Cabra et al [11] as the co-flow temperature ranges investigated do not overlap between the present research and Cabra's work and because of the aforementioned fluid dynamic effects resulting from the jet nozzle diameter adjustment. At any fixed V_{jet} and y_{N2} condition, a marked difference in liftoff heights is not observed as the co-flow equivalence ratio is increased beyond $\varphi_{co-flow} = 0.15$ ($T_{co-flow} = 660$ K) until $\varphi_{co-flow} = 0.20$ ($T_{co-flow} = 810$ K). Above $\varphi_{co-flow} = 0.20$, autoignition is likely the dominant flame stabilization mechanism, which explains the differing liftoff heights for $\varphi_{co-flow} = 0.20$. Furthermore, a maximum non-dimensional liftoff height of approximately $L/d_{jet} \approx 24$ is observed. These results suggest that in practical combustors, when H_2 mixes with products originating at equivalence ratios near 0.20, numerical models which incorporate autoignition and flame propagation should be employed for optimal model accuracy. Figure 93 also demonstrates the significant degree of scatter in liftoff heights which results when 3 independent parameters are varied.

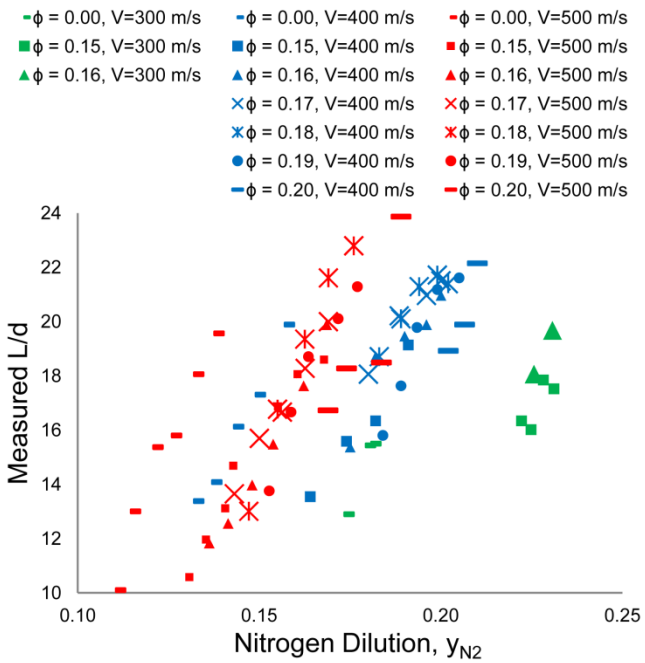

Figure 93: Experimentally measured liftoff heights versus N_2 dilution for various jet velocities and co-flow equivalence ratios.

d) Liftoff Height Correlation Development

Kalghatgi's Correlation

The liftoff height in the steady lifted regime is investigated in detail ($0.15 < \varphi_{co\text{-}flow} < 0.20$). First, Kalghatgi's correlation [16] is used in investigating whether the correlation can accurately capture the influence of varying y_{N2} on L while the $\varphi_{co\text{-}flow}$ is varied:

$$L = 50 \frac{\nu_{jet} V_{jet}}{S_{L,max}^2} \left(\frac{\rho_{jet}}{\rho_\infty}\right)^{1.5} \qquad (17)$$

where ν_{jet} is the kinematic viscosity of the jet, ρ_{jet} is the density of the jet, and ρ_∞ is the ambient density (co-flow density). Kalghatgi's correlation has been previously shown to accurately predict liftoff heights for hydrocarbon jet flames, H_2 jet flames, and H_2 jet flames diluted with hydrocarbons and CO_2 [51]. However, note that Kalghatgi did not have a co-flow, heated or otherwise, in developing the correlation.

Measured liftoff heights are plotted against those predicted by Kalghatgi's correlation with the jet mixture kinematic viscosity calculated using the methodology outlined in a NASA Technical Note by R. S. Brokaw [52]. Results of the comparison between measured results and those predicted by Kalghatgi's correlation are shown in Figure 94. These results indicate that Kalghatgi's correlation correctly predicts the range of liftoff heights, but has trouble accurately predicting the effect of y_{N2} with a hot co-flow. Figure 95 shows Kalghatgi's correlation versus y_{N2} for the cases investigated. For hot co-flow cases ($\varphi_{co\text{-}flow} \geq 0.15$) Kalghatgi's correlation predicts only a weak dependence of L on y_{N2} whereas a strong dependence was observed experimentally. For the cold co-flow cases ($\varphi_{co-flow} = 0.00$), Kalghatgi's correlation shows better

agreement with the experimental data for increasing y_{N2}. Discrepancies for the cold co-flow cases are attributable to the influence of the co-flow velocity on forcing the stabilization zone downstream, as explained by Montgomery et. al. [53]. Despite the accuracy of Kalghatgi's correlation [51] without a co-flow, these results imply that for heated environments, caution should be used when applying the correlation.

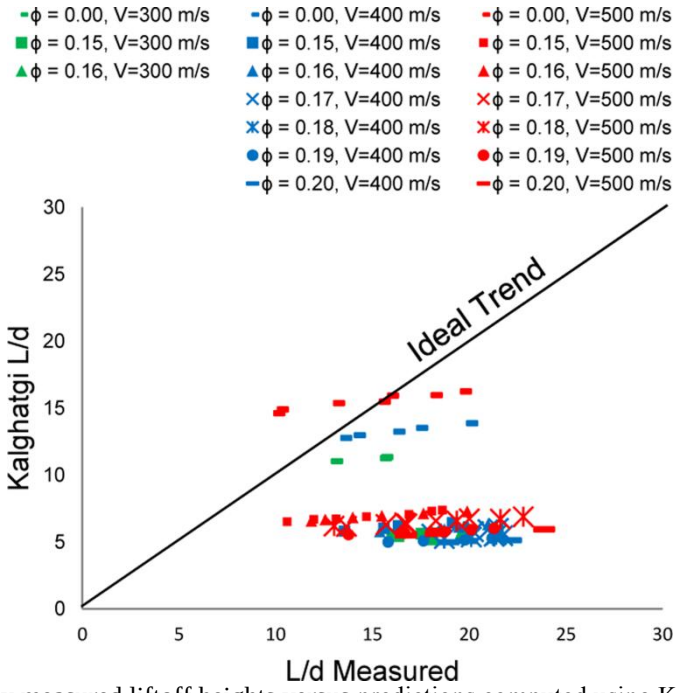

Figure 94: Experimentally measured liftoff heights versus predictions computed using Kalghatgi's correlation for various jet velocities and co-flow equivalence ratios.

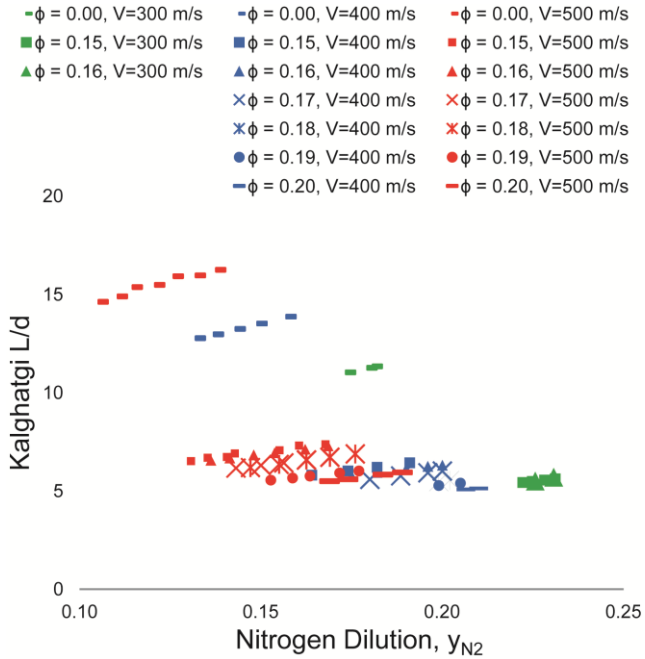

Figure 95: Liftoff height predictions from Kalghatgi's correlation versus N_2 dilution for the conditions investigated experimentally.

Numerical Liftoff Height Modeling using RANS Method

Another method for predicting liftoff height is comparing areas where the turbulent flame speed is greater than the local mean velocity as explained in the Numerical Methods Section [37]. The results are shown in Figure 96. Clearly, the predicted liftoff heights deviate markedly from the experimental results despite the fact that the same method worked well in predicting when the flame will be attached, lifted, or blown-off. For the cold co-flow cases ($\varphi_{co-flow}$ = 0.00), the simulations predicted no flame due to the much lower laminar flame speed resulting from the low temperature mixture of fuel and co-flow. It is therefore argued that a propagating flame exists in the domain for sustainment of a steady lifted flame, but at the liftoff location, an only partially premixed environment exists where the equivalence ratio is too rich for premixed flame propagation. The turbulent premixed flame downstream of the liftoff location is necessary for stability, but another mode of flame stabilization is responsible for anchoring the flame at the liftoff location. These results further indicate that the flame stabilization mechanism at work is tribrachial flame propagation.

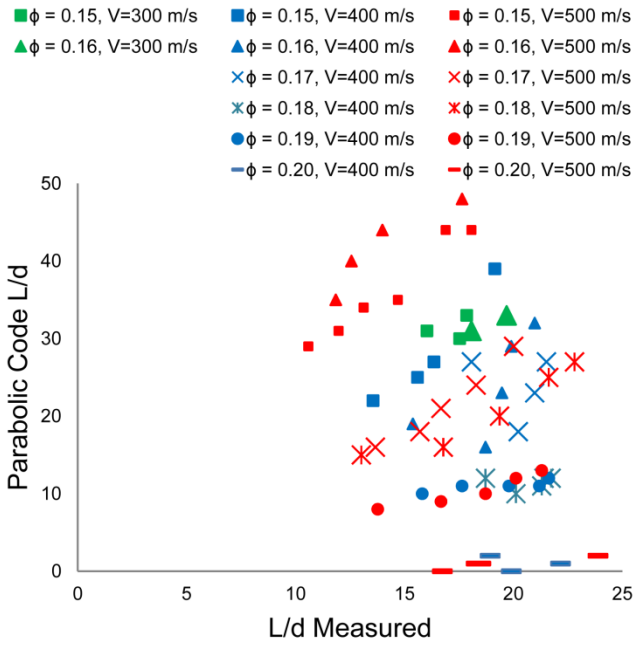

Figure 96: Experimentally measured liftoff heights versus simulated liftoff heights from the 1D RANS parabolic code. The magnitude is not correctly captured, however the effect of N_2 dilution is correctly captured.

Normalization by Damköhler Number

Prior work [54] [55] suggests that the Damköhler number definition derived from large-scale turbulence quantities is equally applicable to small-scale turbulence quantities, and vice versa. In taking advantage of this hypothesis, the Damköhler number is used in investigating whether liftoff heights can be characterized solely by this parameter. The Damköhler number is computed using two methods, both utilizing density weighting [56] in computing an effective velocity near the flame. The first Damköhler number definition, Da_1, uses the jet diameter for computing the flow time scale:

$$Da_1 = \frac{\tau_{flow}}{\tau_{chem}} = \frac{d_{jet}/\left(V_{jet}\left(\rho_{jet}/\rho_{\infty}\right)^{1/2}\right)}{\delta/S_L} \qquad (18)$$

where τ_{flow} is the flow time scale, τ_{chem} is the chemical time scale, S_L is the flame speed, and δ is the flame thickness. The chemical time scale in the denominator of *Da* motivates the utilization of a computational model in lieu of experimental methods for complexity reduction. The methodology used in computing τ_{chem} is outlined in section 2.ii.i. An example τ_{chem} computation set is shown in Figure 97, with $\overline{\varphi}_{Global}$ (equivalence ratios encountered as the jet reactants mix homogeneously with co-flow products) on the x-axis and the laminar flame speed (S_L), the flame thickness (d), and the flame time (τ_{chem}) on the y-axes. τ_{chem} and d share the same y-axis on the right hand side of Figure 97 because the order of magnitude of the values are similar, so the units are given next to the plot labels. The minimum flame time on the lean side (near $\overline{\varphi}_{Global}$ = 0.4) is not used because as fluid from the jet moves downstream and is entrained by the co-flowing products, the mixture starts richer and become leaner. Consequently, the first minimum in chemical time scale that the mixture encounters is at a rich equivalence ratio. If the flame stabilized later, on the lean side, any downstream deviation from the stabilization point would move the flame toward an even leaner zone with a longer flame time. On the rich side, however, perturbations that move the stabilization zone downstream result in ignition compositions closer to stoichiometric where flame stability is enhanced. As a result, the flame time on the rich side is a stable minimum, whereas the minimum on the lean side is unstable.

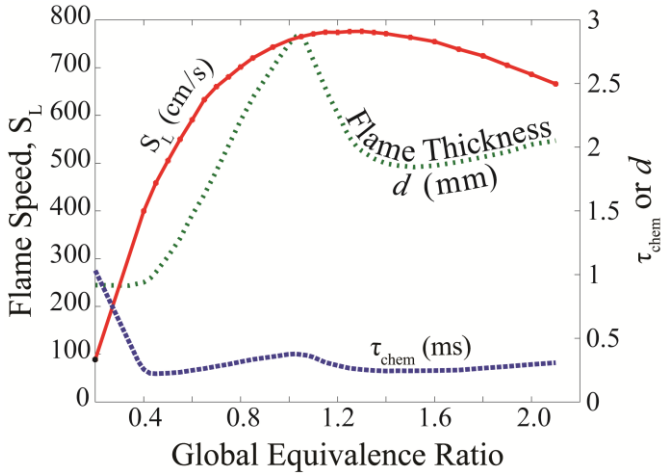

Figure 97: An example calculation of the laminar flame speed, flame thickness, and flame time for $\varphi_{co\text{-}flow}$ = 0.18.

$\overline{\varphi}_{Global}$ is determined through analysis of the global (1-step) reaction equation where equivalence ratio is set such that H_2/O_2 equals that of a reaction of H_2 with air at the same equivalence ratio. The resulting $\overline{\varphi}_{Global}$ definition can be computed using Equation 19 for specified values of $\varphi_{co-flow}$, y_{N2}, and $y_{H2,G}$, where, $y_{H2,G}$ refers to the local (global) H_2 mole fraction as the jet reactants mix with co-flow products.

$$\bar{\varphi}_{Global} = \frac{0.5+2.38/\varphi_{co-flow}}{\left(1/y_{H_{2,G}} - \frac{y_{N_{2,j}}}{1-y_{N_{2,j}}} - 1\right)\left(1/\varphi_{co-flow} - 1\right)} \qquad (19)$$

The jet diameter serves as a basis for the integral length scale, since turbulence scales cannot exceed the jet diameter before the jet fluid is issued into the environment. It is assumed here that a) the flame propagation speed scales with the laminar flame speed and that b) flame propagation is the mechanism most influential in determining the liftoff height for the steady lifted flames studied. The latter assumption is supported by Peters' work [17]. The former assumption is made with the understanding that correlation scatter can be partially attributable to disparities between this assumption and the real conditions. The density weighting accounts for the influence of nitrogen dilution on jet momentum, independent of jet velocity [56]. As nitrogen dilution is increased, jet momentum increases, which increases downstream fluid velocities. Figure 98 is included as an example demonstrating the challenging task of correlation development of liftoff height for the conditions investigated.

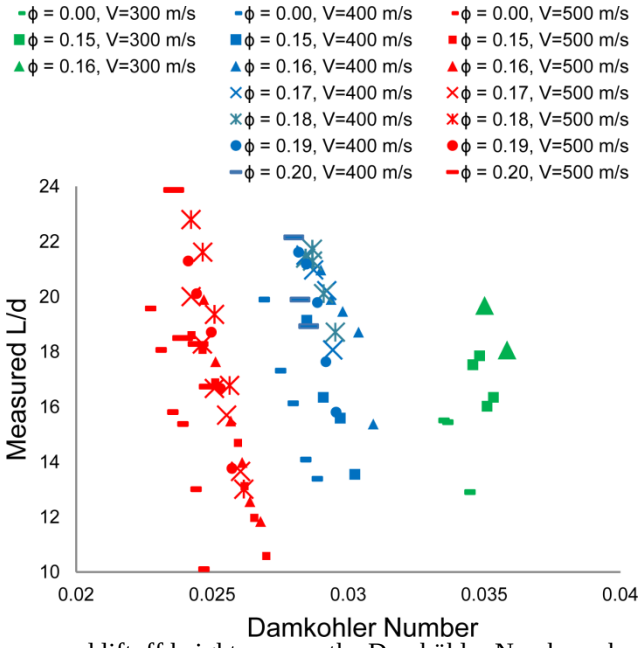

Figure 98: Experimentally measured liftoff heights versus the Damköhler Number where the jet diameter is used as the flow length scale.

Damköhler Number Redefined

Because of the inadequacy of the traditional Damköhler number definition first employed, the Damköhler is redefined in more adequately accounting for the physics encountered with the VCB. The second method uses an alternative length scale in computing the flow time, $z_{\overline{\varphi}=1.5}$:

$$Da_2 = \frac{\tau_{flow}}{\tau_{chem}} = \frac{z_{\overline{\varphi}=1.5}/\left(V_{jet}\left(\rho_{jet}/\rho_{\infty}\right)^{1/2}\right)}{\delta/S_L} \qquad (20)$$

where $z_{\overline{\varphi}=1.5}$ is the axial location where $\overline{\varphi}_{Global}$ = 1.5, which is where a local minimum in flame time occurs as shown in Figure 97 for an example case with $\varphi_{co\text{-}flow}$ = 0.18. The assumption is made here that errors associated with using the z-location along the jet centerline versus the radial location (r_s) where stabilization actually occurs are negligible because r_s is typically small (r_s = 1.7 for the flame depicted in Figure 54 for example) compared to the stabilization height.

Scalar dissipation also impacts the stabilization location to a degree, though Peters [17] explains that scalar dissipation effects are negligible when tribrachial propagation dominates.

Again, since flame propagation is deemed most influential in the stable lifted flames regime, τ_{flame} is used as the chemical time scale. The flow length scale modification is justifiable because the amount of time for the reactants to become ignitable (due to a decrease in scalar dissipation rate) is dictated solely by this length scale and by the fluid velocity (instead of the jet diameter and the fluid velocity). Furthermore, the original jet diameter flow length scale choice was incomplete because it does not incorporate the fact that larger turbulence quantities can develop from a small jet which result from shear interactions with the co-flow.

Early research conducted by Birch et al [57] on nonreacting jets issuing into quiescent environments resulted in a correlation relating local composition along the jet centerline with *z*. With this correlation, it becomes possible to modify the flow length scale to this more appropriate value in order to improve agreement with experimental results. The axial location which minimizes flame time, $z_{\overline{\varphi}=1.5}$, is calculated from:

$$z_{\overline{\varphi}=1.5} = \left[4\frac{y_{jet}}{y_{\overline{\varphi}=1.5}}\left(\frac{\rho_{jet}}{\rho_{\infty}}\right)^{1/2} - 5.8\right] d_{jet} \qquad (21)$$

where y_{jet} is the mass fraction of the fuel in the jet, $y_{\overline{\varphi}=1.5}$ is the mass fraction of the fuel for $\overline{\varphi}_{Global} = 1.5$, ρ_{jet} is the density of the jet, and ρ_{∞} is the density of the ambient fluid (the co-flow). It is assumed here that the correlation for the centerline fuel concentration decay profile is unaffected by chemical reaction, and this assumption has been shown to be reasonably accurate [58] with reacting flows. The liftoff height data is then plotted against these Damköhler numbers in identifying a single functional relationship between Damköhler number and liftoff height.

The first method using the jet diameter in computing the flow time length scale (Figure 98) captures the effects of N_2-in-H_2 dilution on *L* for fixed V_{jet}, but the results are functionally dependent on V_{jet} as this parameter is varied. The conclusion following this observation is that when inappropriate length or time scales are used in the Damköhler number definition, correlation results are not meaningful. The second method, however, captures the trend with good agreement regardless of $\varphi_{co\text{-}flow}$, V_{jet}, and y_{N2}. The result is shown in Figure 99. This result suggests that the Da_2 formulation based on macroscopic features applies equivalently to the small scales in determining the stability point. The scatter is likely due to the fact that in some cases with higher $\varphi_{co\text{-}flow}$ values, autoignition is competing with propagation in stabilizing the flame as well as some contributions from compressibility effects. The satisfactory agreement is also an indicator that numerical models which do not include compressibility effects can produce meaningful results for lifted flames under similar conditions.

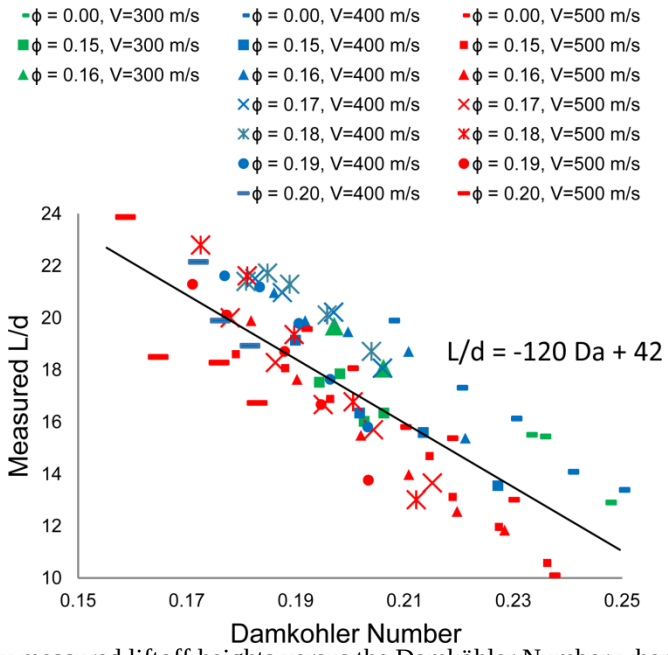

Figure 99: Experimentally measured liftoff heights versus the Damköhler Number where the flow length scale is based on the axial location where the concentration of the fuel results in a minimum chemistry time. The trend is linearly correlated with an R^2 value of 0.68.

A metric for determining how to incorporate the autoignition delay time into the Damköhler number formulation by the use of a weighted average of the flame time and an autoignition delay time which accounts for mixing between the jet and co-flow would likely improve agreement. The weighting percentages should appropriately incorporate the effect of $T_{co\text{-}flow}$ on the stabilization mechanism and the relative importance of autoignition versus tribrachial flame propagation. Additionally, a constant of proportionality that makes the flame time and delay time comparable in terms of how they influence L would likely reduce scatter in the results.

e) Unsteady Regimes Characterization

With the stability regimes diagrams for atmospheric pressure operation created, and the liftoff height characterized as a function of nitrogen dilution and co-flow equivalence ratio at atmospheric pressure, the last investigation to be made at atmospheric pressure was in characterizing the unsteady regime. This work was conducted primarily by Birgitte Johannessen [36]. The unsteady jet flame is characterized by rapid ignition followed by a gradual blowout of the flame. The focus of this effort was on characterizing the frequency of ignition and extinction of the flame as a function of jet velocity, nitrogen dilution, and co-flow equivalence ratio. Several methods were identified to quantify this frequency, and it was determined that using a microphone to capture the acoustic emissions present during jet ignition and extinction was most effective. The number of acoustic emission peaks per second is then measured by examining an amplitude-time plot of the microphone signal. The following results are consistent with Ms. Johannessen's Master's thesis [36], which further describes these research efforts in detail with a more thorough presentation of experimental results.

Figure 100 shows a series of pictures from the Schlieren imaging of the ignition event of an unsteady flame. The ignition event occurs within 6.7 ms. Figure 100a shows a picture when the

flame is blown out. In Figure 100b the flame is re-attaching. This picture is taken 3.3 ms after the first picture. The flame has the shape of a martini glass. In Figure 100c the flame has the shape of a normal attached jet flame. These pictures give an illustration of how fast the ignition occurs and what it looks like.

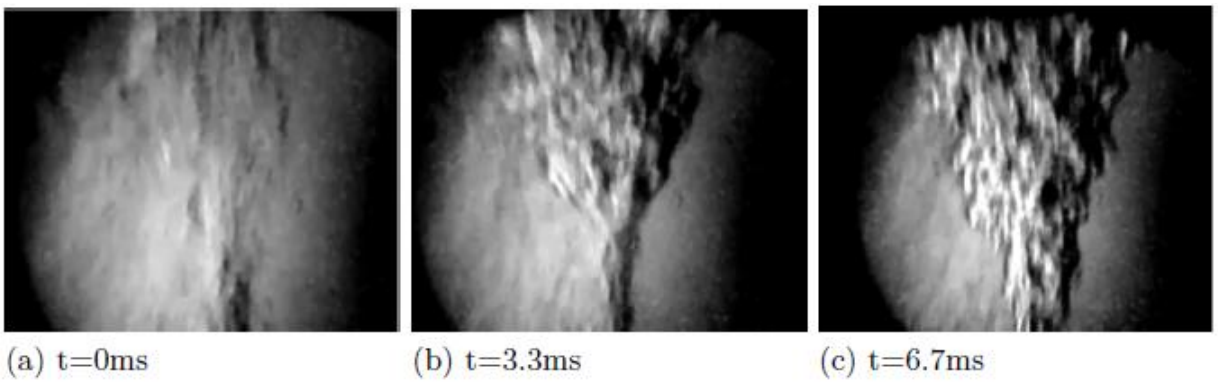

Figure 100: Sequence of images showing the ignition process of the jet.

The unsteady regime was characterized in detail. The first step was to develop a relationship between ignition frequency and nitrogen dilution for various jet velocities and co-flow equivalence ratios. These results are summarized in Figure 101:

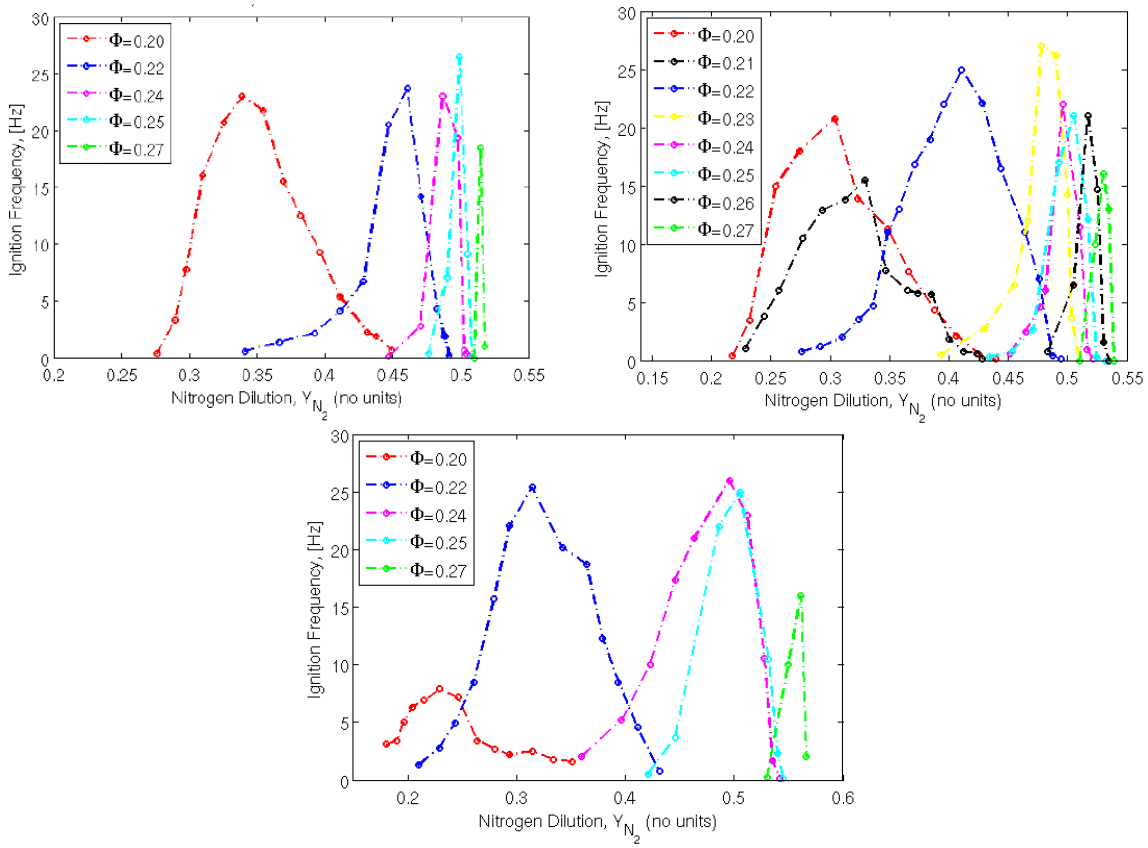

Figure 101: Ignition frequency as a function of nitrogen dilution for various co-flow equivalence ratios for a jet velocity of 300 m/s (top left), 400 m/s (top right), and 500 m/s (bottom).

As the co-flow equivalence ratio increases, the range of nitrogen dilution which produces an unsteady flame increases. Also, as the co-flow equivalence ratio increases, more nitrogen dilution is necessary to cause the flame to become unsteady. The value of the peak frequency, however, remains relatively constant.

Generally, the rising portion of the curve is characteristic of the flame becoming less steady. The flame is less and less often attached to the nozzle or lifted as the frequency increases. Past the peak, however, they flame is oscillating between being blown out and lifted. As the nitrogen dilution increases further, the flame is blown out more often. These results have also been characterized by keeping the co-flow equivalence ration constant, and plotting the effect of varying the velocity, shown in Figure 102.

Note that at low co-flow equivalence ratios, increases the jet velocity necessitate more nitrogen dilution to keep the flame in the unsteady regime. For intermediate co-flow equivalence ratios, the peak frequency occurs at about the same amount of nitrogen dilution for all jet velocities. Finally, at a co-flow equivalence ratio of 0.27, higher jet velocities require more nitrogen dilution to keep the flame in the unsteady regime.

As was stated previously, the method of counting acoustic amplitude peaks was compared to the method of examining high speed schlieren video of the flames. These results are presented in Figure 103.

Clearly, the two methods agree favorably.

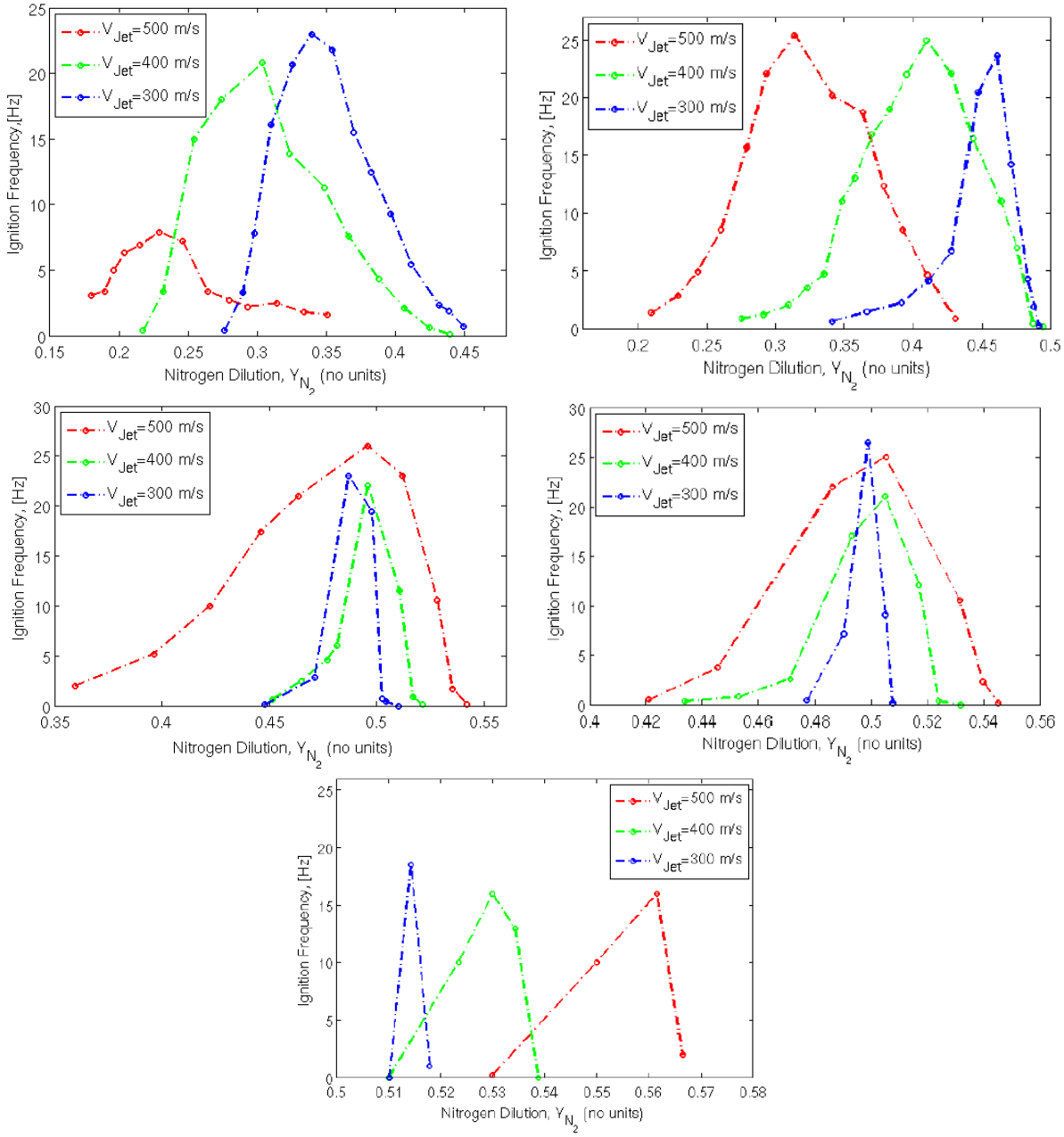

Figure 102: Ignition frequency as a function of nitrogen dilution for 3 jet velocities for a co-flow equivalence ratio of 0.20 (top left), 0.22 (top right), 0.24 (middle left), 0.25 (middle right), 0.27, bottom.

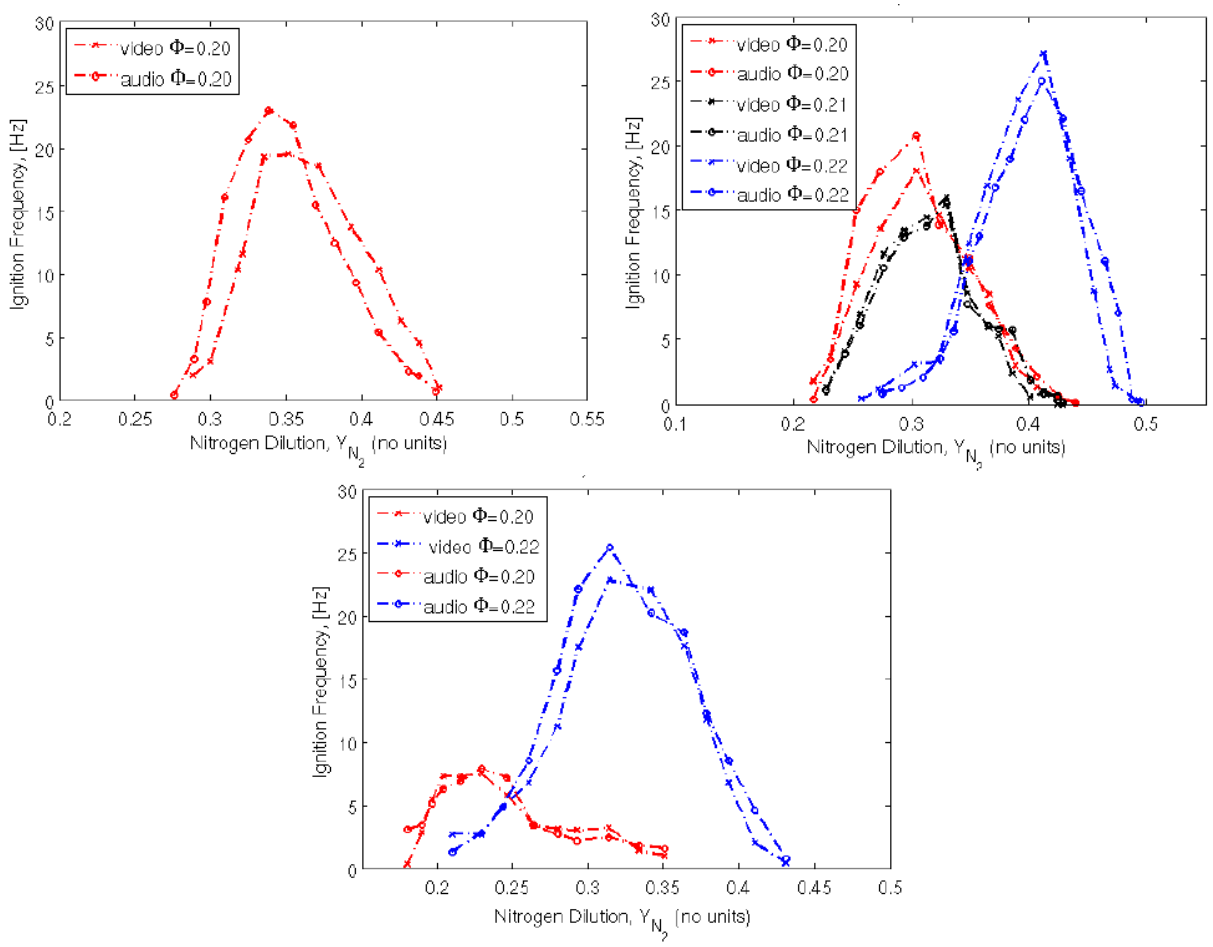

Figure 103: Comparison of ignition frequency results obtained from the method of counting acoustic amplitude to the method of examining high speed schlieren video for a jet velocity of 300 m/s (top left), 400 m/s (top right), 500 m/s (bottom).

iii. *Elevated Pressure Research*

a) Stability Regime Diagrams With Confinement

Elevated pressure experiments began soon after the atmospheric pressure experiments were completed. With the elevated pressure apparatus, it was first deemed prudent to make an attempt at re-drawing the stability regimes diagrams with confinement. The intended purpose of these tests was to determine if confinement alone, at atmospheric pressure, affects the stability of the flame. Figure 104 shows stability regimes diagrams for 400 m/s and 500 m/s at atmospheric pressure with confinement. These diagrams were produced without the exhaust valves installed, so it is confinement alone that differs between these experiments and those produced previously.

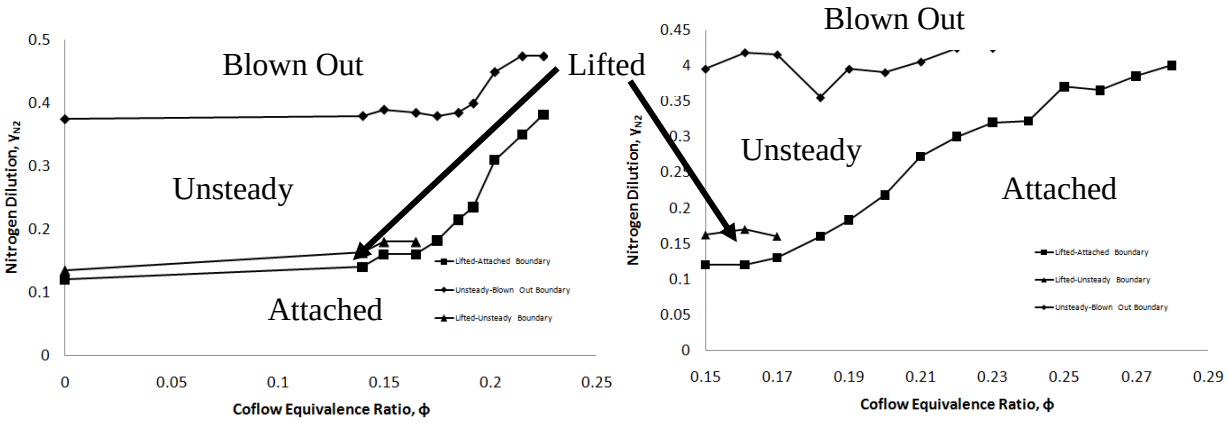

Figure 104: Stability regimes diagrams for a jet velocity of 400m/s (left), and 500 m/s (right). These diagrams outline when the flame is attached, lifted, unsteady, and blown out.

There are some key differences between there results and those obtained without confinement. First, lifted flames only exist for co-flow equivalence ratios less than 0.17 whereas without confinement, lifted flames existed for equivalence ratios less than 0.2. Also, for lifted flames, when the amount of nitrogen dilution is increased, the flame becomes unsteady instead of blowing out. It takes much more nitrogen dilution to get the flame to fully blow out with confinement. It is thought that recirculation of hot products acts as an intermittent stabilizing factor keeping the flame lit even for very high levels of nitrogen dilution. Many aspects of the stability regimes diagrams are similar to those obtained without confinement.

It was also noticed that the stability regimes diagrams change once again when the exhaust valves are installed (still at one bar). These stability regimes diagrams were not produced, but it was found that the nitrogen dilution range that produces lifted flames is increased with the exhaust valves installed.

b) Liftoff Height Characterization

Liftoff height dependence on P_{chamb}, $\varphi_{co\text{-}flow}$, y_{N2}, and V_{jet}, is next characterized using the elevated pressure apparatus with particular focus on pressure dependence. The sensitivity of L with respect to these parameters was characterized first for determination of the most influential variables on L. The sensitivity analysis was conducted for a base case with $\varphi_{co\text{-}flow} = 0.15$, $y_{N2} = 0.33$, $V_{jet} = 400$ m/s, and $P_{chamb} = 1.5$ bar using the following expression.

$$\boldsymbol{S_{y,dy} = \frac{(L_{y+dy} - L_y) - (L_{y-dy} - L_y)}{dy/y}} \qquad (22)$$

The sensitivity analysis results are summarized in Figure 105:

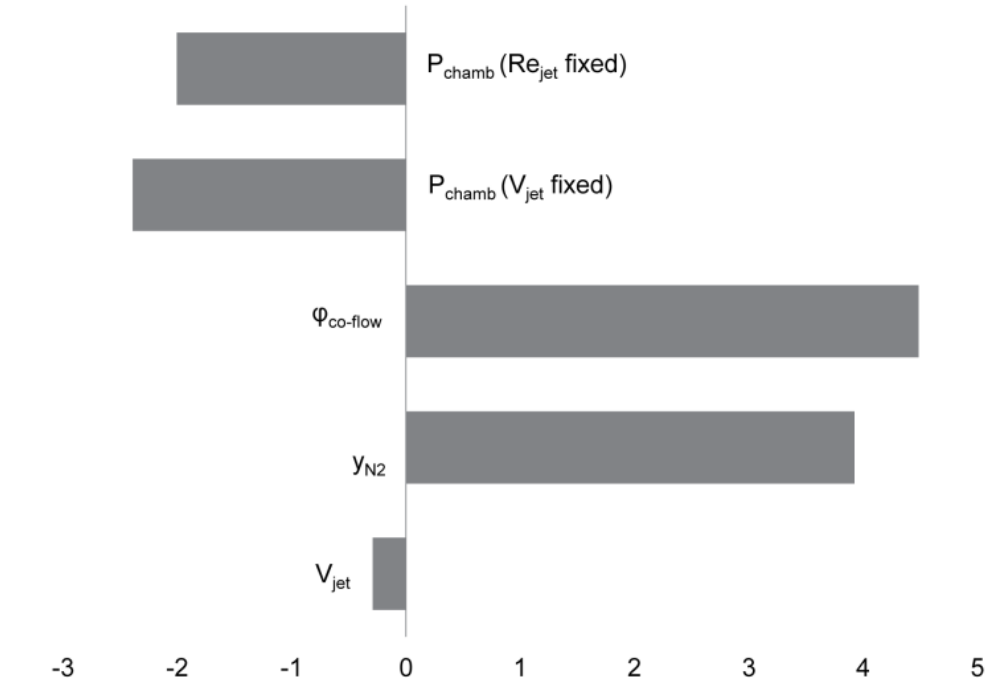

Figure 105: Sensitivity analysis showing the sensitivity of L with respect to V_{jet}, y_{N2}, $\varphi_{co\text{-}flow}$, and P_{chamb} with both V_{jet} and Re_{jet} fixed.

0.1 bar was chosen as the increment value, dy, for P_{chamb} (both with Re_{jet} and V_{jet} fixed) sensitivity, 0.005 for $\varphi_{co\text{-}flow}$ sensitivity, 0.04 for y_{N2} sensitivity, and 100 m/s for V_{jet} sensitivity. As expected, L exhibits negative sensitivity to P_{chamb}, particularly when V_{jet} is held constant because pressure increases lead to V_{jet} decreases when Re_{jet} is fixed causing further liftoff height reductions. Also as expected, a strong positive sensitivity of the liftoff height with respect to y_{N2} is observed. Nitrogen addition increases jet momentum which increases fluid velocity downstream of the nozzle exit and reduces the flame propagation speed. Both of these factors bear positive contributions toward V_{jet} - L sensitivity. Surprisingly, a strongly *positive* sensitivity with respect to co-flow equivalence ratio is observed. The increase in co-flow equivalence ratio leads to an increase in flame speed which should serve to reduce the liftoff height. However, since the co-flow air flow rate is held constant as equivalence ratio is varied with these experiments, the increased co-flow velocity accompanying stoichiometry increases likely effects L sensitivity more than temperature under these conditions. In short, as $\varphi_{co\text{-}flow}$ increases, the accompanied temperature increase causes an additional co-flow velocity increase (accompanied by the co-flow velocity increase contribution from the co-flow H_2 flow rate increase) because of the vitiated air density reduction. Previous research by Montgomery et. al. [53] and others explores and explains liftoff height dependence on co-flow velocity.

The dependence of L on P_{chamb} is characterized for various values of V_{jet} and y_{N2} as well as cases where Re_{jet} is held constant since it is unclear whether fixing V_{jet} or Re_{jet} is most appropriate. Figure 106 compares L pressure dependence for V_{jet} = 400 m/s and 500 m/s and with y_{N2} = 0.33 and $\varphi_{co\text{-}flow}$ = 0.15.

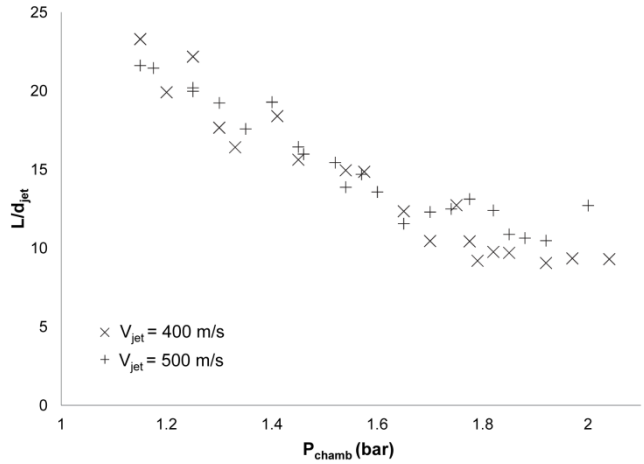

Figure 106: Experimental measurements of L normalized by d_{jet} versus P_{chamb} with constant jet velocities of V_{jet} = 400 m/s and 500 m/s, and with y_{N2} = 0.33 and $\varphi_{co\text{-}flow}$ = 0.15 ($T_{co\text{-}flow}$ = 664 K).

Consistent with the sensitivity analysis, L pressure trending is nearly identical for the two V_{jet} values. L insensitivity to V_{jet} for fully turbulent jet flames can be explained in a similar manner that flame length insensitivity to V_{jet} is explained for attached turbulent jet flames. As jet velocity increases, turbulent diffusivity (D_t) increases, leading to faster mixing which can balance the reduction in flow time [59].

A pressure sweep with Re_{jet} fixed instead of V_{jet} as pressure increases further demonstrates L insensitivity to V_{jet}.

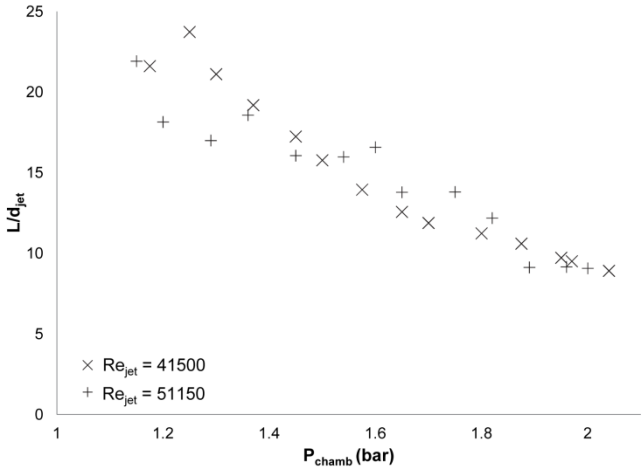

Figure 107: Experimental measurements for L normalized by d_{jet} versus pressure at constant jet Reynolds numbers of Re_{jet} = 41500 and 51150, and with y_{N2} = 0.33 and $\varphi_{co\text{-}flow}$ = 0.15 ($T_{co\text{-}flow}$ = 664 K).

V_{jet} at 1.15 bar (the minimum pressure explored due to apparatus limitations) is 400 m/s and 500 m/s for Re_{jet} = 41500 and 51150, respectively. As P_{chamb} is increased, the reduction in V_{jet} for Re_{jet} = 41500 and 51150 scales by an equivalent factor, so Figure 107 demonstrates L insensitivity to Re_{jet} which does not diminish with velocity reductions resulting from increases in pressure up to 2 bar.

In assessing conditions for which D_t does not scale linearly with V_{jet}, an addition pressure sweep at y_{N2} = 0.20 demonstrates that L insensitivity to V_{jet} occurs only when turbulence intensity is great enough to be considered "fully turbulent", or for conditions where Re_{jet} exceeds a threshold value.

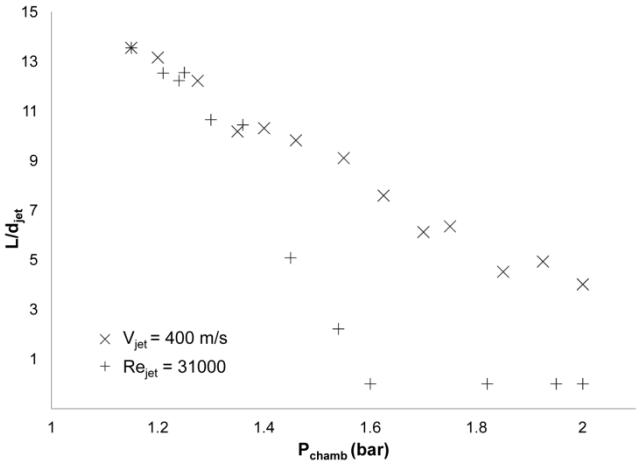

Figure 108: Experimental measurements for L normalized by d_{jet} versus pressure for a constant jet velocity of V_{jet} = 400 m/s and a constant jet Reynolds numbers of Re_{jet} = 31000, and with y_{N2} = 0.20 and $\varphi_{co\text{-}flow}$ = 0.15 ($T_{co\text{-}flow}$ = 664 K).

As with Figure 107, V_{jet} at P_{chamb} = 1.15 bar is equivalent for the two cases considered. The reduction in Re_{jet} resulting from a reduction in y_{N2}, however, introduces a significant L sensitivity on V_{jet} which is evident in Figure 108. As P_{chamb} is increased, the reduction in V_{jet} for the constant Re_{jet} cases causes a flame stabilization location departure between the constant Re_{jet} cases and constant V_{jet} cases. This result suggests that for Re_{jet} = 31000, turbulence intensity is not great enough for linear D_t - V_{jet} scaling. Scaling laws used for understanding flame length insensitivity (shown in Figure 109) on V_{jet} apply in a similar manner in explaining liftoff height insensitivity on V_{jet} shown here.

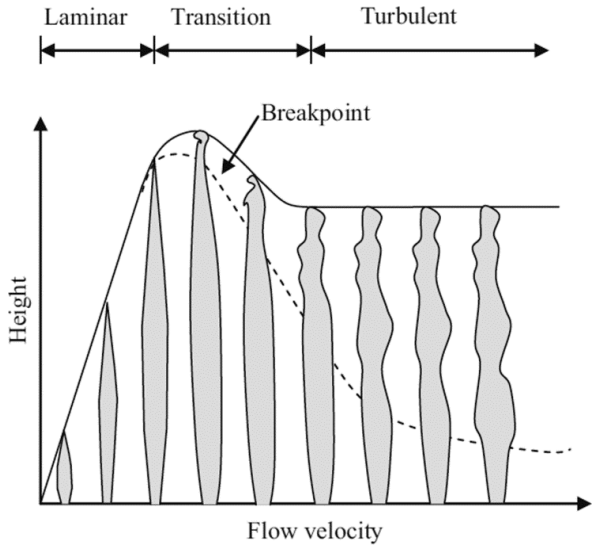

Figure 109: Qualitative depiction of flame length versus jet flow velocity showing flame height insensitivity to jet flow velocity for fully turbulent jet flames [59].

c) Liftoff Height Correlation with Elevated Pressure

The elevated pressure liftoff height data is next correlated with the Damköhler Number, where the flow length scale is defined as the distance the fluid travels before reaching an equivalence ratio where flame time is minimized. The data is first plotted together in understanding the level of scatter encountered as the chosen independent parameters are varied.

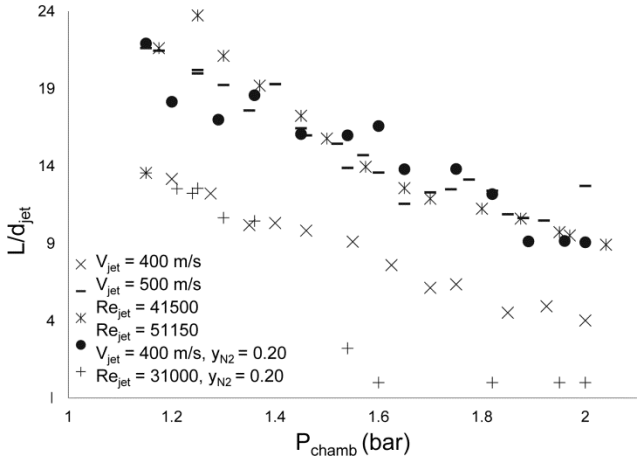

Figure 110: Liftoff height data summarized in a single plot used for correlation formulation.

Cases with y_{N2} = 0.33 exhibit minimal dependence on jet velocity and the choice of holding V_{jet} or Re_{jet} constant. A departure occurs when y_{N2} decreases as shown with the y_{N2} = 0.20 data.

In investigating the applicability of the Damköhler number used for the atmospheric pressure research on the elevated pressure results, flame time is first computed. While the atmospheric (and unconfined) numerical results indicated that the local equivalence ratio which minimizes flame time is a consistent value of $\overline{\varphi}_{mr}$ = 1.5, the elevated pressure conditions have a minimum that is slightly leaner as outlined in Figure 111 and Figure 112.

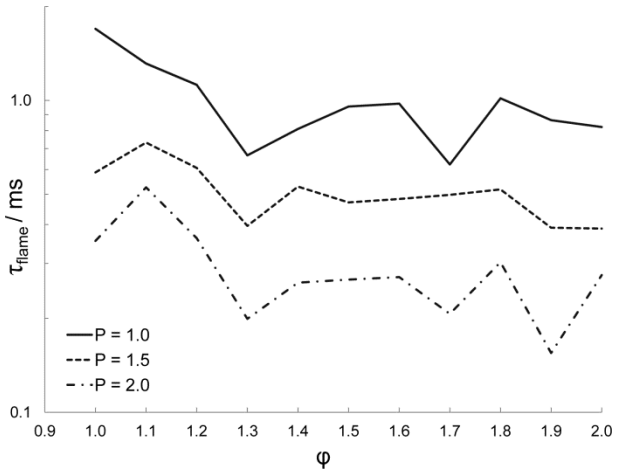

Figure 111: Flame time versus local equivalence ratio for y_{N2} = 0.33 and $\varphi_{co\text{-}flow}$ = 0.15 for selected pressures.

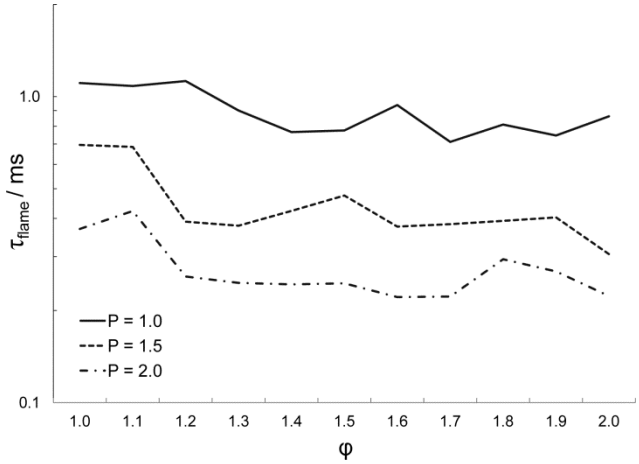

Figure 112: Flame time versus local equivalence ratio for y_{N2} = 0.20 and $\varphi_{co\text{-}flow}$ = 0.15 for selected pressures.

The base cases with y_{N2} = 0.33 exhibits a local minimum when $\overline{\varphi}_{mr}$ = 1.3. Other local minimums exist, though it is reasonable to postulate that the flame most often anchors where the local minimum in flame time is closest to the stoichiometric value because the flame propagates toward the nozzle until reaching the steep equivalence ratio rise at φ_{mr} < 1.3. With y_{N2} reduced to 0.20, however, the flame time sensitivity on $\overline{\varphi}_{mr}$ reduces. Furthermore, the local minimum is a function of pressure for y_{N2} = 0.20. The reduced sensitivity likely increases the impact of factors other than flame time on the liftoff height. Nonetheless, the local minimum observed for P = 1.4 was selected for analysis of the y_{N2} = 0.20 data because this is the minimum for the atmospheric pressure cases. Consequently, this is the only flame time minimum for which the jet velocity is equivalent between the cases where V_{jet} and Re_{jet} were held constant with the intent of understanding the observation that fixing this independent parameter becomes important when y_{N2} is reduced.

Damköhler numbers are then computed for the elevated pressure data set. V_{jet} is again weighted by the square root of the jet density to surrounding fluid density in incorporating the momentum increase effect imparted by N_2 dilution onto τ_{flow}. τ_{flame} is again computed as the ratio of the flame thickness (δ) to the laminar flame speed (S_L).

The resulting dependence of the pressurized normalized liftoff heights measured on the Damköhler number is presented in Figure 113:

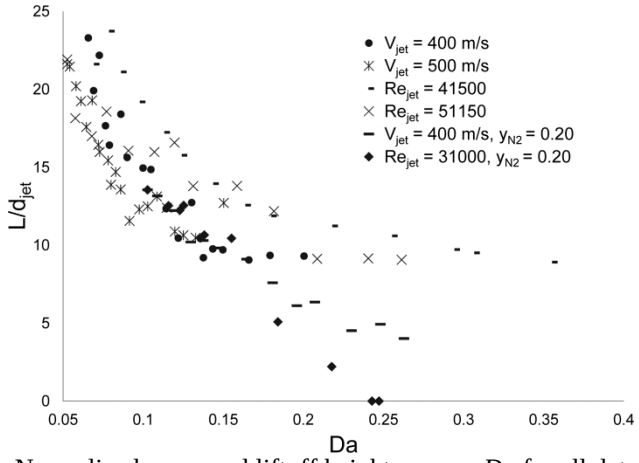

Figure 113: Normalized measured liftoff heights versus *Da* for all data presented.

Generally, L/d_{jet} trends surprisingly well with *Da*. Trending is poor for $y_{N2} = 0.20$ which is attributable to the additional effect of turbulent diffusivity scaling nonlinearly with V_{jet} for lower Reynolds number jets – an effect which has not been included with this correlation.

When the co-flow equivalence ratio is increased beyond 0.15, flame stability is significantly compromised, as shown in Figure 114 and Figure 115 with a co-flow equivalence ratio of 0.17.

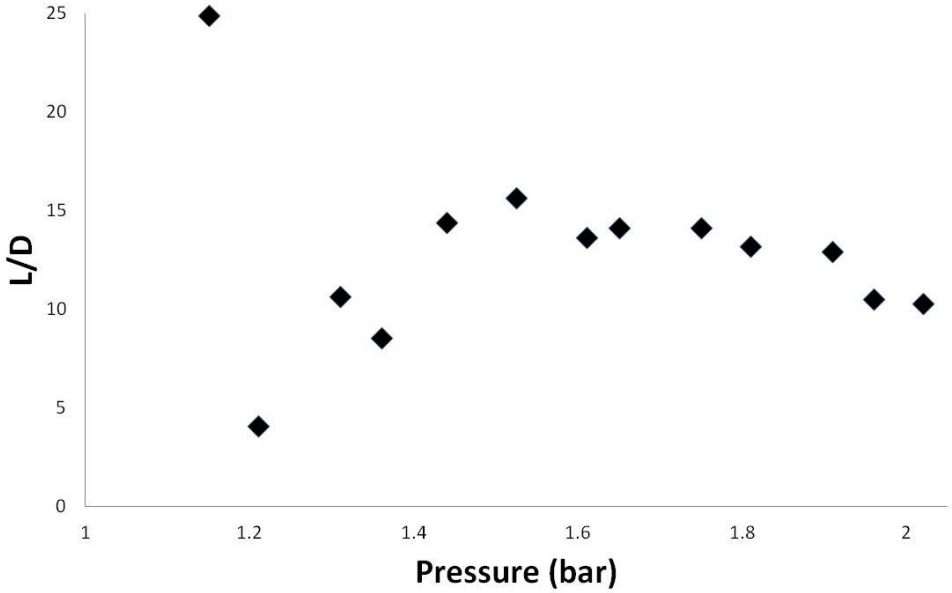

Figure 114: Liftoff height dependence on pressure for a nitrogen dilution mole fraction of 0.33, a constant jet velocity of 400 m/s, and a co-flow equivalence ratio of 0.17.

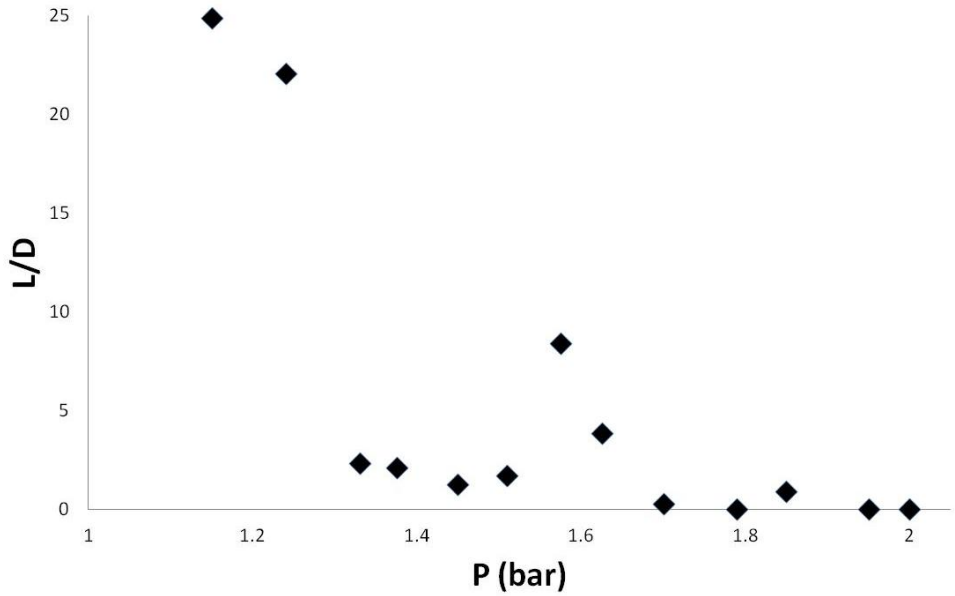

Figure 115: Liftoff height dependence on pressure for a nitrogen dilution mole fraction of 0.33, a constant jet Reynolds number of 41500, and a co-flow equivalence ratio of 0.17.

When jet velocity is held constant, dependence of liftoff height on chamber pressure is weak and somewhat erratic. When jet Reynolds number is held constant, however, the flame becomes attached for most pressures above 1.3 bar. Measured liftoff heights are highly stochastic, and analysis of the transient liftoff height values for each data point reveals significantly higher variance in liftoff height through time than the cases with a co-flow equivalence ratio of 0.15. Peters [17] explains that increased jet nozzle inner diameters can result in increased lifted flame stability with hotter co-flows because strain rates are reduced while keeping jet momentum constant. This strategy may reduce local extinction, increasing lifted flame stability. A risk with larger jet diameters is introduced, however, relating to the maximum heat release rate that the chamber can handle, since heat loads are absorbed by the constant thermal mass of the metal pressure vessel walls. Consequently, the jet nozzle inner diameter choice of 2.4 mm was still the best fit in terms of making elevated pressure experimental results consistent with those gathered at atmospheric pressure, and in keeping the heat load manageable, as well as for various safety reasons.

5. Conclusions

Improvements in the understanding of stability and ignition for diluted premixed and partially premixed H_2 flames are beneficial for H_2 optimized gas turbine combustor development. Lifted flames are an attractive target flame for numerical model benchmarking and flame stabilization theory improvements because the measurable liftoff height is dependent on chemical, transport, and fluid dynamic effects. Numerical models capable of accurately replicating experimentally measured liftoff heights under all relevant conditions can be used in gas turbine combustor development with increased confidence because the complexities which inherently influence the stabilization location in laboratory flames are equally applicable in gas turbine environments. The primary contribution of this research is the generation of data sets which characterize the

stability regimes under a multitude of conditions and the stabilization height of turbulent N_2-in-H_2 jet flames in a vitiated co-flow versus environment temperature, jet velocity, nitrogen dilution, and pressure.

Stability regime diagrams developed are presented which outline the conditions under which a N_2-in-H_2 jet flame in a vitiated co-flow is attached, lifted, blown-out or unsteady. The stability regime diagrams are an effective means of facilitating understanding of the interaction of the factors influential in stabilizing jet flames. For the burner geometry used, it is found that lifted flames exist for co-flow equivalence ratios below 0.20 when enough N_2 dilution is added to the fuel. A co-flow equivalence ratio of 0.20 corresponds to an estimated co-flow temperature of 810 K which is near the autoignition temperature of H_2 indicating that lifted flame stability is likely dominated by flame propagation for all cases where stable lifted flames exist. For co-flow equivalence ratios above 0.20, autoignition becomes important, and the flame is unsteady with no definable liftoff height. A steady 1-D parabolic RANS code is also utilized in investigating the stability regimes diagrams and good agreement with experimental results was achieved. The numerical results also suggest that flame propagation dominates flame stability for co-flow equivalence ratios below 0.20.

The lifted flame regime is further characterized by determining the dependence of liftoff height on N_2 dilution, jet velocity, co-flow equivalence ratio, and pressure. Experimental results at atmospheric pressure exhibit the strongest (positive) liftoff height dependence on nitrogen dilution mole fraction. The liftoff height is also positively dependent upon the velocity of the jet, though to a lesser extent. The effect of co-flow equivalence ratio is most pronounced near $\varphi_{co\text{-}flow} = 0.20$, where autoignition likely begins to play a role. Additionally, the transition from the cold co-flow cases ($\varphi_{co\text{-}flow} = 0.00$) to the cases near co-flow blowout ($\varphi_{co\text{-}flow} = 0.15$) exhibit a significant liftoff height dependence on co-flow equivalence ratio. Liftoff height is weakly dependent on co-flow equivalence ratio for all other cases where $0.00 \leq \varphi_{co\text{-}flow} \leq 0.15$.

The unsteady regime was also studied in detail at atmospheric pressure with varying nitrogen dilution mole fraction, co-flow temperature, and jet velocity by the use of audio recordings and schlieren imaging high speed videos. The results from both the audio recordings and the schlieren imaging suggest that the ignition of the unsteady jet flames occurs as a result of autoignition. With this regime, the ignition frequency increases with increasing nitrogen dilution mole fraction in the jet until a maximum frequency is reached. After reaching the maximum frequency, the frequency decreases with further increases of the nitrogen dilution mole fraction. For increasing co-flow temperatures the flames become unsteady and blow out at increasing nitrogen dilution mole fractions. An increase in the jet velocity leads to unsteady and blown out flames for decreasing nitrogen dilution mole fractions for low co-flow temperatures. Higher co-flow temperatures lead to an increasing range of nitrogen dilution mole fractions over which jet flames with increasing velocities are unsteady. An increase in the velocity leads to an unsteady flame for lower nitrogen dilution mole fractions and a blown out flame for higher nitrogen dilution mole fractions at higher co-flow temperatures.

For the pressurized experiments, L dependence on pressure is negative indicating that the reduction in flame time resulting from pressure increases is the dominant factor imparted by pressure effects. For high jet Reynolds numbers ($Re_{jet} \geq 41500$), L is insensitive to V_{jet} which

indicates that the rate at which turbulent diffusivity increases balances the reduction in flow time as V_{jet} is increased for the conditions investigated. When Re_{jet} is reduced ($Re_{jet} \leq 31000$) by reducing the concentration of the N_2 diluent, however, L sensitivity to V_{jet} becomes positive. A sensitivity analysis confirms L insensitivity to V_{jet} for high turbulence intensity. The sensitivity analysis also indicates highly positive L sensitivity to $\varphi_{co\text{-}flow}$ and y_{N2}, whereas L sensitivity to pressure is highly negative both when V_{jet} is held constant and Re_{jet} is held constant as pressure is varied.

A 1D steady parabolic RANS code effectively captures the stability regimes, though the same method cannot correctly predict the liftoff height for lifted flames. Kalghatgi's correlation for predicting liftoff heights shows excellent results for jets issuing into quiescent environments, so it is investigated in assessing its applicability for cases where a heated co-flow is involved. Kalghatgi's correlation poorly predicts the trend for hot co-flow conditions, yet captures the trend adequately for cold co-flow conditions. Thus, the correlation is found incapable of predicting correctly the dependence of liftoff height on N_2 dilution for hot co-flows. Since existing correlations were found inappropriate where heated co-flows are applied, research was conducting on developing a new correlation which incorporates the temperature effect turbulent lifted flames.

The new correlation is based upon the Damköhler number, with careful selection of flow and chemical time scales. The liftoff height data is plotted against the Damköhler number showing a direct relationship when the Damköhler number is appropriately defined. This result suggests that the Damköhler number is an overarching parameter that describes lifted flame dynamics for the conditions investigated, which span many flame stabilization regimes. By properly choosing the parameters defining the flow time scales and chemical time scales which address the dominant flame stabilization mechanism, a direct dependence of liftoff height on the Damköhler number is observed. Consequently, the Damköhler number can be used as a means of estimating the liftoff height when experimental data is nonexistent for guiding future experimental and numerical work. Since the chemical time scale which produces the strongest correlation is based on flame propagation, the hypothesis that flame propagation dominates flame stabilization when the co-flow is below the autoignition temperature is reinforced. Numerous prior studies indicate that for lifted flames in ambient environments, tribrachial flame propagation is paramount, and may also be paramount for these flames. The numerical investigation presented also reinforces the tribrachial flame propagation theory. For stable lifted flames issuing into co-flows hotter than the autoignition temperature, autoignition becomes influential in determining the ignition location. For these flames, the Damköhler number should incorporate the autoignition delay time into the chemical time scale instead of using the flame time alone. The potential for using a single metric for predicting liftoff characteristics across several stability regimes, however, is attractive.

6. References

[1] O. Bolland, H. Undrum, Advances in Environmental Research 7 (2003) 901-911.
[2] P. Chiesa, G. Lozza, L. Mazzocchi, ASME J. of Eng. Gas Turbines and Power 127 (2005) 73-80.
[3] K.M. Lyons, Prog. Energy Combust. Sci. 33 (2007) 211-231.
[4] W.M. Pitts, Proc. Combust. Inst. 22 (1988) 809-816.
[5] L. Vanquickenborne, A. Van Tiggelen, Combust. Flame 10 (1966) 59-69.
[6] M.J. Dunn, A.R. Masri, R.W. Bilger, R.S. Barlow, G.H. Wang, Proc. Combust. Inst. 32 (2009) 1779–1786.
[7] N. Peters, F.A. Williams, AIAA 21 (3) (1983) 423-429.
[8] M.M. Tacke, D. Geyer, E.P. Hassel, J. Janicka, (1998). Proc. Combust. Inst. 27 (1998) 1157-1165.
[9] L. Muniz, M. G. Mungal, Combust. Flame, 111 (1997) 16-31.
[10] J. Buckmaster, Prog. Energy Combust. Sci. 28 (2002) 435-475.
[11] R. Cabra, T. Myhrvold, J. Y. Chen, R. W. Dibble, A. N. Karpetis, R. S. Barlow, Proc. Combust. Inst. 20 (2002) 1881-1888.
[12] R. Cabra, J. Y. Chen, R. W. Dibble, A. N. Karpetis, R. S. Barlow, Combust. Flame 143 (2005) 491-506.
[13] T. Myhrvold, I.S. Ertesvag, I.R. Gran, R. Cabra, J. Y. Chen, Combust. Sci. Technol. 178 (2006) 1001–1030.
[14] R.L. Gordon, A.R. Masri, S.B. Pope, G.M. Goldin, Combust. Theory Model. 11 (3) (2007) 351–376.
[15] C.N. Markides, E. Mastorakos, Proc. Combust. Inst. 30 (2005) 883-891.
[16] G.T. Kalghatgi, Combust. Sci. Technol. 41 (1984) 17-29.
[17] N. Peters, Turbulent Combustion, Cambridge University Press, Cambridge, U.K., 2000 237-261.
[18] R.R. Cao, S.B. Pope, A.R. Masri, Combust. Flame 142 (2005) 438-453.
[19] S. Kumar, P.J. Paul, H.S. Mukunda, Combust. Sci. Technol. 179 (2007) 2219–2253.
[20] R.L. Gordon, S.H. Stårner, A.R. Masri, R.W. Bilger, Further Characterisation of Lifted Hydrogen and Methane Flames Issuing into a Vitiated Coflow, 5th Asia-Pacific Conference on Combustion, Asia-Pacific Regional Affiliate of the Combustion Institute, Adelaide, Australia, 2005.
[21] R Gordon, A. Masri, E Mastorakos, Combust. Flame 155 (2008) 181-195.
[22] R. Gordon, A. Masri, S. Pope, G. Goldin, Combust. Flame, 151 (2007), 495–511.
[23] R. Gordon, Ph.D. thesis, The University of Sydney, 2007.
[24] R. Cabra, Turbulent Jet Flames in a Vitiated Coflow, Report No. NASA/CR-2004-212887 E-14301, NASA Glenn Research Center, 2004.
[25] R. Cabra et al, Turbulent Jet Flames into a Vitiated Coflow. PhD Thesis, UC – Berkeley 2005.
[26] M. Karbassi, I. Wierzba, J. Energy Resource Technol. 120 (1997) 167-171.
[27] R. Kee, J. Grcar, M. Smooke, J. Miller, SAND85-8240. (1985).

[28] P.R. Medwell, B. B. Dally, Energy and Fuels. 26 (2012) 5519-5527.
[29] J.Y. Chen, W.C. Chang, Combust. Sci. Technol. 133 (1998) 343-375.
[30] J. Li, Z. Zhao, A. Kazakov, F.L. Dryer, Int. J. Chem. Kinet. 36 (2004) 566-575.
[31] J. Ströhle, T. Myhrvold, Int. J. Hydrogen Energy 32 (2007) 125-135.
[32] K. Döbbeling, J. Hellat, H. Koch, ASME J. Eng. Gas Turbines and Power 129 (2007) 2-12.
[33] P. Patnaik, A Comprehensive Guide to the Hazardous Properties of Chemical Substances, Wiley-Interscience, Hoboken, New Jersey, U.S. (2007) 402.
[34] J.Y. Chen, W. Kollmann, Proc. Combust. Inst. 22 (1989) 645-653.
[35] S. Muppala, J.X. Wen, N.K. Aluri, F. Dinkelacker, Molecular Transport Effects of Hydrocarbon Addition on Turbulent Hydrogen Flame Propagation, 2nd International Conference on Hydrogen Safety, EU NoE HySafe, San Sebastian, ES, 2007.
[36] B. Johannessen, Studies of Combustion in Berkeley's Vitiated Co-flow Burner (VCB), Master's Thesis No. EPT-M-2011-16, Norwegian University of Science and Technology, 2011.
[37] D. Frederick, Numerical Investigations of a Hydrogen Jet Flame in a Vitiated Co-flow. PhD Thesis, UC – Berkeley 2013.
[38] D.P. Incropera, DeWitt, Fundamentals of Heat and Mass Transfer. 6 (1996) 490-515.
[39] B.S. Petukhov. Adv. Heat Transfer. 6 (1970) 503-565.
[40] V. Gnielinski. Forschung im Ingenieurwesen, 41 (1975) 8-16.
[41] V. Gnielinski. Forschung im Ingenieurwesen 41 (1975) 145-153.
[42] D. Frederick. Design and Modeling of a Vitiated Co-flow Burner and Chamber. Master's Thesis from UC – Berkeley, 2010
[43] G.S. Settles, Schlieren and Shadowgraph Techniques: Visualizing Phenomena in Transparent Media, Springer-Verlag. (2001) 48-58.
[44] D. Varish, T. Dogu, G.U. Journal of Science, 21 (2008) 37-41.
[45] G. Borman, K. Ragland, Combustion Engineering, McGraw-Hill Companies, Inc, 1998.
[46] S.L. Fischer, F.L. Dryer, H.J. Curran, Int. J. Chem. Kinet. 32 (2000) 713–740.
[47] H.J. Curran, S.L. Fischer, F.L. Dryer, Int. J. Chem. Kinet., 32 (2000) 741–759.
[48] E.W. Kaiser, T.J. Wallington, M.D. Hurley, J. Platz, H.J. Curran, W.J. Pitz, C.K. Westbrook, J. Phys. Chem., 35 (2000) 8194-8206.
[49] N.M. Marinov, Int. J. Chem. Kinet. 31 (1999) 183-220 (1999)
[50] D.G. Goodwin, Cantera. (2009). http://code.google.com/p/cantera/
[51] Y. Wu, Y. Lu , I.S. Al-Rahbi, G.T. Kalghatgi, Int. J. Hydrogen Energy 34 (14) (2009) 5940-5945.
[52] R.S. Brokaw, Viscosity of Gas Mixtures. NASA Technical Note, NASA TN D-4496 (1968)
[53] C.K. Montgomery, C.J. Kaplan, C.R. Oran, Proc. Combust. Inst. 27 (1998) 1175-1182.

[54] N. Peters, J. Fluid Mech. 384 (1999) 107-132.
[55] G.Z. Damköhler, Electrochem. 46 (1940) 601–626.
[56] G.R. Ruetsch, L. Vervisch, A. Linan, Phys. Fluids 7 (1995) 1447-1454.
[57] A.D. Birch, D.R. Brown, M.G. Dodson, J. Fluid Mech. 88 (1978) 431-449.
[58] G. T. Kalghatgi, Combust. Sci. Technol. 26 (1981) 233-239.
[59] S. McAllister, J.Y. Chen, A.C. Fernandez-Pello, Fundamentals of Combustion Processes, Springer, New York, USA, 2011 149-151.
[60] W.M. Pitts, Combust. Flame 76 (1989) 197-212.